HUGHES
HUGHES AIRCRAFT COMPANY
ELECTRON DYNAMICS DIVISION

ORNL/SUB-79/33200/18

DEVELOPMENT PROGRAM FOR A 200 kW, CW GYROTRON

W.J. DeHope, P.E. Ferguson, S.L. Hart, V.A. Matranga,
J.J. Sandoval, M.J. Schmitt, J. J. Tancredi, M.A. Wozniak

FINAL REPORT

FEBRUARY 1984

Report Prepared by

HUGHES AIRCRAFT COMPANY
Electron Dynamics Division
3100 West Lomita Boulevard
Torrance, California 90509
under
Subcontract No. 53Y-33200C

for
OAK RIDGE NATIONAL LABORATORY
Oak Ridge, Tennessee 37830
operated by
MARTIN MARIETTA
ENERGY SYSTEMS, INC.
for the
U.S. DEPARTMENT OF ENERGY
Contract No. DE-AC05-84OR21400

Printed in the United States of America. Available from
National Technical Information Service
U.S. Department of Commerce
5285 Port Royal Road, Springfield, Virginia 22161
NTIS price codes — Printed Copy: A03; Microfiche A01

ORNL/SUB-79/33200/18

DEVELOPMENT PROGRAM FOR A 200 kW, CW GYROTRON

W.J. DeHope, P.E. Ferguson, S.L. Hart, V.A. Matranga,
J.J. Sandoval, M.J. Schmitt, J. J. Tancredi, M.A. Wozniak

FINAL REPORT

FEBRUARY 1984

Report Prepared by

HUGHES AIRCRAFT COMPANY
Electron Dynamics Division
3100 West Lomita Boulevard
Torrance, California 90509
under
Subcontract No. 53Y-33200C

for
OAK RIDGE NATIONAL LABORATORY
Oak Ridge, Tennessee 37830
operated by
MARTIN MARIETTA
ENERGY SYSTEMS, INC.
for the
U.S. DEPARTMENT OF ENERGY
Contract No. DE-AC05-84OR21400

ABSTRACT

Development of a millimeter-wave device to produce 200 kW of continuous wave power at 60 GHz is described. The device, a gyrotron oscillator, is intended for electron-cyclotron heating of fusion plasmas. The design philosophy is herein discussed and experimental results, both diagnostic and long pulse, are given.

TABLE OF CONTENTS

LIST OF ILLUSTRATIONS

LIST OF ILLUSTRATIONS (CONTINUED)

LIST OF ILLUSTRATIONS (CONTINUED)

LIST OF ILLUSTRATIONS (CONTINUED)

1.0 OVERVIEW AND DESIGN APPROACH

1.1 GENERAL

In May of 1979, Hughes Aircraft Company, Electron Dynamics Division, embarked on an effort to develop a 110 GHz, 200 kW CW gyrotron oscillator for Oak Ridge National Laboratory, under DOE funding, to be used for electron cyclotron resonance heating of experimental fusion plasmas. This was later redirected to 60 GHz. All testable goals were accomplished in March 1983 with the successful demonstration of 100 ms, 200 kW performance in tube S/N 2A.

1.2 PHYSICAL BASIS

Constraints of conventional devices limit output power to an approximately $\lambda^{5/2}$ dependence due to the combined effects of surface area and skin depth upon circuit thermal dissipation. The gyrotron's natural ability to operate in high order waveguide and cavity modes (though not all modes are equally desirable) enable it to greatly exceed conventional devices' power levels (Figure 1-1). The gyrotron exploits the electron cyclotron maser instability to convert electron beam kinetic energy to rf. To gain insight into the physical mechanism of the ECM instability, we assume an intial set of equally spaced relativistic electrons rotating along a common cyclotron orbit as depicted in Figure 1-2a. When a small sinusoidal electric field is applied ($\omega_{rf} \geq \Omega_c$), those electrons which are phased so as to be accelerated by the electric field will become more massive and rotate slower. Conversely, those electrons which are phased so as to be decelerated by the electric field will lose mass and rotate faster. If we assume the rf frequency ω_{rf} slightly greater than the initial cyclotron frequency, the decelerated electrons will stay in phase with the electric field for a longer time than the accelerated electrons. As a result, the decelerated electrons will lose more energy than is gained by the accelerated electrons with the energy difference going toward increasing the electric field amplitude. Thus, the rf electric field will grow at the expense of the dc rotational energy of the electrons. Figure 1-2b shows the electron distribution after this interaction has occurred. Note the bunching in the azimuthal coordinate analogous to axial bunching seen in conventional microwave tubes such as klystrons and traveling-wave tubes. Figure 1-3 shows a conceptual dispersion diagram for beam and cavity modes.

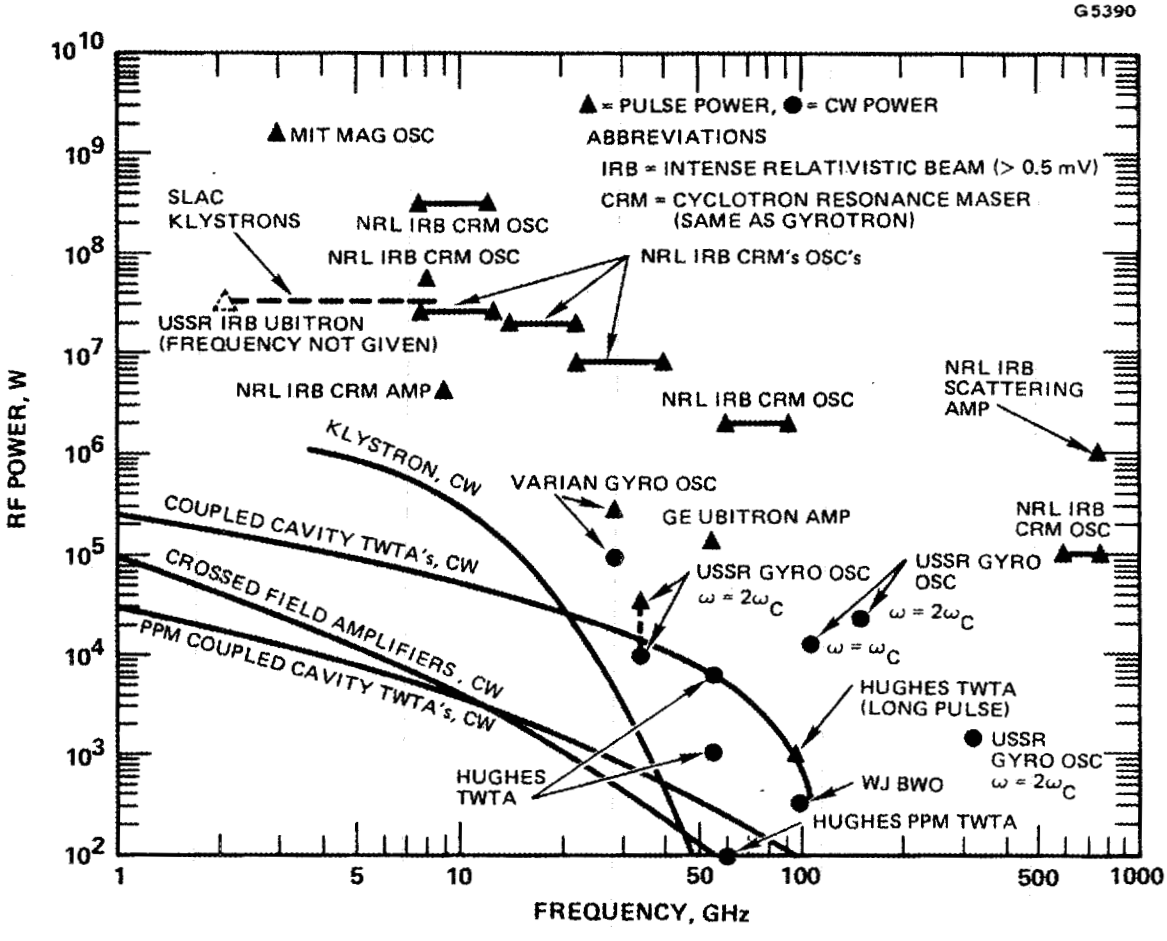

Figure 1-1 Plots of power versus frequency for high-power devices in the microwave and millimeter-wave regimes at start of program. (Dots are CW power, triangles are pulsed power).

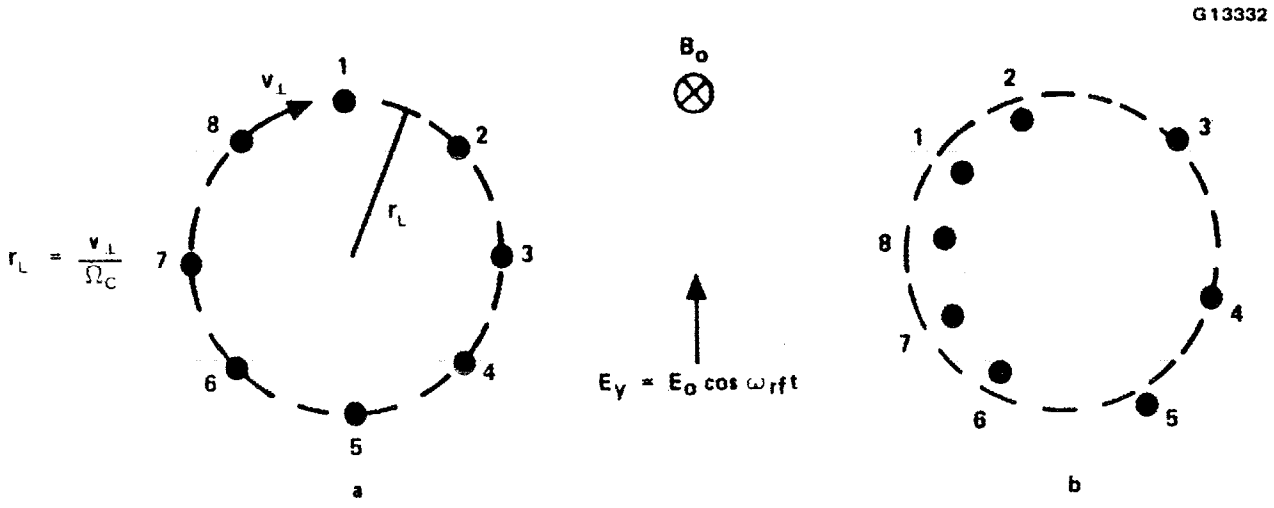

Figure 1-2 Electron distribution around the cyclotron orbit (a) before application of the electric field and (b) after several wave periods with the electric field present.

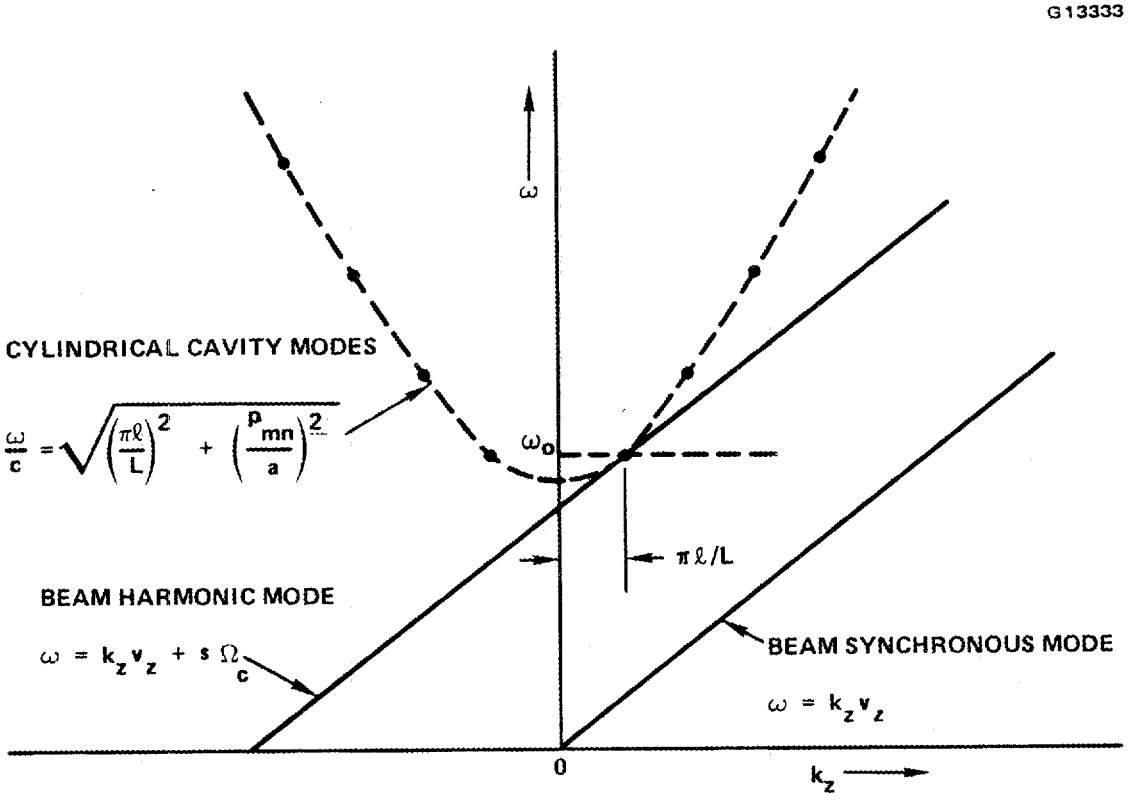

Figure 1-3 Conceptual dispersion diagram showing the beam and cavity modes in a configuration which will excite the TE_{mnl} cavity mode at the sth beam harmonic. Oscillation is expected at the tangency point of cavity (waveguide dispersion) and beam curves (found from the "slippage" condition $(\omega/k_z - v_z)(2\pi/\Omega_c) = s\lambda_g$). For a list of symbols, see Section 9.

The simplest way to exploit the ECM instability for rf generation is to pass an electron beam through a microwave cavity where beam-wave interaction can occur. Such a device, called a gyrotron, is shown schematically in Figure 1-4. Here the electrons are formed into a hollow beam by a magnetron-injection gun with a considerable amount of their energy in rotation. A gradually rising magnetic field compresses the beam in diameter and at the same time increases the orbital energy until approximately 2/3 of the beam energy is in rotation and the rotational frequency is almost equal to the frequency of the cavity. At this point the magnetic field becomes uniform and the beam enters an open cavity where the spinning electrons interact with the $TE_{mn\ell}$ mode of the cavity (m, n, and ℓ are the azimuthal, radial, and longitudinal mode numbers, respectively) as previously described. The spent beam then enters the region of decreasing magnetic field, undergoes decompression and impinges on the collector. The latter can also function as the output waveguide. In order to handle the power in the spent beam and the power dissipation in the window, the output waveguide tapers up from the cavity diameter to an appropriate value.

Specifications and operating parameters are given in Table 1-1, and a complete list of symbols is given in Section 9.

1.3 DESIGN CONSTRAINTS AND DEVICE APPLICATIONS

The device, a gyrotron oscillator, is intended for electron cyclotron resonance heating of fusion plasmas. ECRH is a most attractive method of plasma heating. Localized microwave heating is possible and simple launcher structures can be used, located sufficiently far away from the reactor plasma to eliminate long term launcher damage.

The gyrotron should be capable of operation into severely time-varying mismatches. The cavity, drift tube, and window must be adequately designed to tolerate the thermal loading due to ohmic heating. The collector must handle the full DC power of the beam. The gun must be arc-free and capable of high quality electron optics. The sheer power and frequency requirements dictate high order cavity and output modes; the circular symmetric modes (TE_{0n} class) are particularly attractive since their lack of radial electric field and axial currents at the wall offer lower cavity losses and significantly reduced transmission losses than non-symmetric modes of comparable mode number. This characteristic allows the use of lower order modes.

ORNL-DWG. 81-16887FED
G5393

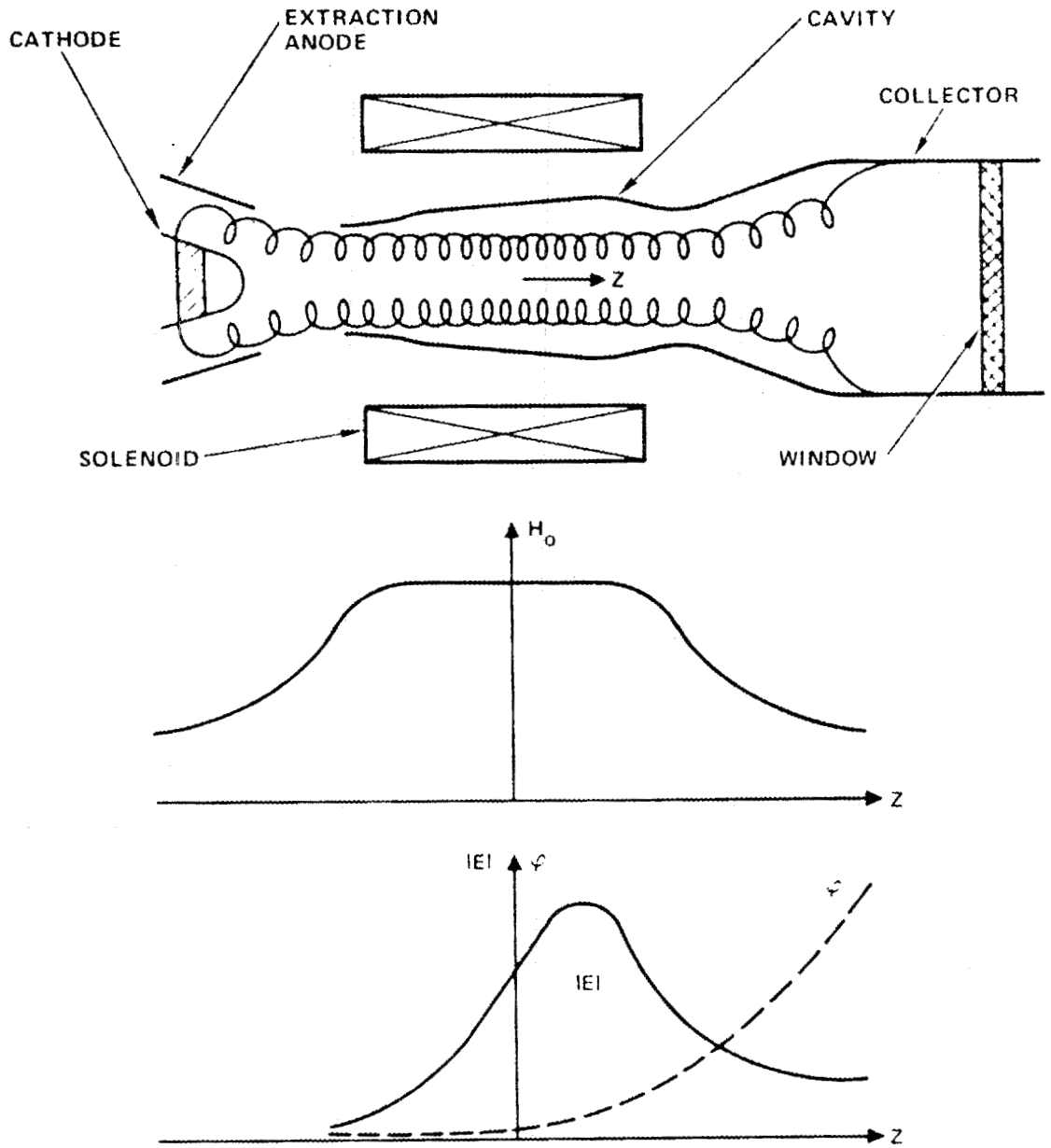

Figure 1-4 Schematic of gyrotron oscillator showing applied magnetic field and the rf field and gain in the cavity.

TABLE 1-1

GYROTRON SPECIFICATIONS

The Gyrotron	
Frequency	60 GHz
Power out	200 kW rf
Electronic efficiency	35%
Beam voltage	70-80 kV
Beam current	7-8 A
Transverse to longitudinal velocity ratio	1.5-2.0
The Power Supply	
Voltage rating	100 kV dc
Current rating	10 A
Anode supply voltage	0-35 kV dc
Anode supply current	20 mA
Heater supply voltage	0-15 V, ac
Heater supply current	15 A
Operating Regimes	
1. 10 s pulse length	
2. 1 ms-100 ms pulse length	
3. cw	

2.0 ELECTRON OPTICS AND MAGNETICS

2.1 GUN DESIGN

For reasons discussed in Section 1.3, the TE_{0n} mode was chosen early in the program as the desired class of circular cylindrical waveguide modes for interaction. Since the electric field strength, and hence the beam-wave coupling, is zero at the center of these azimuthally symmetric modes, the formation of hollow beams was particularly attractive. Also, since the ECM instability mechanism can only convert transverse beam velocity to electromagnetic radiation, it is beneficial to produce a beam of maximum rotational energy content in the interaction cavity. These characteristics are most readily satisfied by an electron gun of the magnetron-injection style.

In a magnetron injection gun (Figure 2-1), a beam of electrons is formed from a heated thermionic annular cathode ring in an appropriately shaped accelerating electric field immersed in an axial magnetic field. This combination of electric and magnetic fields imparts tangential and axial momentum to each electron. The axial magnetic field is then slowly increased from the gun to the cavity, keeping the magnetic moment of each particle essentially constant, until a significant fraction of total kinetic energy is in rotation at a cyclotron frequency about equal to the resonant frequency of the cavity.

Figure 2-2 shows schematically a suitable gyrotron electron beam in an interaction space. The beam velocity, usually normalized to the vacuum speed of light, is related to the relativistic gamma as

$$\beta = \frac{v}{c} = \sqrt{1 - \gamma^{-2}}$$

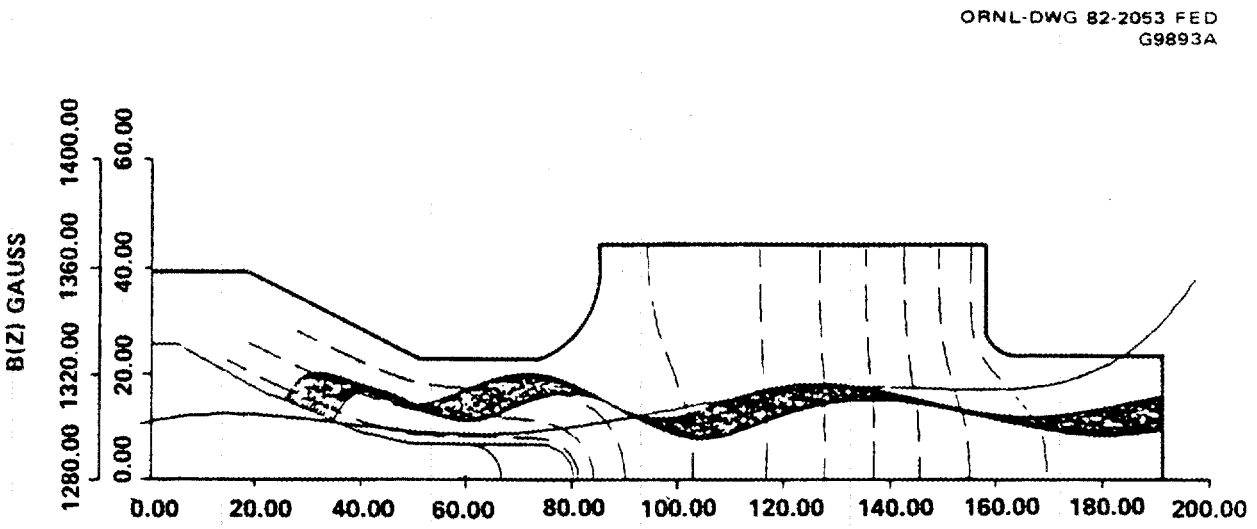

Figure 2-1 Magnetron injection gun.

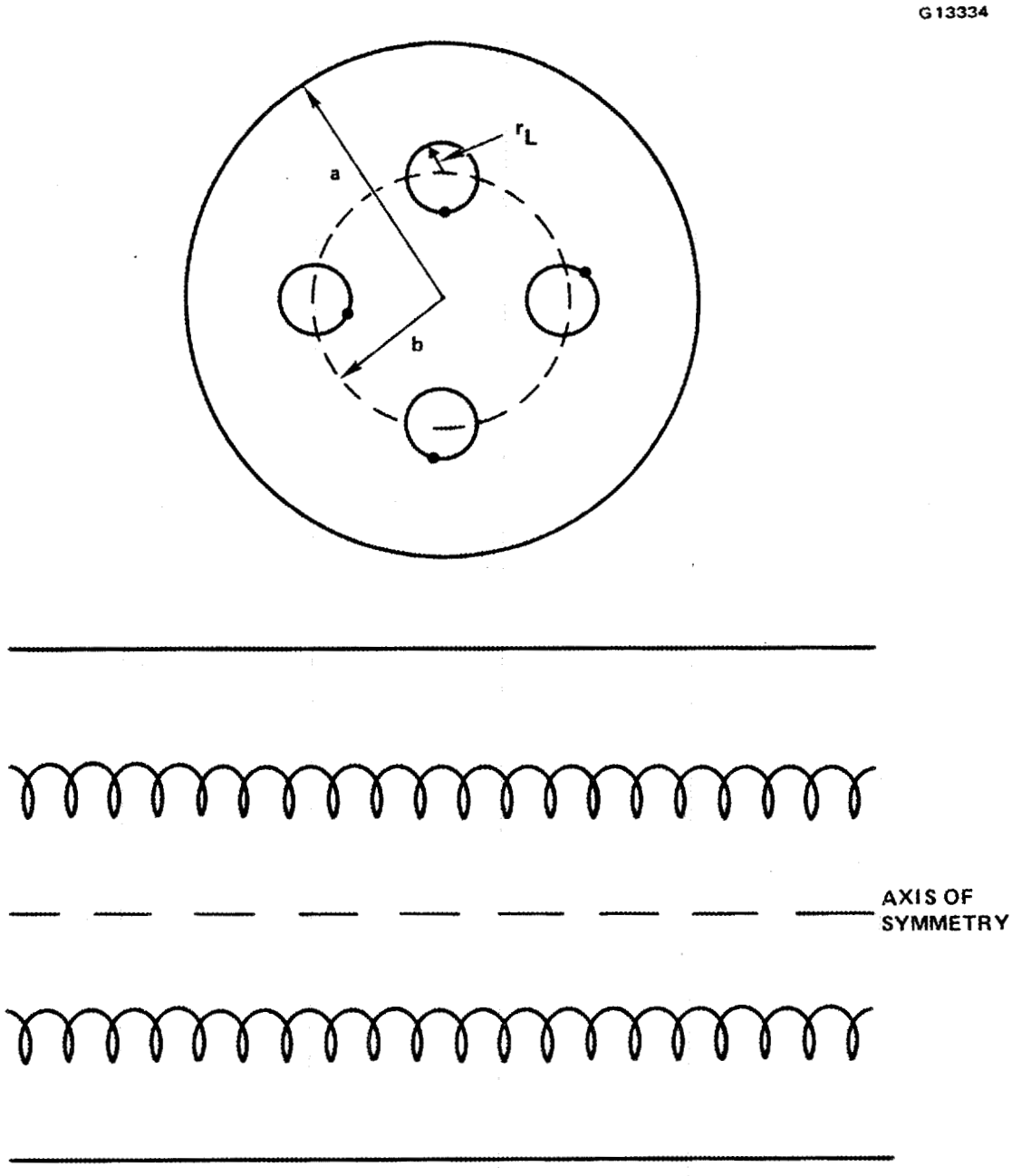

Figure 2-2 Annular gyrotron beam.

where γ is related to the beam voltage V by

$$\gamma = 1 + \frac{eV}{m_o c^2} = 1 + \frac{V(kV)}{511}$$

The degree of rotational energy content is given by

$$\frac{U_\perp}{U_{Tot}} = \frac{\alpha^2}{\alpha^2+1}$$

where

$$\alpha = \beta_\perp / \beta_z$$

is the ratio of tangential and axial velocity, and is controlled by either the voltage applied on an intermediate, non-intercepting electrode or by the magnetic mirror ratio of cavity to cathode magnetic fields. The latter adjustment, however, also changes the cyclotron frequency Ω_c and/or beam position in the cavity.

The annular width of the beam is ideally as close to $2r_L$, the rotational Larmor diameter of gyration, as possible. Finite emitter widths and space charge effects in the beam render this limit unattainable in practice. However, due to the choice of a relatively high order cavity mode (p large) and fundamental harmonic (s=1) interaction, the Larmor radius in the cavity is a small fraction of the cavity radius (Figure 2-3), i.e.,

$$r_L = \frac{v_\perp}{\Omega_c} = \frac{\beta_\perp cs}{\omega} = \frac{\beta_\perp}{p} a << a$$

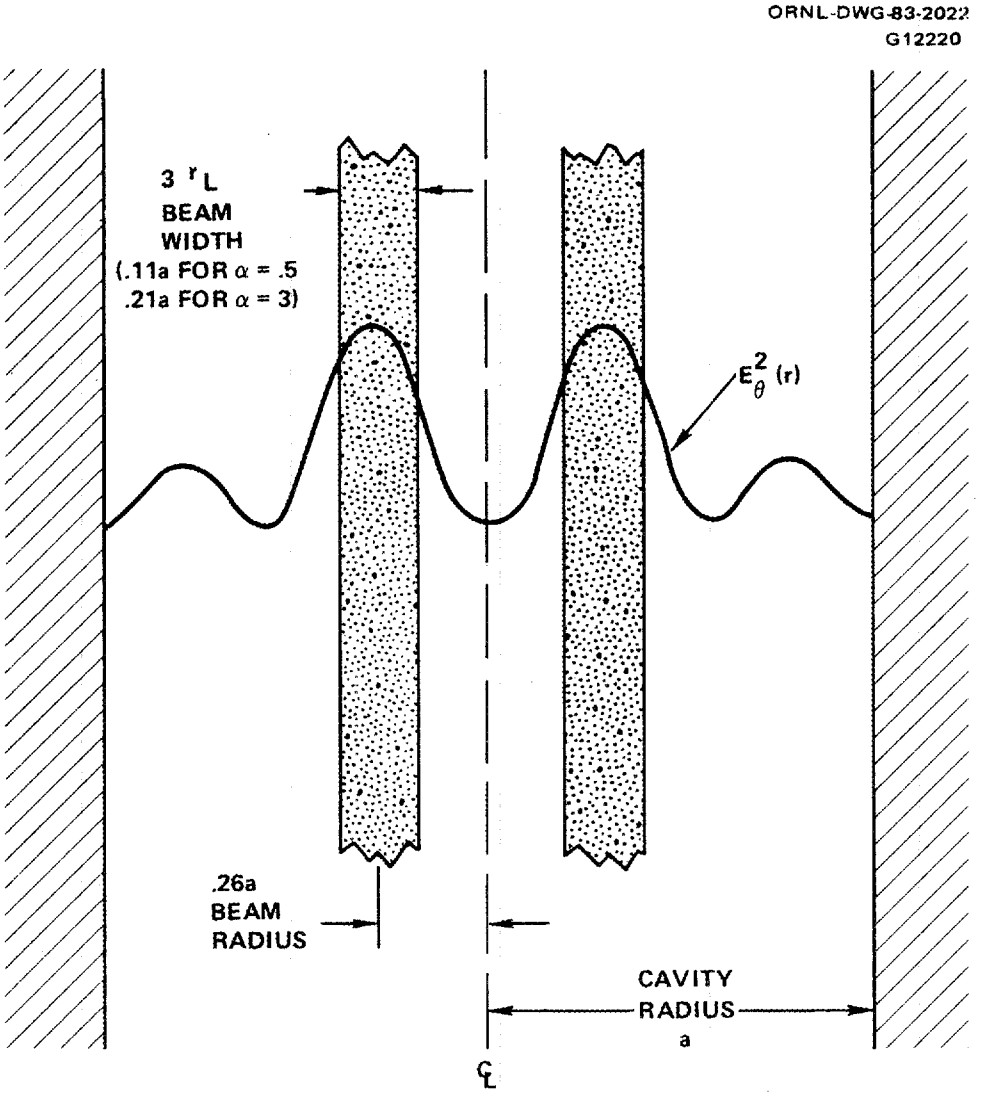

Figure 2-3 Schematic of beam position and width in a TE_{021} cavity.

Although the exact cavity dimensions were unknown during the early stages of gun design, it was known that the cavity would have to be long and close-to-cut-off just to ensure electrons would execute a sufficient number of cyclotron orbits within the interaction length.

Initial design goals are shown in Table 2-1.

Although the space-charge-free electron motion between the concentric cathode and mod anode can be given in closed form[1] which, along with adiabatic scaling of particle motion in the drift tube region, can be used for initial design and trade-off analyses, detailed gun analysis requires the use of a trajectory tracing, interactive computer program. A rectangular mesh (Herrmannsfeldt) computer code used in the early stages of the development effort was eventually replaced by a deformable mesh electron optics program with modifications for highly accurate modeling of the emission process under realistic gyrotron operating conditions. Both these programs consider space charge effects of the beam by repeatedly solving Poisson's equation at distinct mesh points subject to the space charge "laid down" by the trajectories in the previous iteration.

TABLE 2-1

INITIAL BEAM DESIGN GOALS

Beam voltage	V_K = 70-80 kV
Beam current	I_K = 0-10 A
Current density at emitter	J_K < 10 A/cm^2
Beam guiding center (for efficient interaction)	b = 1.8412 a/p_{mn} = 1.84 $\lambda/2\pi$ = .146 cm
Cavity magnetic field	B_o = 22.9 - 24.0 kG
Perpendicular to axial velocity ratio in cavity	α > 1.5
Annular beam thickness in cavity	< 4 r_L

The original gun design, with computed performance parameters of $\alpha = 2.35$ with a transverse velocity spread of 1.1% was designed for operation in an applied magnetic field essentially constant in the gun region. Early test results, indicating tapered gun magnetic fields to be preferable (Section 5), prompted a slight electrode redesign (cathode snout shortened) to optimize performance in the empirically derived magnetic field. The computed results of this final gun design, shown in Figure 2-4, indicate high α is obtainable for a reasonable range of cathode fields. Beam width in the cavity is 3.4 r_L; cathode current density is 5 A/cm^2 at 8A emission.

Later guns featured effective thermal isolation of the emitter region from the rest of the cathode electrode body (Figure 2-5) to guarantee emission is restricted to the emitter strip and ensure arc-free operation. (This particular design also allows easy implementation of oil cooling at a later date if CW test conditions require even cooler electrode temperatures. Unfortunately, the untimely termination of CW test facility funding rendered this untestable, although the existing design has performed flawlessly to 100 ms pulsewidths.)

2.2 SOLENOID DESIGN

Initial design constraints on the superconducting solenoid were for a constant (flat) axial magnetic field throughout the gun region, a field of varying slope in the cavity region, and a slowly increasing field in between. This would have to be accomplished with a warm bore large enough to accomodate slipping in the gun, drift tube, cavity, uptaper, and their corresponding cooling and support envelopes. These requirements were satisfied by the coil arrangement illustrated in Figure 2-6, provided by the Magnetic Corporation of America, with a 5.0 inch warm bore diameter.

The axial field due to a uniform current density coil, at any point along the axis, is found by integrating the Biot-Savort law for an incremental current element ($\vec{dB} = (\mu_o/4\pi)\ \vec{dI} \times \vec{dr}/|\vec{r}|^3$) azimuthally, axially, and radially (from inner to outer coil radii) for each distinct coil and summing their individual contributions. The resultant, initial axial field profile is shown in Figure 2-7.

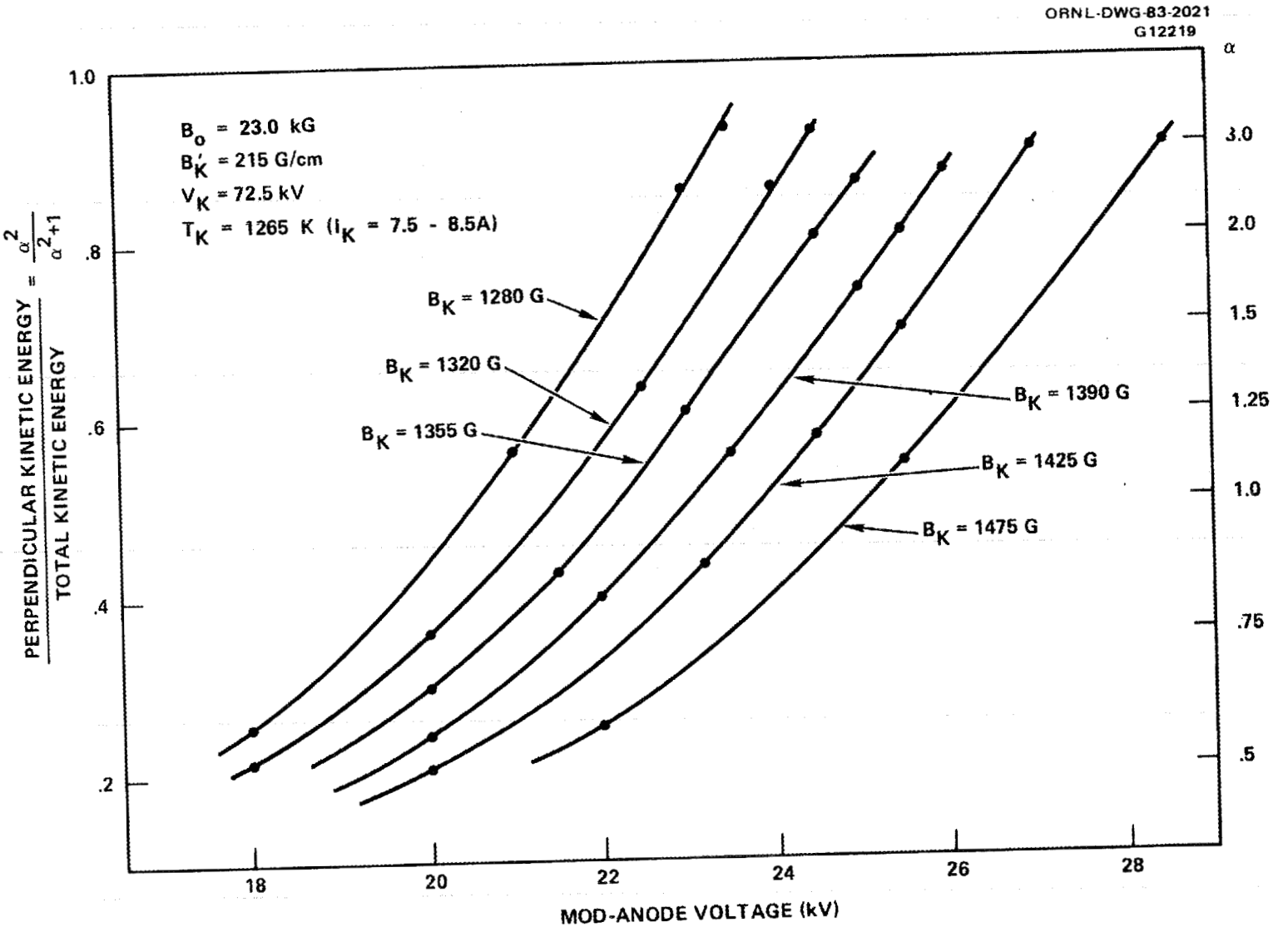

Figure 2-4 Computed results of the Hughes 917H final gun design.

E4683

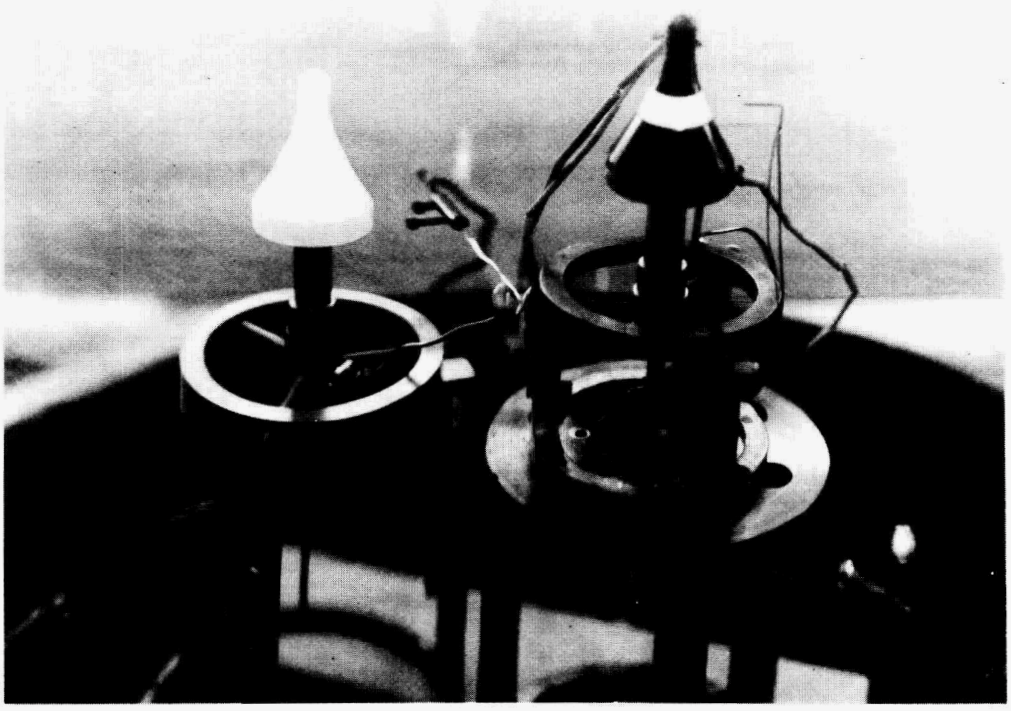

Figure 2-5 Original (left) and thermally isolated cathode designs.

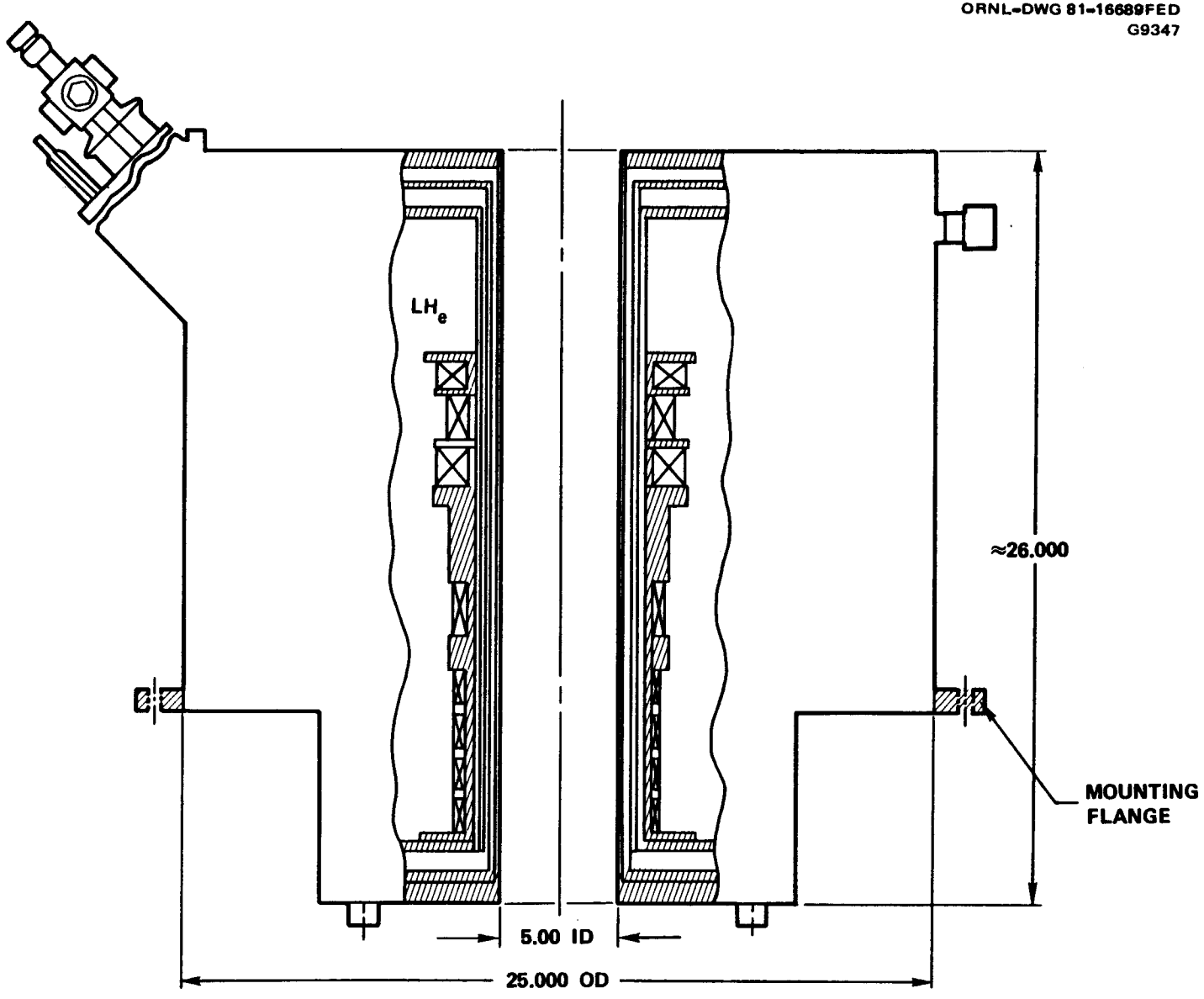

Figure 2-6 Totally enclosed, eight coil cryostat permitting sufficient access to Gyrotron.

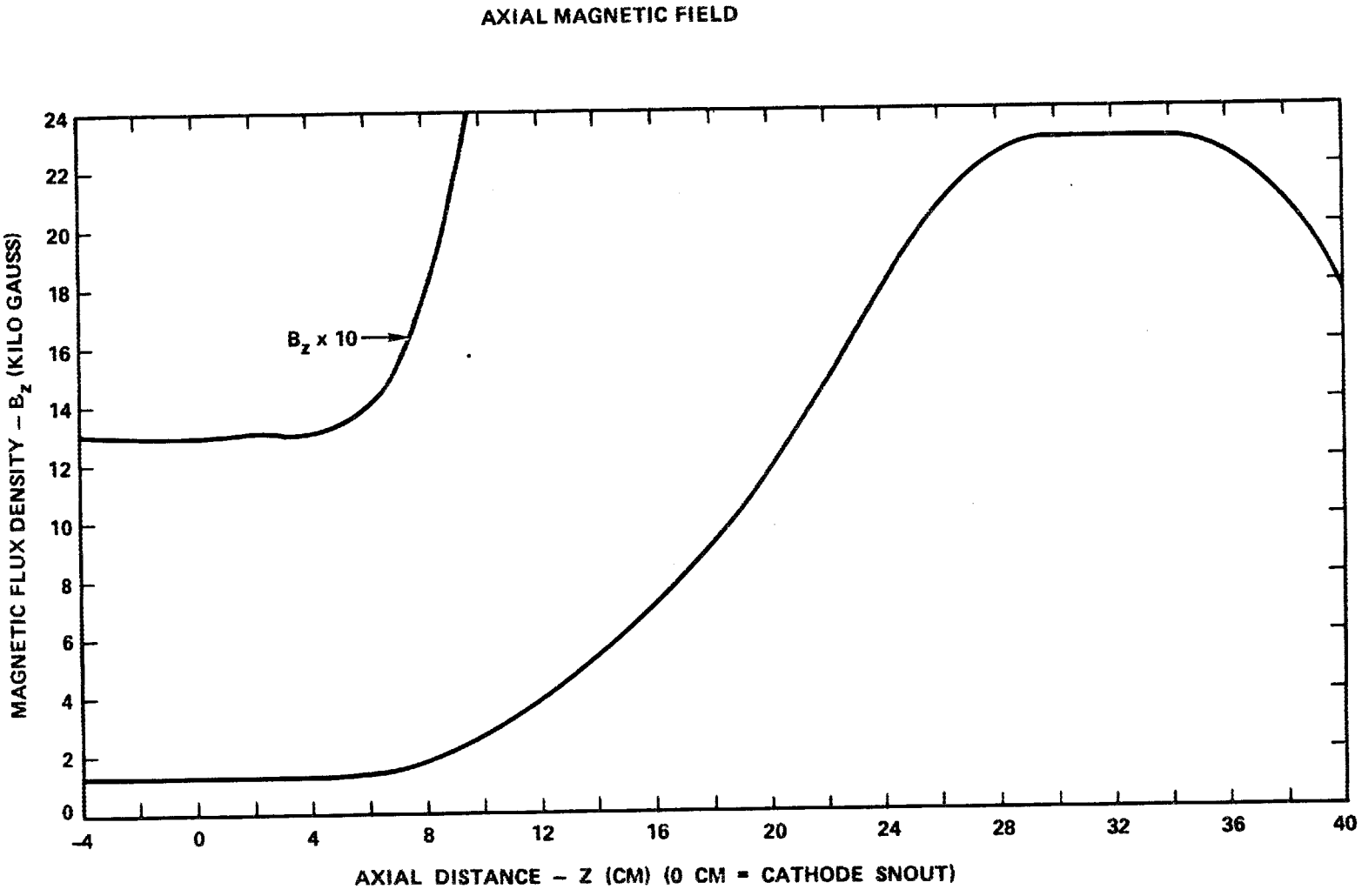

Figure 2-7 Axial magnetic field for ORNL 60 GHz gyrotron.

Transverse fields should be kept to a minimum. Even the simplest integration of the Lorentz force equation for radial deflection of an axially-directed electron:

$$m\ddot{r} = m\left(\frac{dz}{dt}\right)^2 \frac{\partial^2 r}{\partial z^2} = -ev_z B_r$$

$$r(z) = \frac{-\eta}{c}\iint \frac{B_r(z)}{\beta_z(z)}\, dz^2$$

shows deflections up to centimeters possible using typical gyrotron beam parameters and transverse fields as low as 100 gauss.

Considerable flexibility has been afforded by the multi-coil nature of this superconducting solenoid system. Alternate field profiles (Figure 2-8) could be experimentally tried by changing the individual current settings of the eight separate coils.

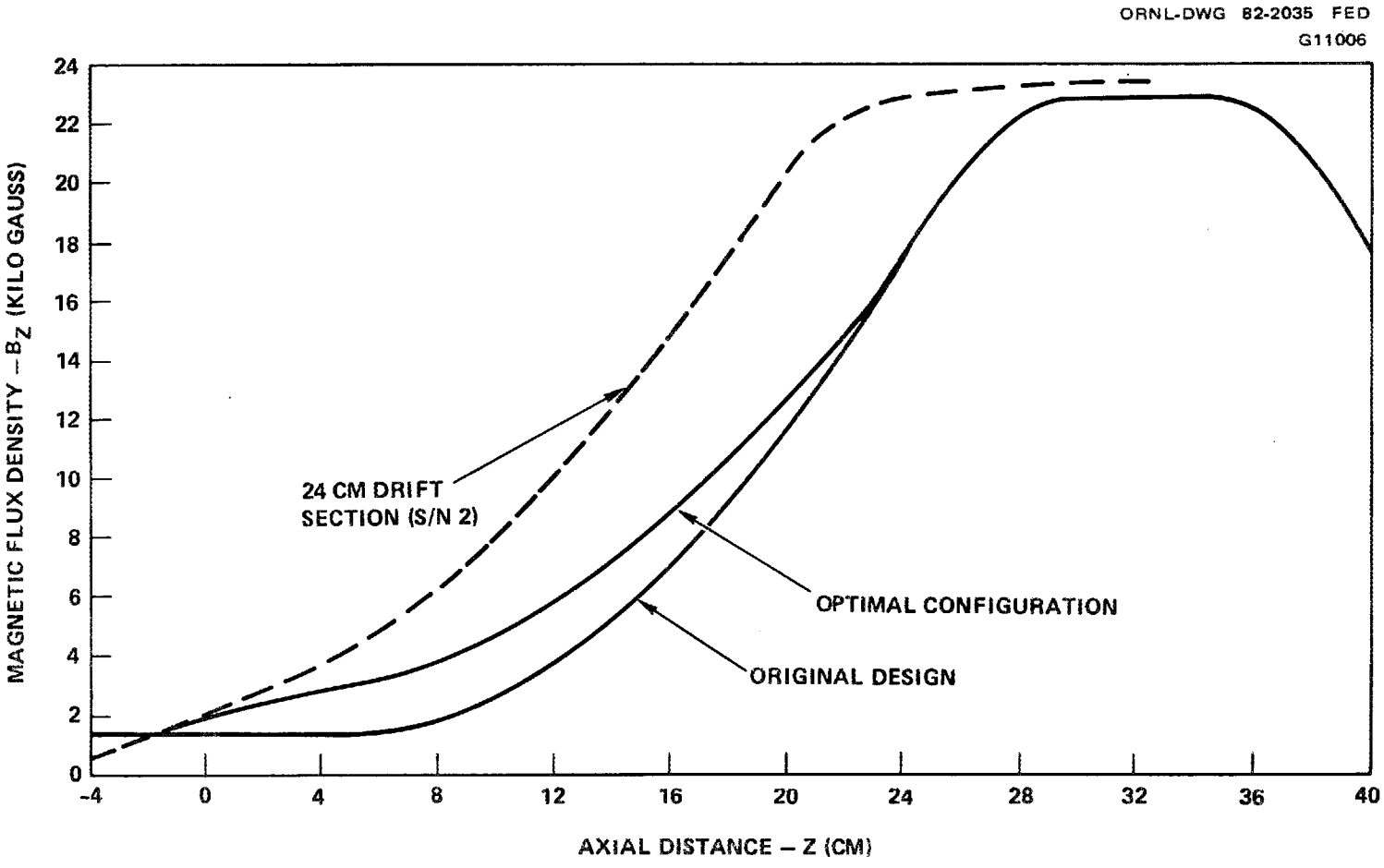

Figure 2-8 Axial magnetic fields for ORNL 60 GHz gyrotron.

3.0 CAVITY DESIGN AND RF TRANSMISSION CONSIDERATIONS

3.1 INTRODUCTION; COMPUTER PROGRAM DEVELOPMENT

Achieving high power and efficiency over a reasonable range of operating parameters without interruption by "competing" modes is the primary goal in cavity design. Parameter space must also allow a smooth control of power over a 17 dB dynamic range.

The efficiency achievable with a gyrotron oscillator is highly dependent on the shape of the cavity's physical dimensions and the profile of the applied magnetic field. Approximating the RF electric field of the cavity (by assuming its axial dependence is sinusoidal, Gaussian, or some other presumed shape) can be useful for developing a "feel" for the approximate dependence of efficiency on length and beam parameters. However, precise determination of the field structure is essential for accurate modelling of a given design. This can be done for arbitrary degrees of cavity irregularity by using a large partial differential equation solver such as SUPERFISH (Figure 3-1) or, at a considerable cost savings and with easy allowance for end effects, by the use of slowly varying waveguide theory. SVWGT solves the complex eigenvalue equation

$$E''(z) + \left(\omega^2/c^2 - p^2/a^2(z) \right) E(z) = 0$$

subject to user-defined boundary conditions at the ends by iterating with differing values of $\omega = \omega_R + i\omega_I$. This equation results from substituting assumed solutions of the form

$$E_\theta = E(z)\, J_m' \left(\frac{pr}{a(z)} \right) \cos m\theta\, e^{j\omega t}$$

which holds for cavities made up of slowly and smoothly varying sections of waveguide into Maxwell's equations. This then gives E(z) (the axial RF field

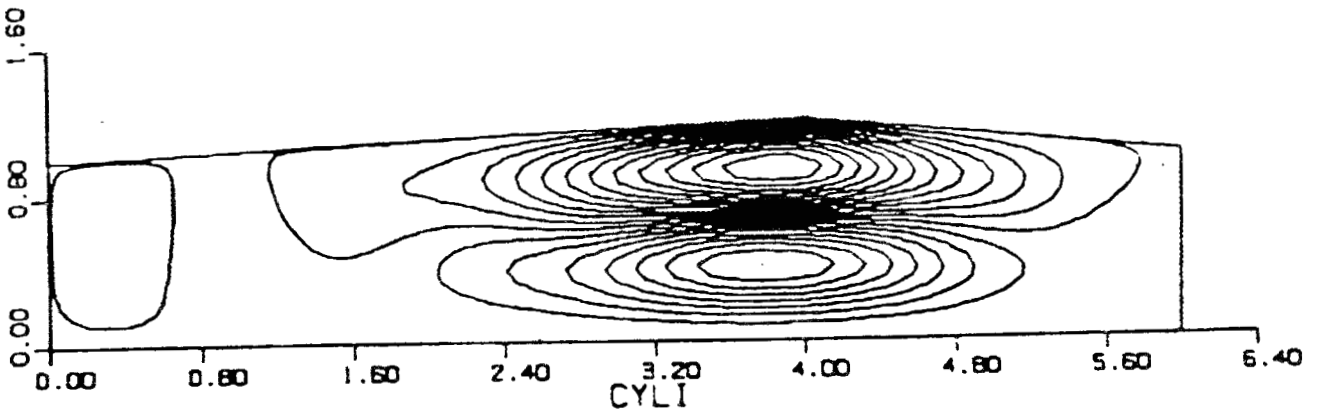

(a) TE_{021} MODE

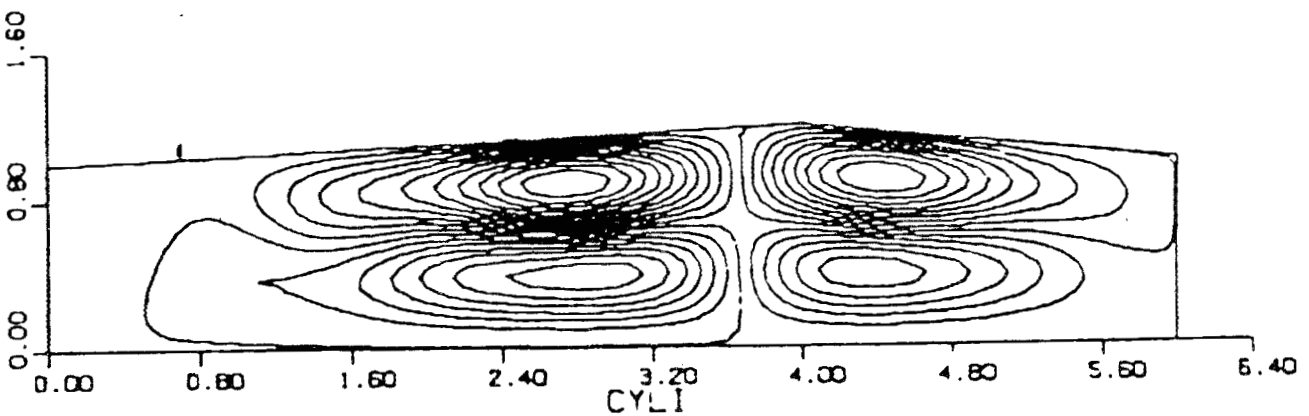

(b) TE_{022} MODE

Figure 3-1 Field plots of azimuthally symmetric tapered cavity modes.

profile), the resonant frequency ω_R, and the resonant Q factor ($= \omega_R/2\omega_I$, since E_θ decays as $e^{-\omega_I t}$). Effects of beam loading can be accounted for by inclusion of a current source term.

This computer generated RF field profile (Figure 3-2) is used as input to a large signal efficiency program which tracks a sufficient number of particles (usually about 50) of differing entrance phase according to the relativistic equations of motion. The calculation is subject to the RF electric and magnetic fields, the applied axial magnetic field of the superconducting solenoid, and the beam conditions of voltage, radial position, and alpha (Figures 3-3, 3-4.) The degree of stored cavity energy is then successively varied and the RF output power equated to the kinetic energy lost by the test particles (Figure 3-5). This allows the self-consistent calculation of either beam current, Q, or frequency given any two of the remaining parameters, since stored cavity energy scales as $QI\lambda$.

Linear ECM theory is adequate for calculating start oscillation power (or current) thresholds (Figure 3-6). This proves exceptionally useful in predicting the degree to which mode competition is to be expected for a given mode and cavity design.

3.2 MODE COMPETITION

Mode competition is said to occur when a desired mode is unattainable at a given combination of parameters due to the intrusion of an unwanted resonant mode. Proper gyrotron design must aim at ensuring the desired region of operation is free from such debilitating mode competition. The otherwise desirable TE_{0nl} class of modes is especially susceptible to mode competition from the TE_{2nl} modes, particularly for higher values of n, because

- The similarity in Bessel roots, p_{mn}, of the TE_{0n} and TE_{2n} assure that the resonant frequencies will be similar, hence the mode separation in magnetic field space will be small (and increasingly smaller for increasing n).

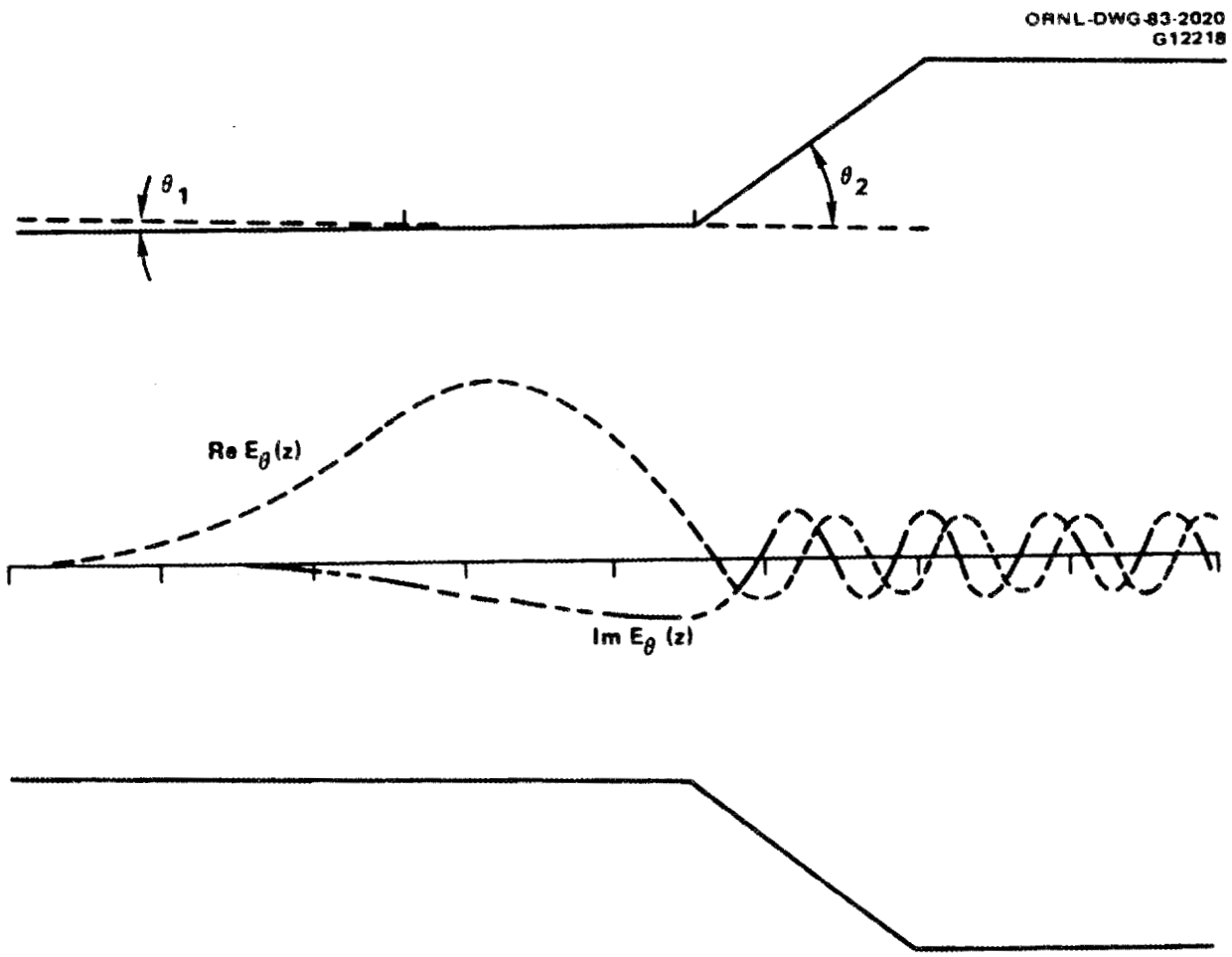

Figure 3-2 Cavity configuration.

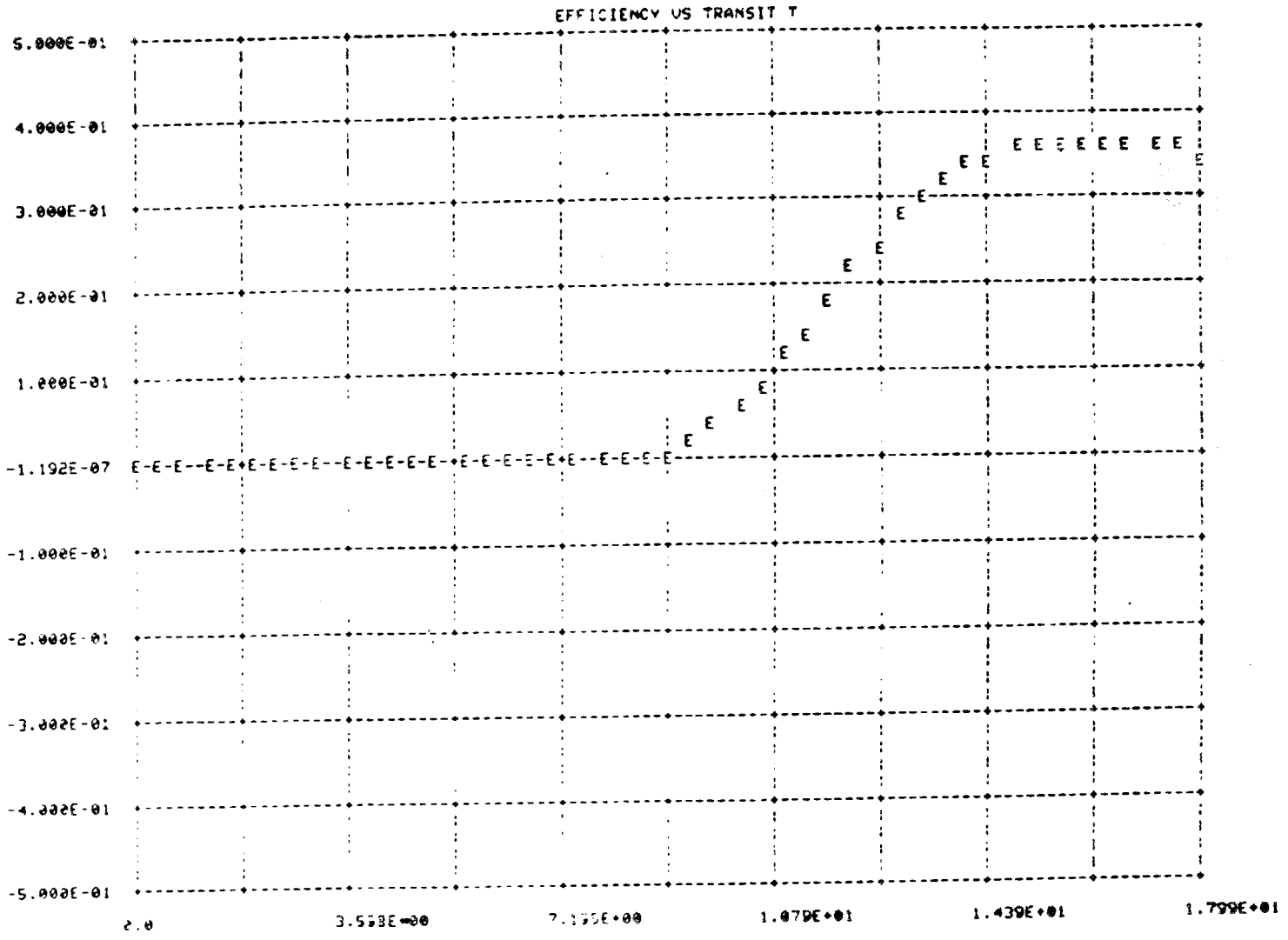

Figure 3-3 Overall efficiency versus transit time normalized by the cavity radius divided by the speed of light.

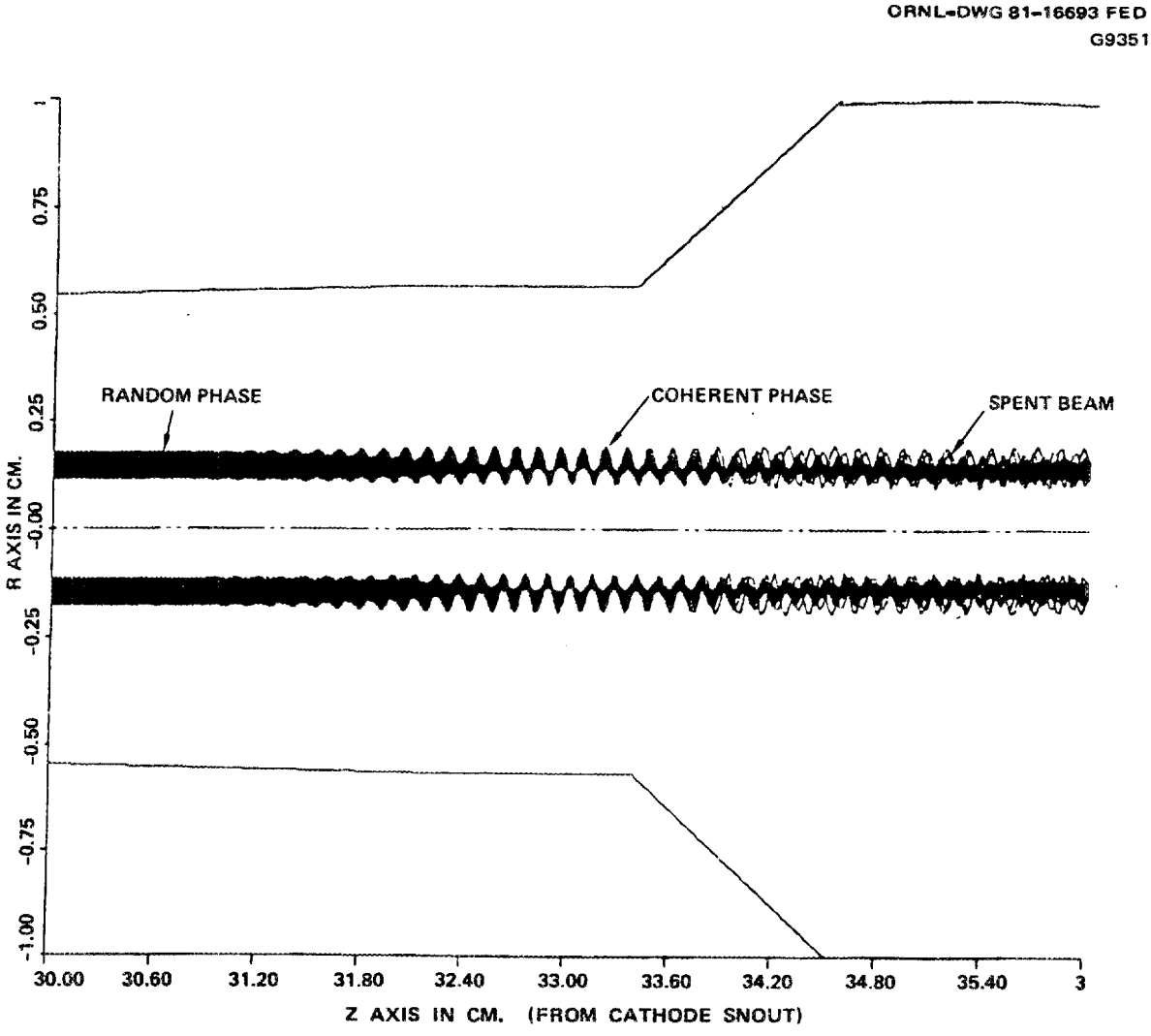

Figure 3-4 Phase bunching of hollow electron beams.

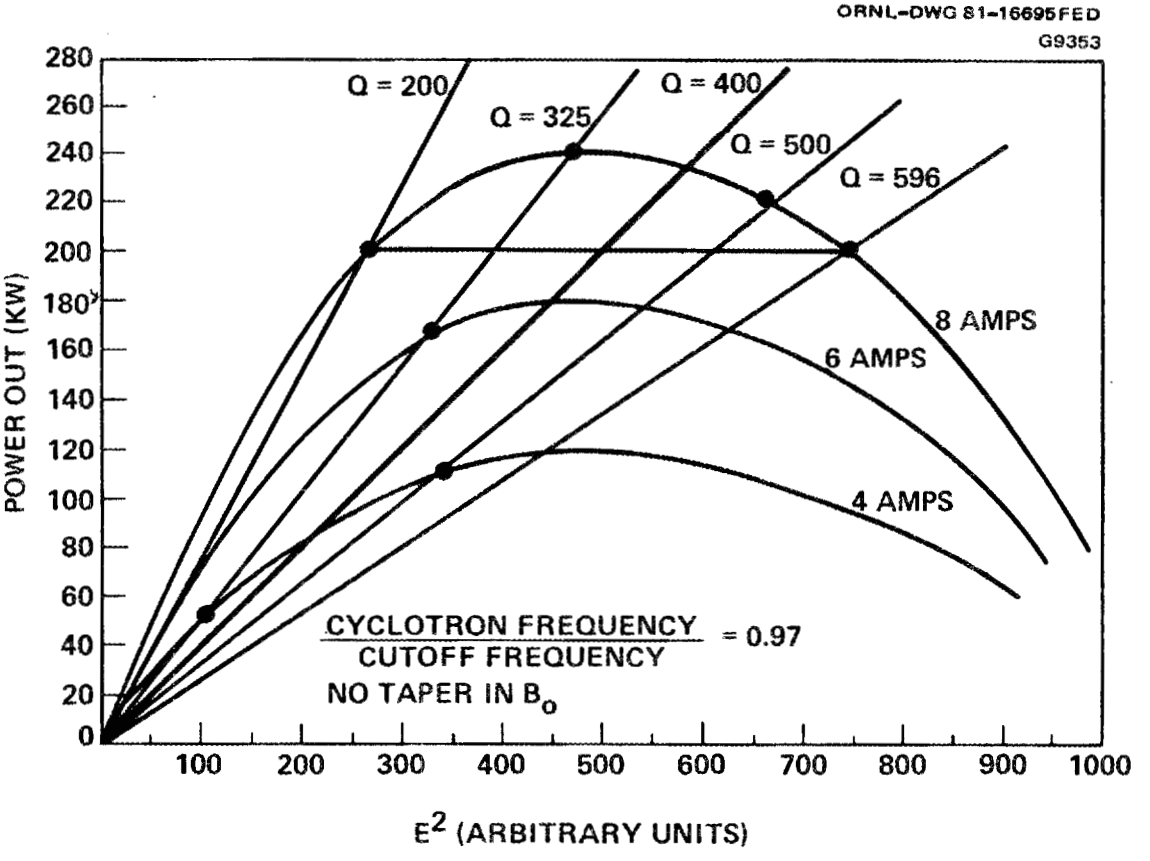

Figure 3-5 Efficiency analysis of a 60 GHz gyrotron cavity design at a fixed magnetic field, beam position and voltage.

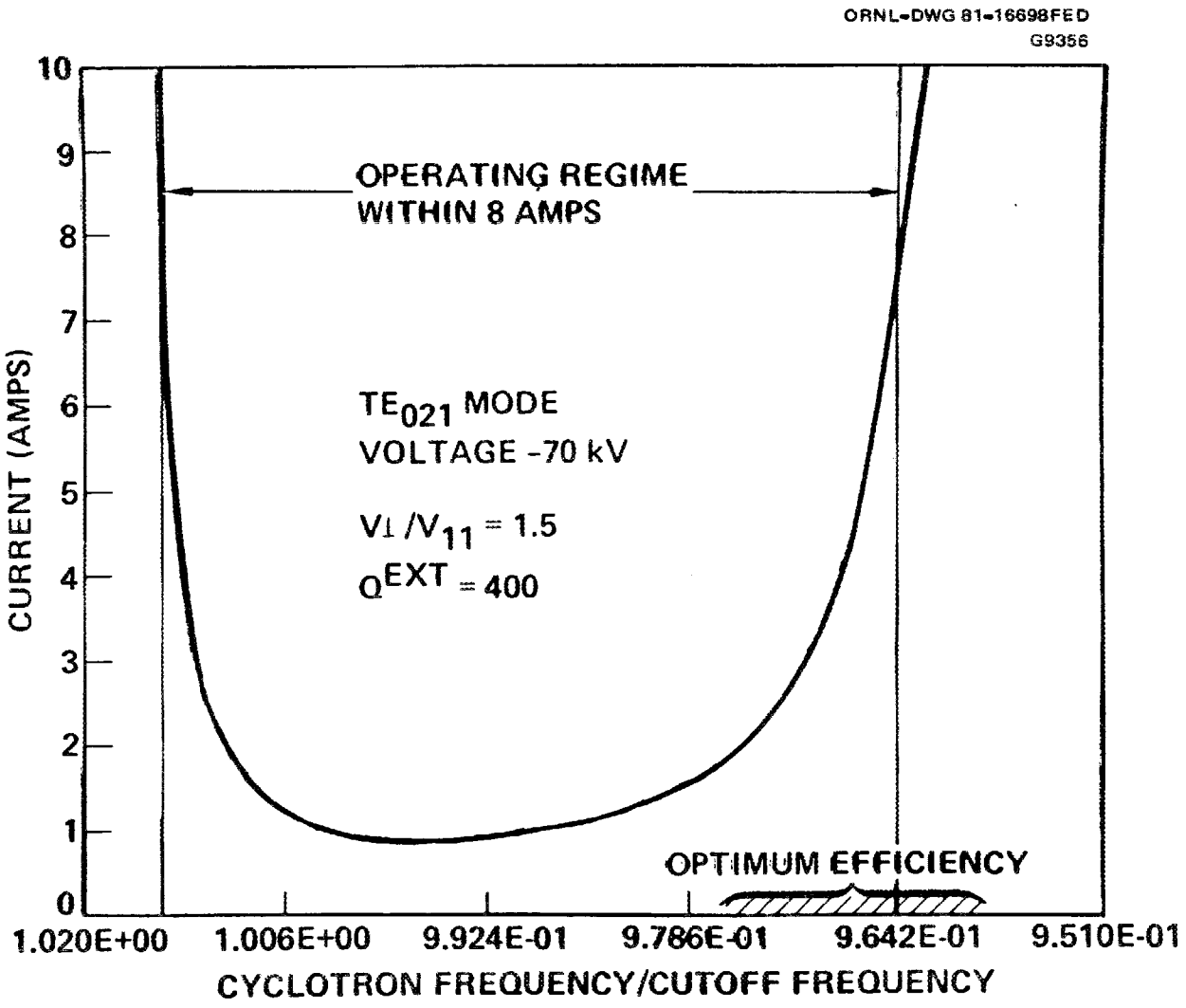

Figure 3-6 Start-up threshold analysis.

- A similar radial rf field dependence and beam coupling dependence of the "negatively" polarized TE_{2n} mode and the symmetric TE_{0n} mode.

Some benefit can be had by determining regimes particularly free of mode competition (though probably low in efficiency) and starting a pulse in these regions. By then moving into the high efficiency region, one can take advantage of mode locking, in which the threshold for oscillation of an unwanted mode is increased about four-fold from that of a single mode analysis. This is particularly useful for CW conditions in which there is sufficient intrapulse time to vary magnetic field as well as alpha.

3.3 EFFICIENCY ENHANCEMENT

Using sinusoidal axial rf field distributions and uniform applied axial magnetic fields, calculated perpendicular conversion efficiencies ($\eta_\perp = \eta(\alpha^2 + 1)/\alpha^2$) are limited to approximately 55 percent. However, by skewing the rf field profiling (by tapering the cavity walls) and/or profiling the applied magnetic field, perpendicular efficiencies in excess of 80 percent have been calculated by large signal analyses. HEDD has chosen to pursue wall profiling alone because

- Flat magnetic fields allow additional ease in correlating experimental results with theoretical efficiency predictions; the precise magnetic field is known at any point in the cavity since the magnetic field is kept essentially constant and decreased quickly to below threshold conditions in the cavity's output.

- Wall profiling allows additional frequency separation of $\ell = 1$ and $\ell = 2$ axial modes (although the ℓ^{-2} dependence of Q for iris-coupled designs was believed adequate in itself for discrimination of higher order axial modes).

3.4 INITIAL AND FINAL CAVITY DESIGN

The initial 60 GHz gyrotron employed a long, high Q cavity designed for low oscillation thresholds. Successful demonstration of oscillation and TE_{02} output

in the first test device prompted the implementation of a refined, lower Q, higher efficiency cavity design (Figures 3-7, 3-8). Peak thermal wall loading under CW conditions (due to ohmic losses in copper walls) is 550 W/cm^2. The cavity has external, brazed-on cooling fins and uses water coolant.

3.5 MODE PURITY AND TAPER DESIGN

Although not a distinct program requirement, mode purity was recognized as a definite design goal because

- high mode purity simplifies system waveguide component design (transducers, couplers, antennas)
- since mode conversion is usually accompanied by increased reflection at the discontinuity, a low mode conversion system is in general, a better matched system.
- low mode conversion would reduce the likelihood of potential problems with extremely high order trapped modes in the collector section.

A computer program utilizing the coupled mode "telegraphers" equations was written to evaluate different taper designs. (See example of Figure 3-9.) Tapers were designed, using raised cosine and multi-circular arc profiles, that were vastly superior to linear tapers by 10 to 20 dB of additional mode suppression.

3.6 DRIFT TUBE DESIGN

A well designed gyrotron drift tube:

- prevents, as much as possible, leakage of cavity fields into the drift section
- allows uninhibited beam transmission from gun to cavity, adequately preventing any ECM or other instability from altering the smooth adiabatic compression and distorting the minimal velocity spread.

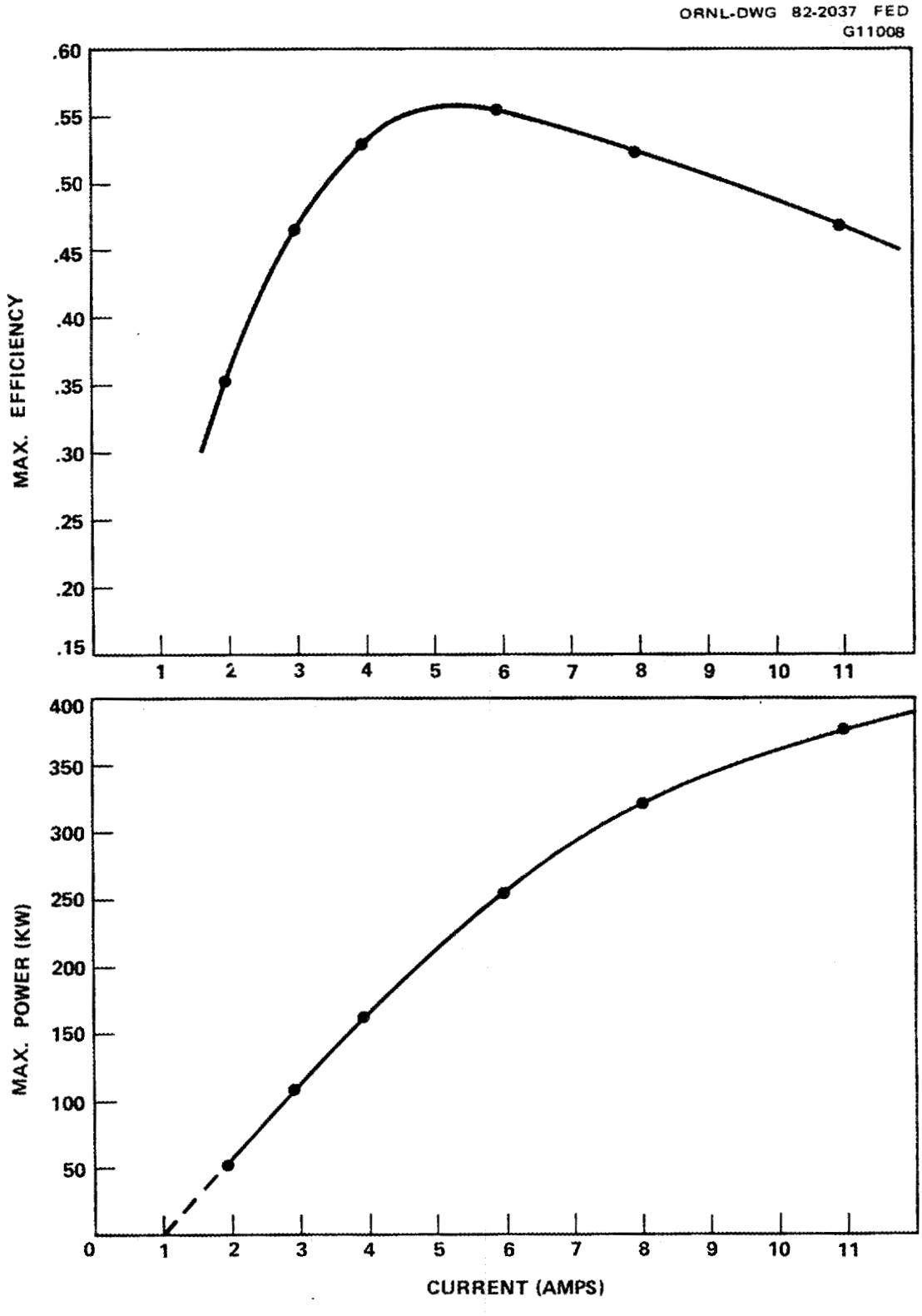

Figure 3-7 Computed power and efficiency for the revised cavity design.

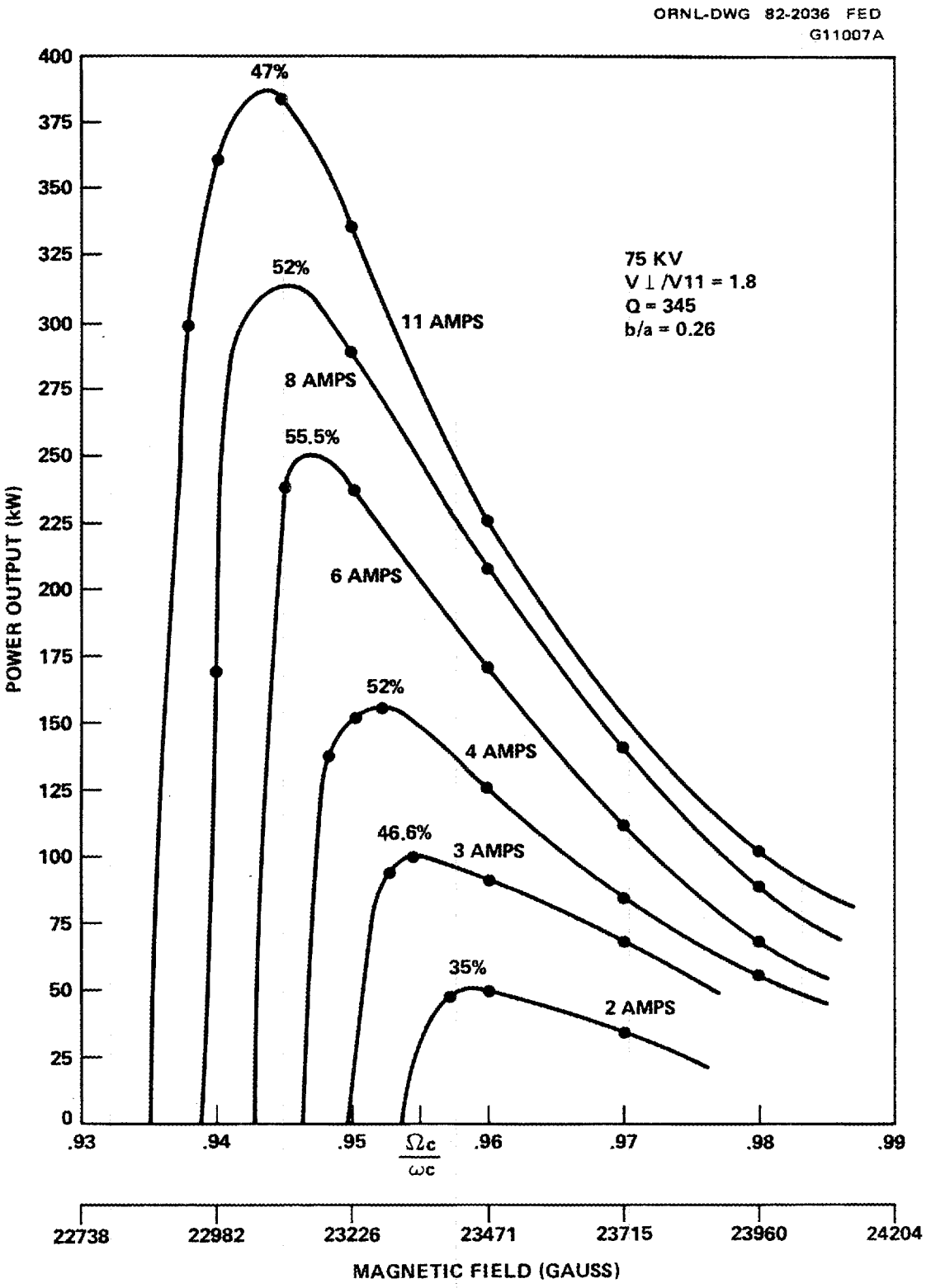

Figure 3-8 Power out vs. magnetic field predicted for the revised cavity design.

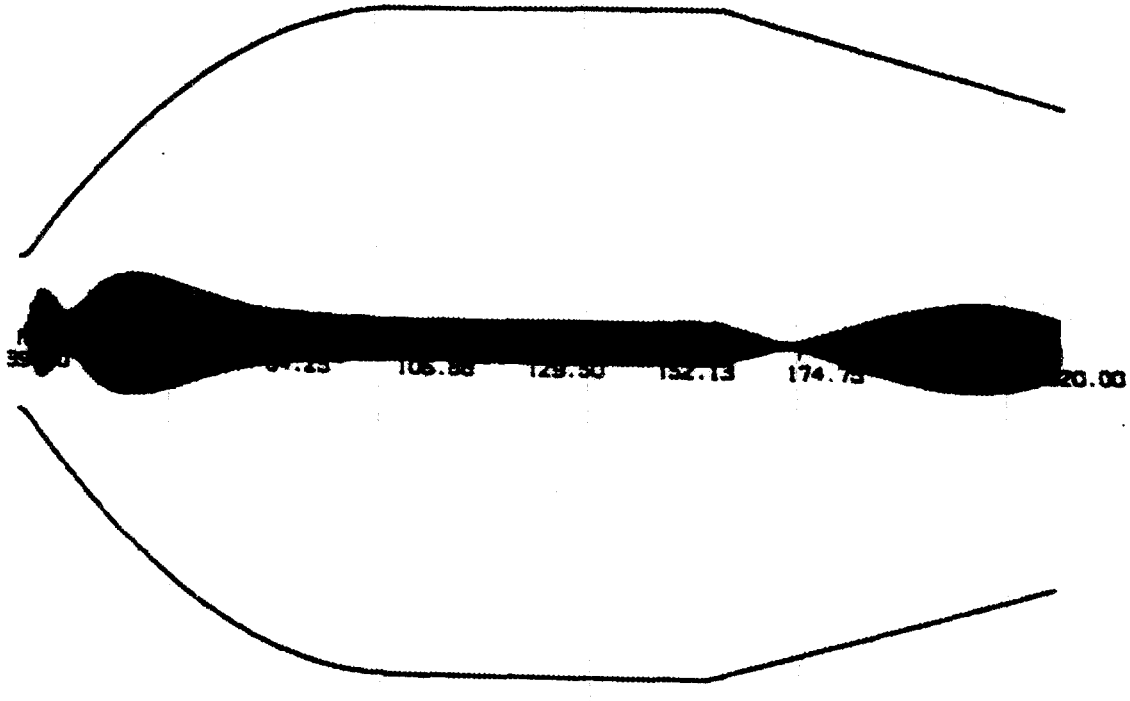

Figure 3-9 Sample computer output showing the combined "up" taper, collector region, and "down" taper with 17 dB overall suppression of the TE_{01} mode. Shading shows the relative amplitude of the TE_{01} mode.

- contains sufficient metallic grounded elements to prevent electrostatic charging of any drift tube ceramic parts

- is sufficiently rugged, mechanically and thermally, to withstand the dissipated CW power due to inevitable low level interception as well as any attenuated RF.

A drift tube design (Figure 3-10) was chosen which satisfies the above criteria. It consists of stacked discs of copper rings and beryllia (doped with 40 percent silicon carbide) arranged to prevent any axial periodicity and with decreasing axial thickness as rotational beam energy increases.

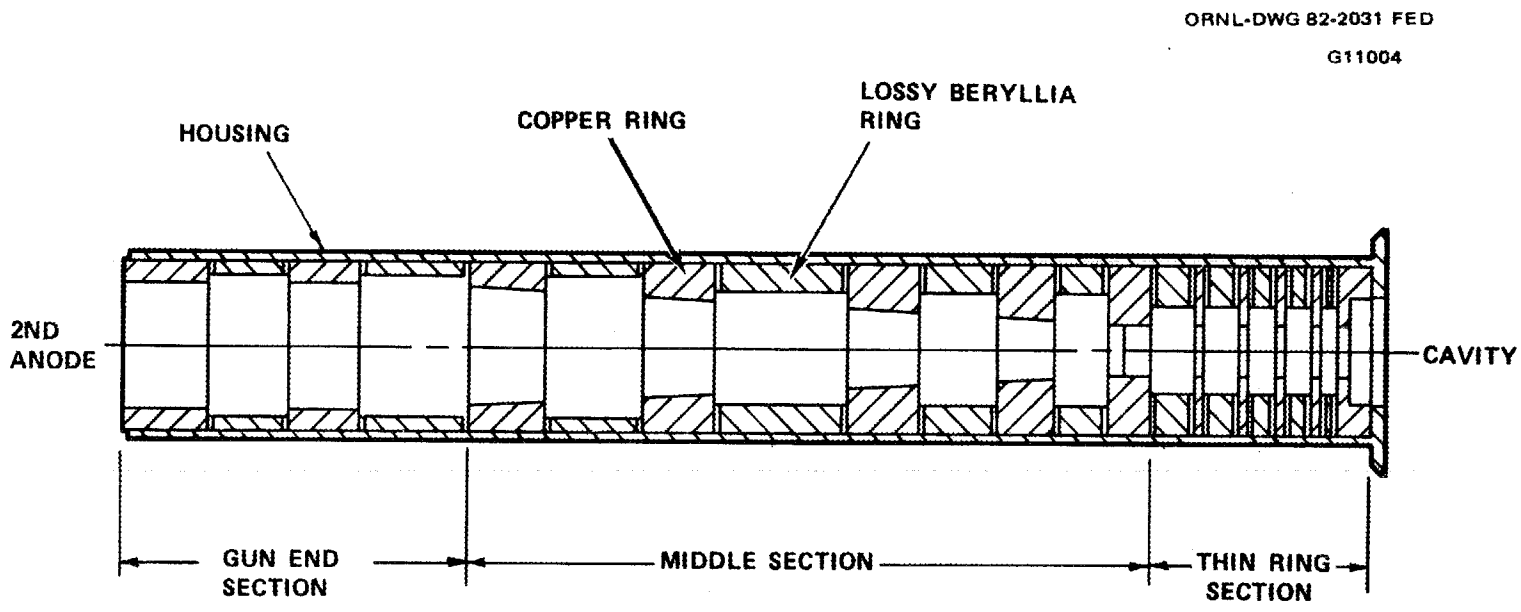

Figure 3-10 Lossy drift section.

4.0 THERMAL AND MECHANICAL DESIGN

4.1 BEAM COLLECTION

Although other designs were considered (Figures 4-1, 4-2) an axisymmetric design was chosen (Figure 4-3) for its anticipated improved rf match to the interaction cavity and simpler design.

Large signal analyses of DC and spent (after interaction) beam distributions (Figure 4-4) indicated a 3.5 inch diameter collector would be adequate if an efficient cooling scheme was chosen. Utilizing an external fin geometry (Figure 4-5) a thermal design was generated that provided effective cooling with a reasonable flow rate and pressure drop. A mock-up (Figure 4-6) was built and successfully tested to 345 gallons/minute to verify the mechanical integrity of the design.

The need to empirically determine the beam distribution within the collector soon became apparent, particularly as the severe magnetic field incongruities were discovered (Section 5.3). Magnetic shunts and/or spreading coils could then be added at low duty to ensure safe CW operation. The use of a thin-walled diagnostic collector on early tubes allowed reliable distribution data to be taken. Different techniques were used:

- The use of x-ray sensitive photographic film (Figure 4-7) was prohibitively slow, since every parameter change necessitated another lengthy exposure, development and analysis of the exposure density. A proposed scheme (Figure 4-8) using photodiode-backed scintillating crystals allowed real time, accurate analysis but at a cost judged prohibitive.

- Distinct thermocouple readings (Figure 4-9) were somewhat slow and required a large number of detectors to resolve small hot spots with attendant data handling complexity.

- Infrared imaging with the Hughes Probeye camera (Figure 4-10) was judged as most practical for beam distribution studies.

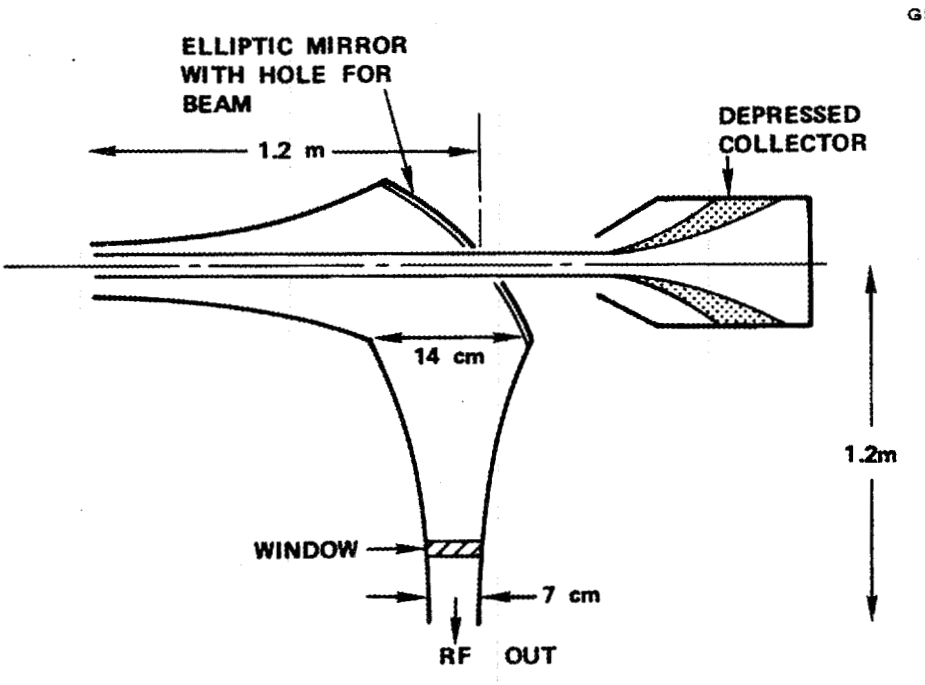

Figure 4-1 Method of extracting RF through a right angle bend using an elliptic mirror.

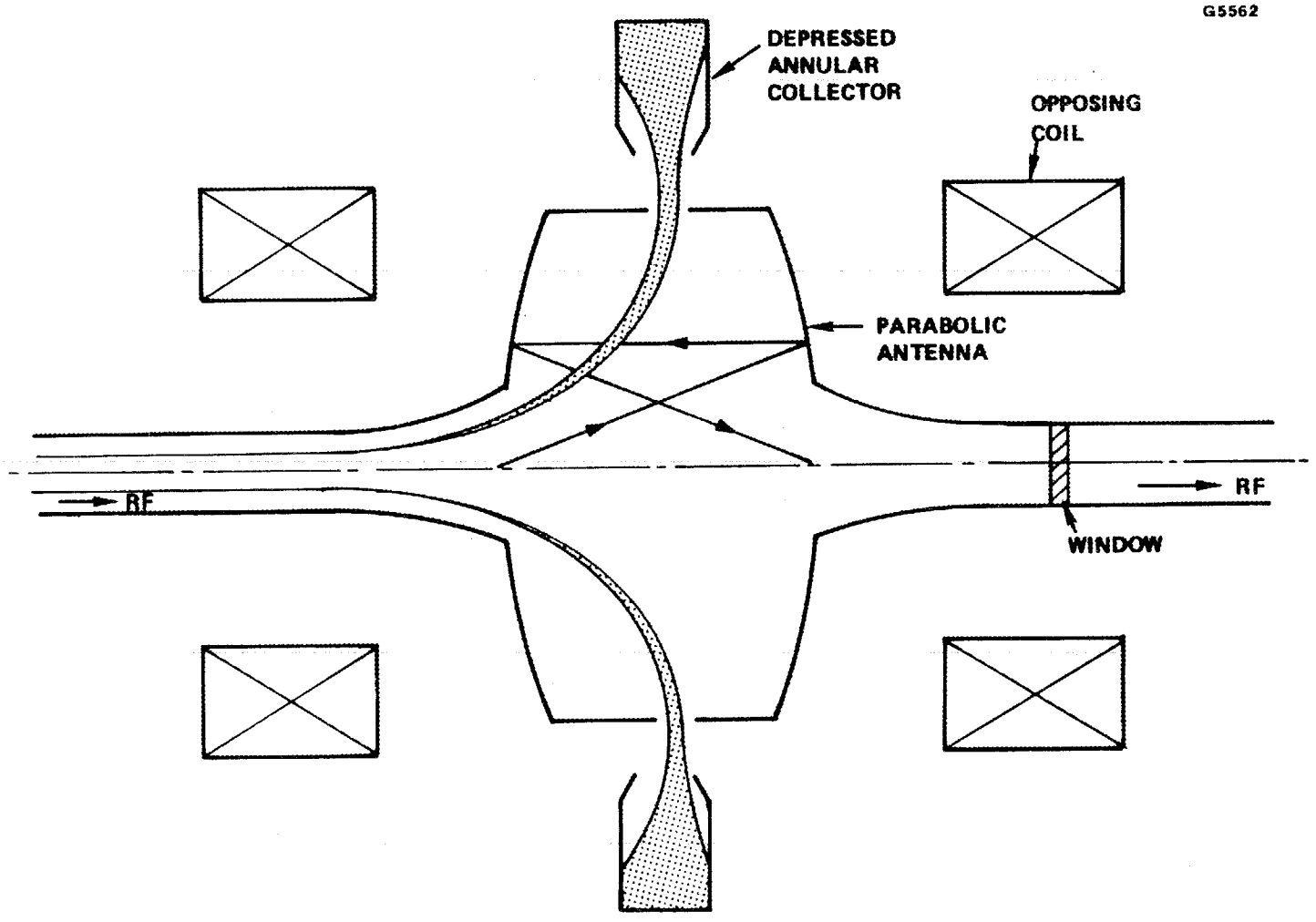

Figure 4-2 Electron extraction between facing parabolic antenna proposed by R. Dandl of Oak Ridge.

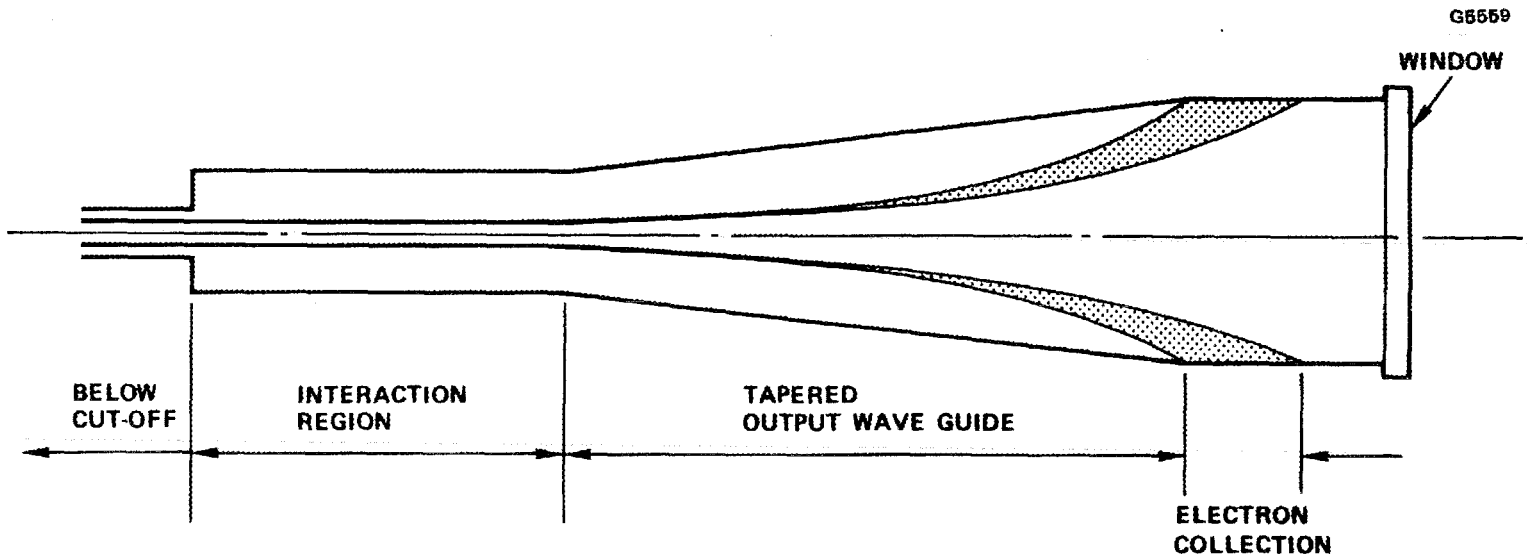

Figure 4-3 Schematic of waveguide and electron collector.

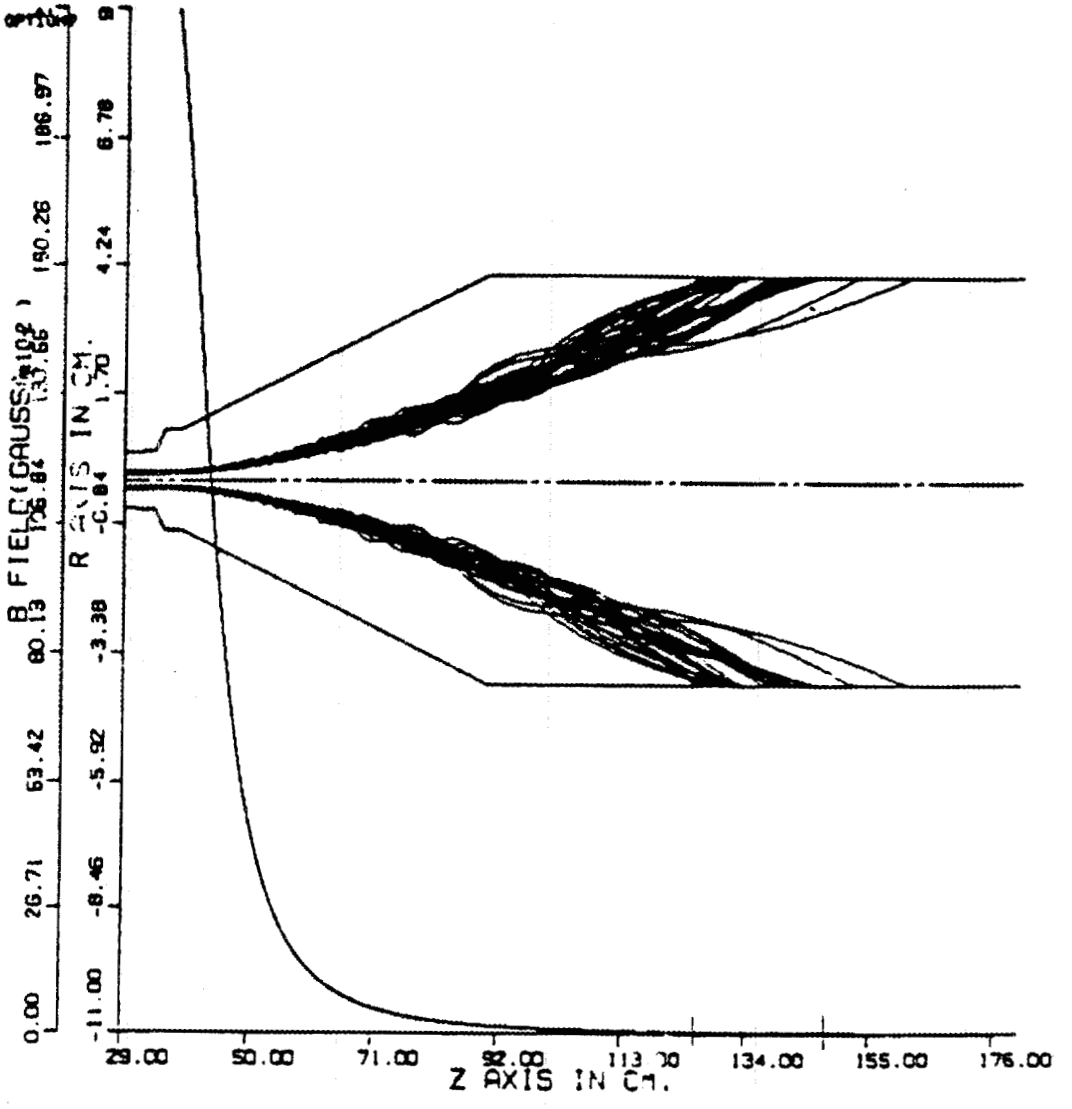

Figure 4-4 Graphic output of an electron beam RF modulated by a cavity, and impacting on the collector walls.

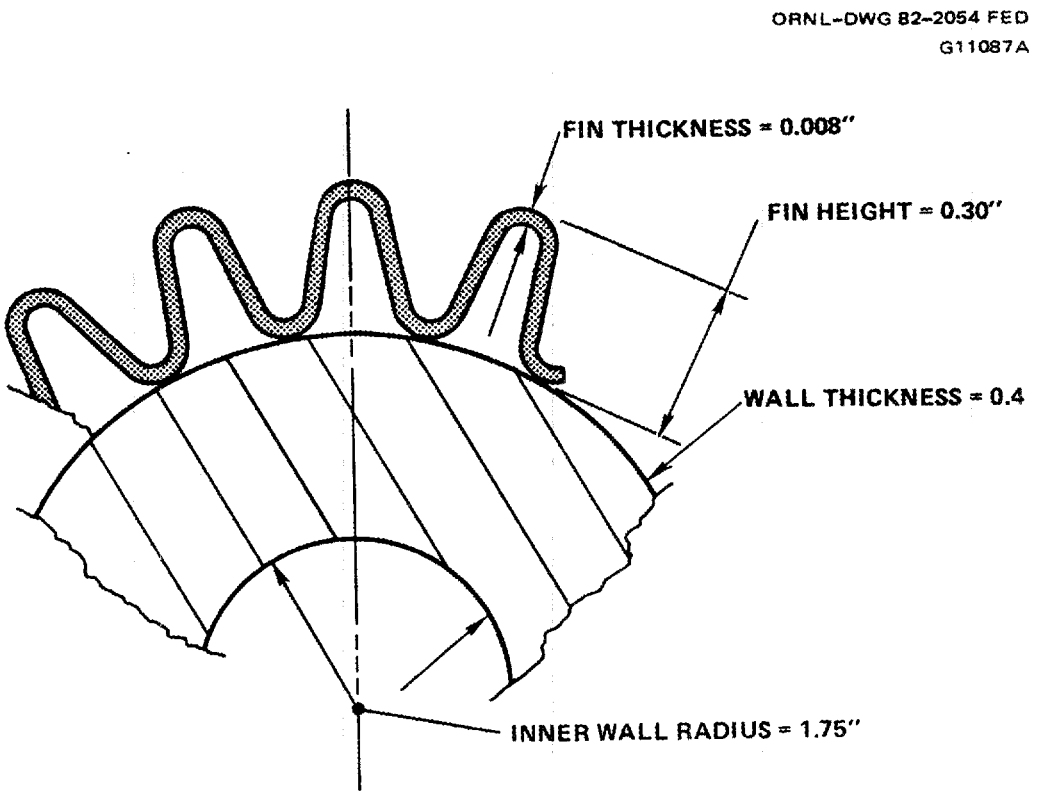

Figure 4-5 Cross-sectional view of the CW collector assembly with cooling fins.

ORNL PHOTO NO. 0348-82
E3956

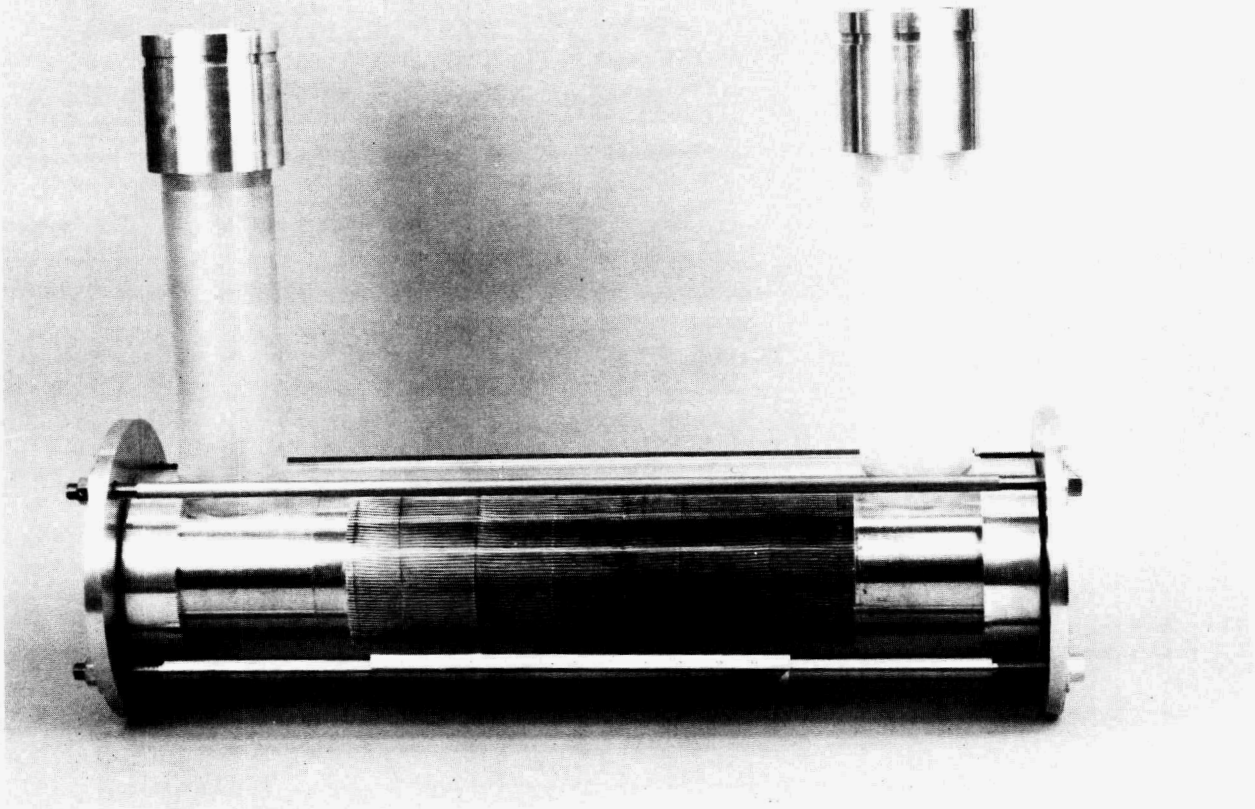

Figure 4-6 CW collector mock-up.

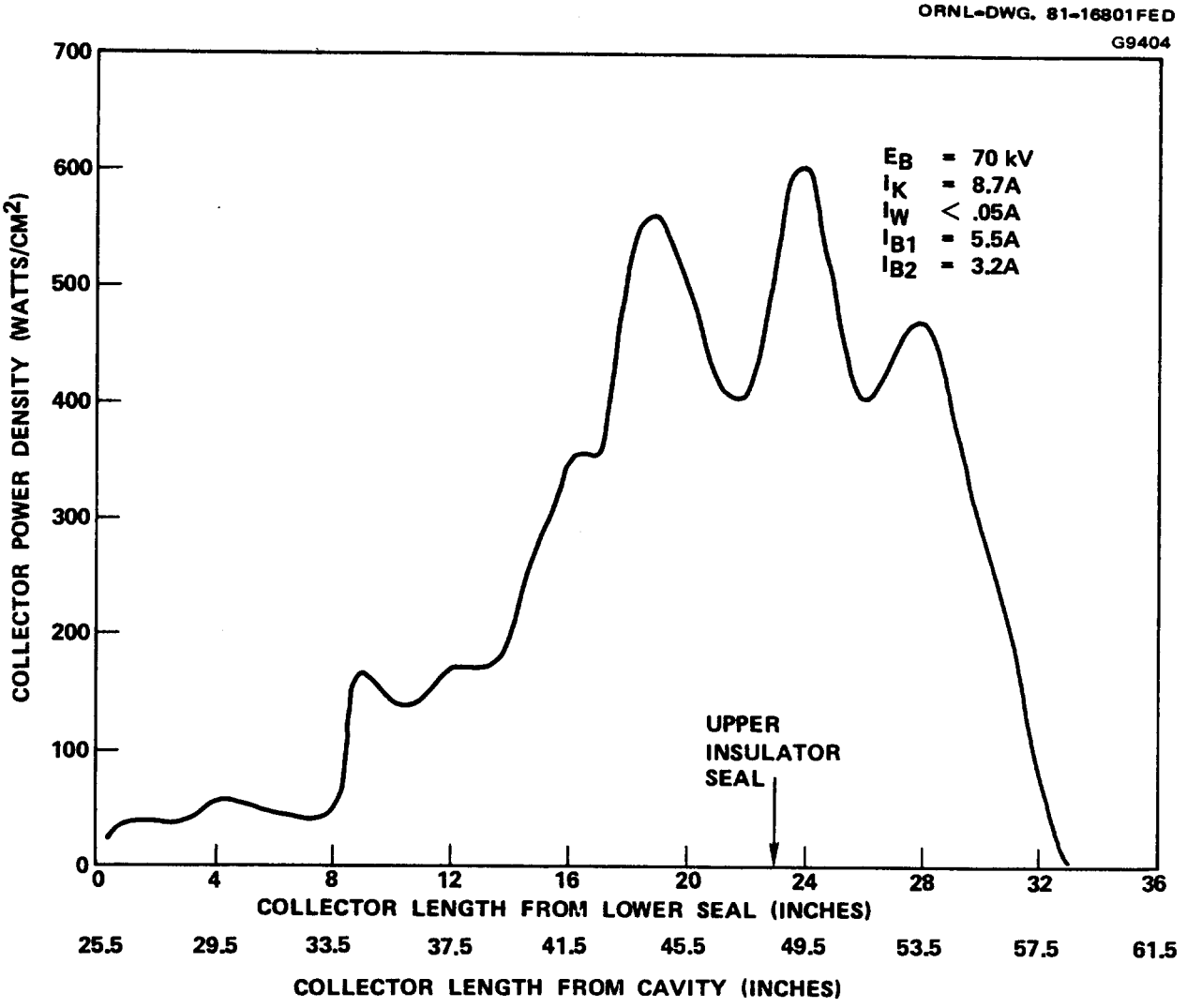

Figure 4-7 Collector power distribution - as determined by X-ray sensitive film exposure.

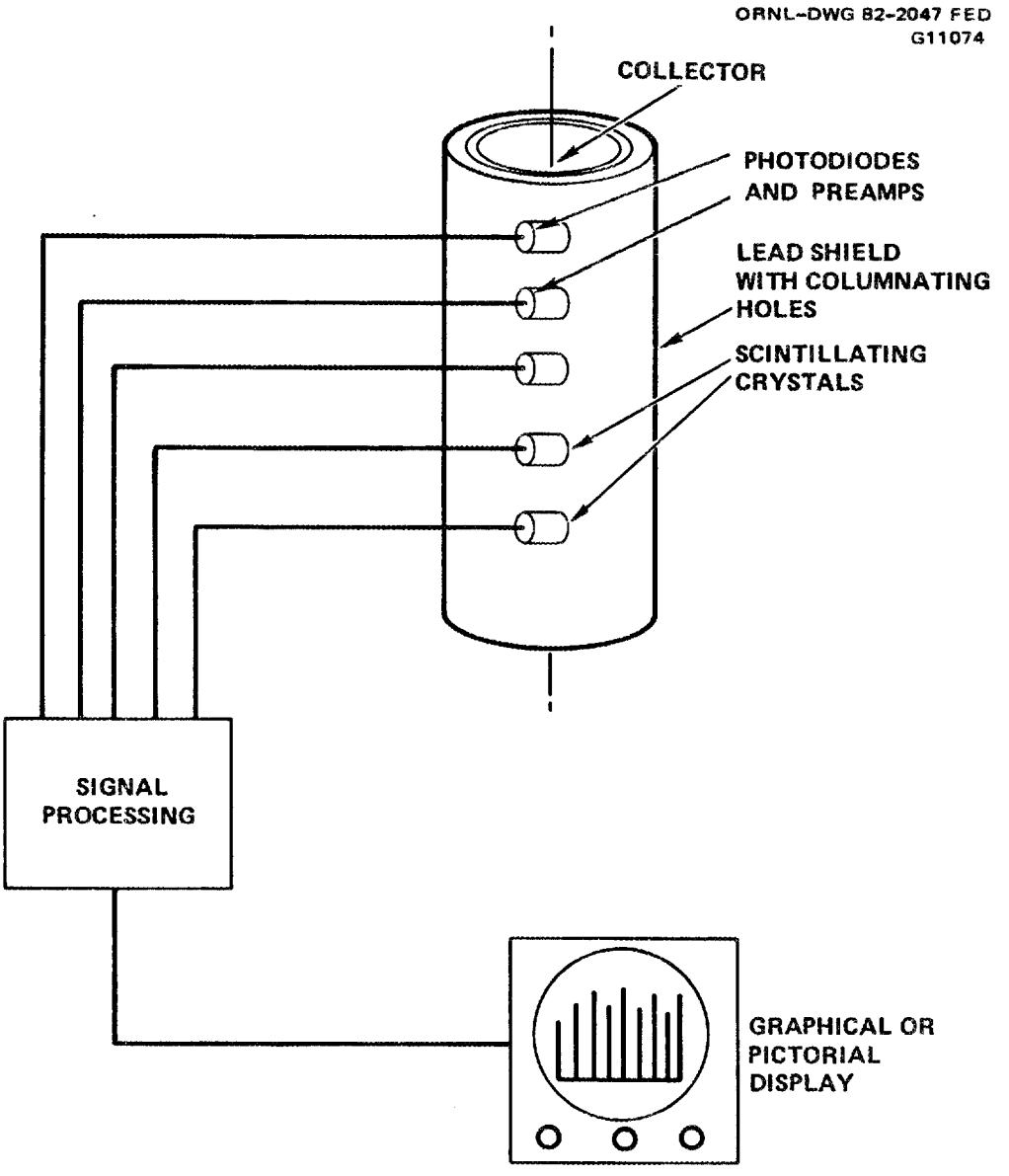

Figure 4-8 Real time detection and display scheme of electron density profile. The strip of detectors is azimuthally rotatable.

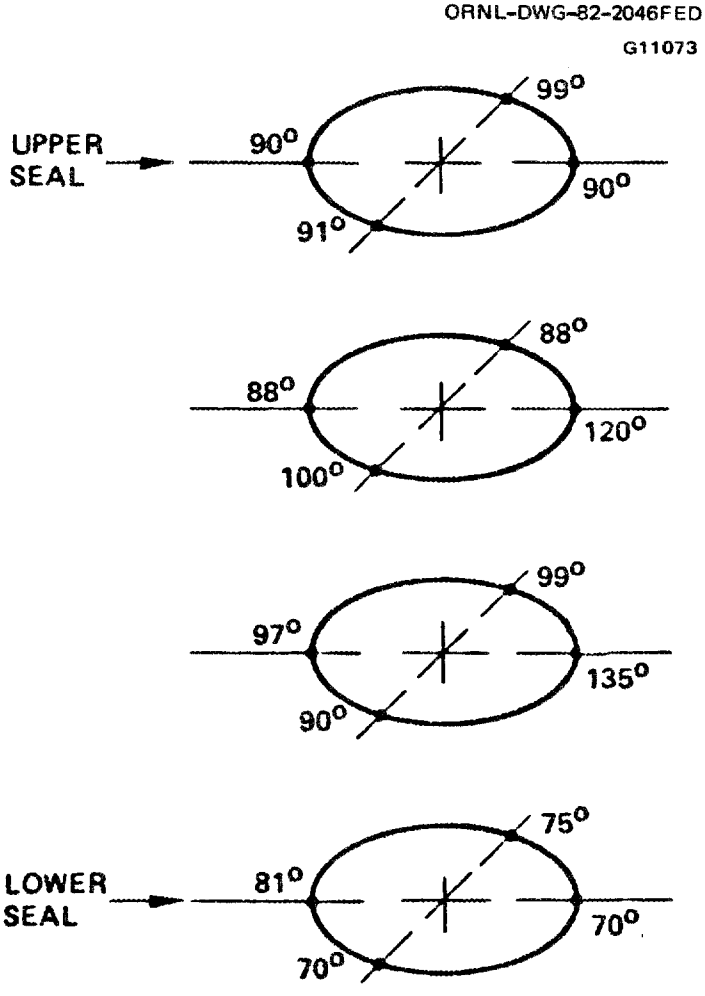

Figure 4-9 917H gyrotron thermocouple measurement of collector temperatures at four axial positions.

E4684

ORNL PHOTO NO. 0347-82

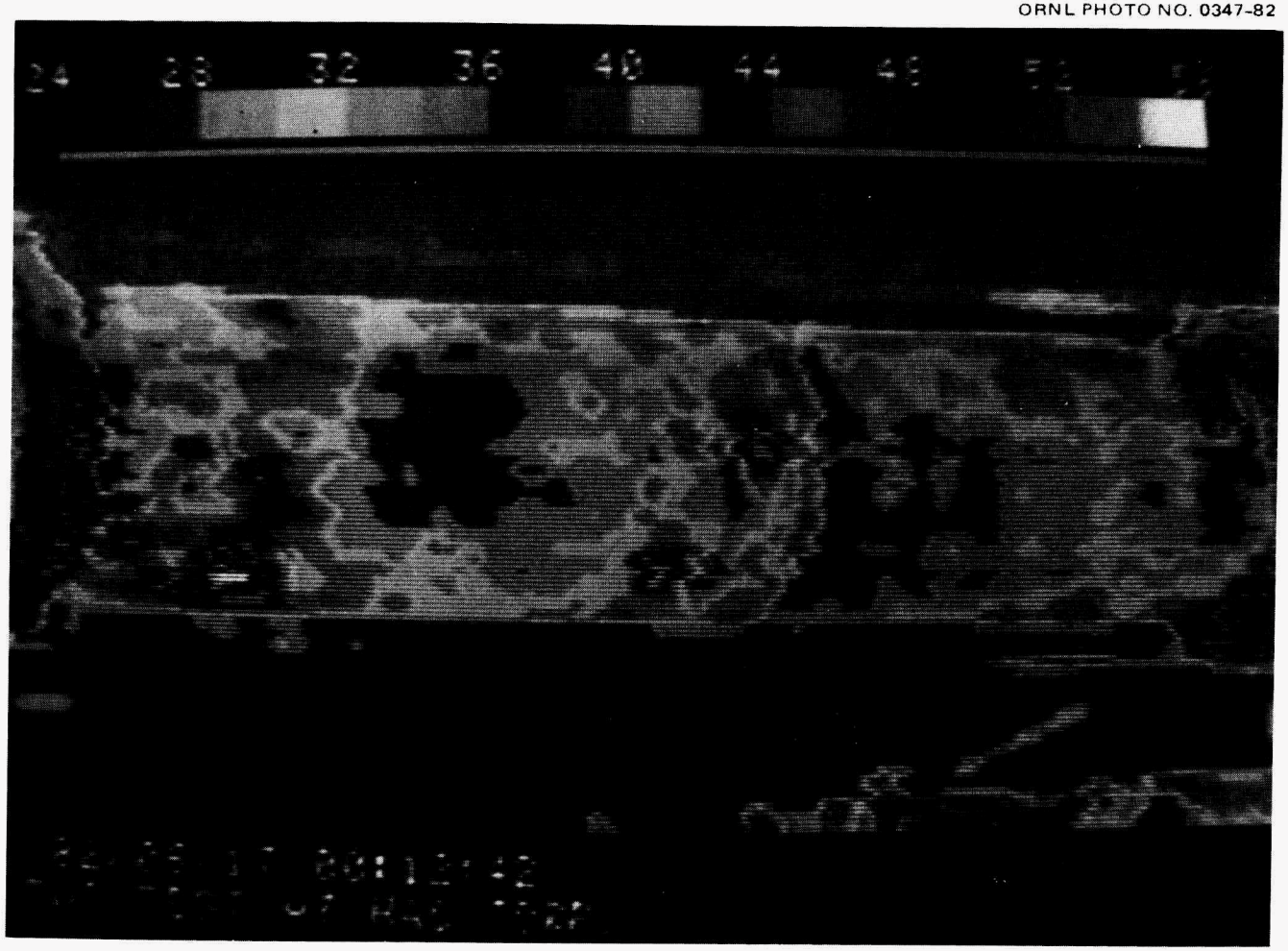

Figure 4-10 Enhanced infrared image of gyrotron S/N 1A showing the collector, lengthwise. A severe hot spot is seen in the lower left corner.

4.2 RF OUTPUT WINDOW

The choice of high temperature-brazable ceramics for windows is a tradeoff between the higher thermal conductivity and wider bandwidth (lower dielectric constant) of beryllia (BeO) versus the higher strength of alumina (Al_2O_3.) Both alumina and beryllia windows have been tested during the course of this development.

Several different RF window designs have been constructed during the course of this development program:

- Single disc window: can be either edge-brazed into the waveguide, or oversized and "face-brazed" by an outer annular ring (Figure 4-11) for greatly increased thermal and mechanical capability. BeO (ε_r = 6.6 at 60 GHz) is the material of choice since Al_2O_3 (ε_r = 9.6) suffers from narrower bandwidth due to its higher dielectric constant.

- Double disc, FC-75 face-cooled window: the low dielectric constant and reasonable loss properties of FC-75 make this fluorocarbon fluid a ready microwave medium while a specific heat of 0.25 cal/g-K make it a very acceptable coolant. This results in a window of high power handling capability with fair frequency response, although there is still considerable mismatch at or around the TE_{221} resonance.

- Multi-disc window: By employing quarter wave matching techniques, more than two dielectric media can be combined to result in significantly wider bandwidth. The wider bandwidth results in low VSWR at the frequencies of potentially interfering modes such as TE_{22} (Figure 4-12), and therefore raises their start-oscillation threshold. The use of a multi-disc window as a vacuum window on a Hughes gyrotron was postponed by program direction until its power handling capability could be demonstrated. Instead, a multi-disc barrier window was constructed for 28 GHz (Figure 4-13), where it could be readily tested at ORNL using existing CW gyrotrons. To date no CW tests have occurred. (This design has successfully handled 200 kW, 100 ms pulses at 1 percent duty in a 53 GHz tube, limited only by the capability of the HEDD modulator.)

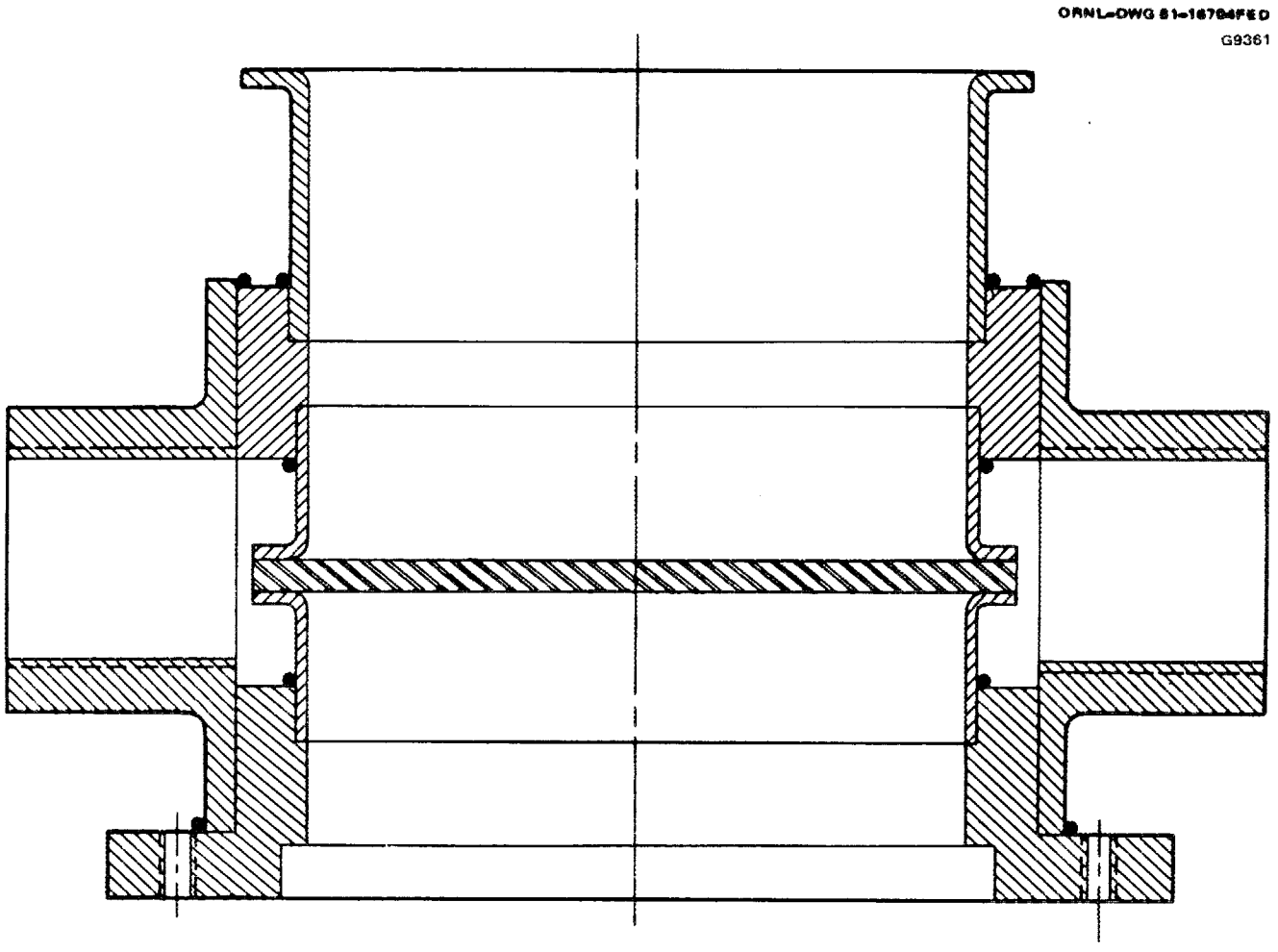

Figure 4-11 Mechanical design of single disc window.

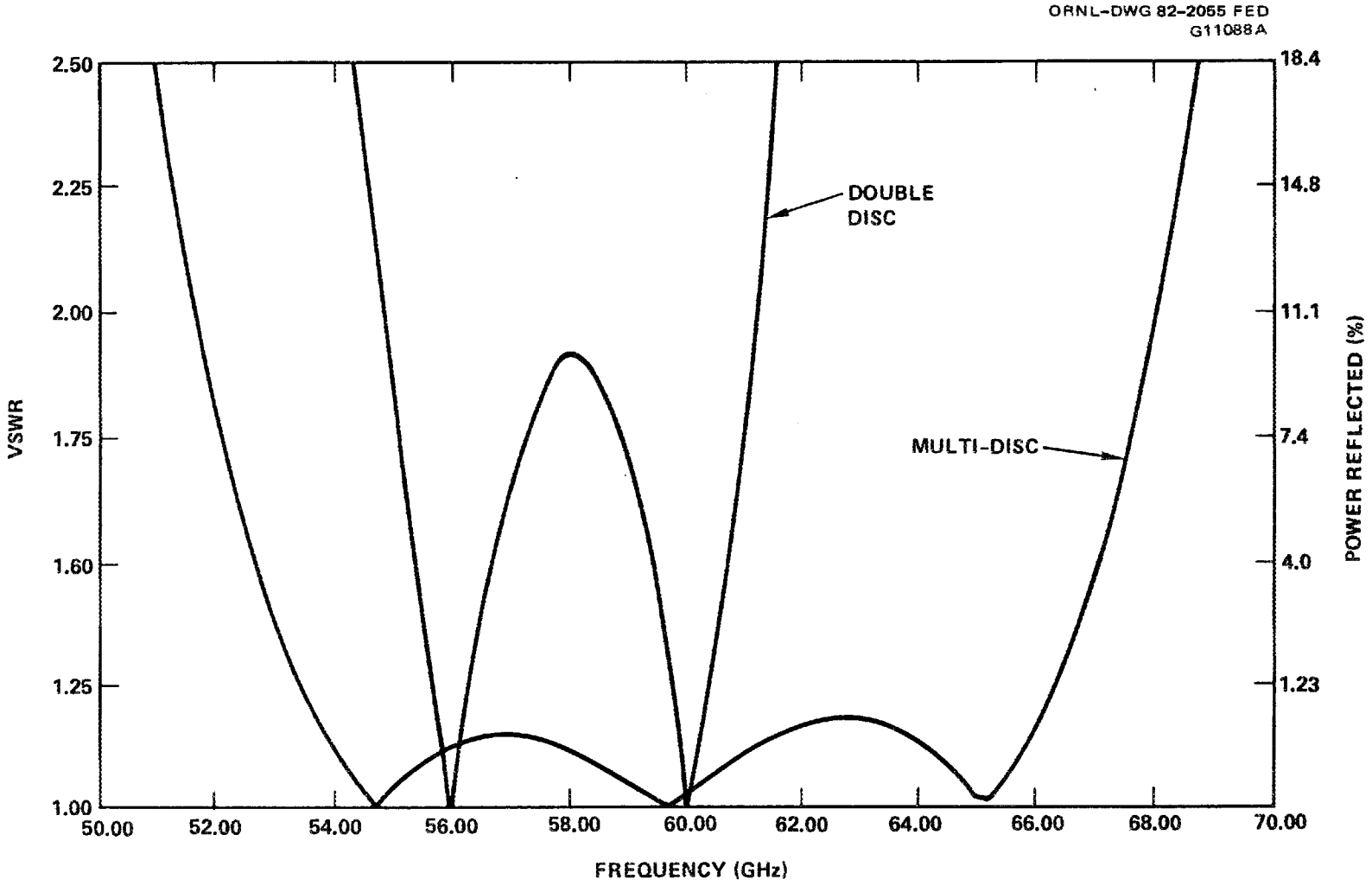

Figure 4-12 Comparison of VSWR pass bands of two Fc-75 cooled window designs.

E4685

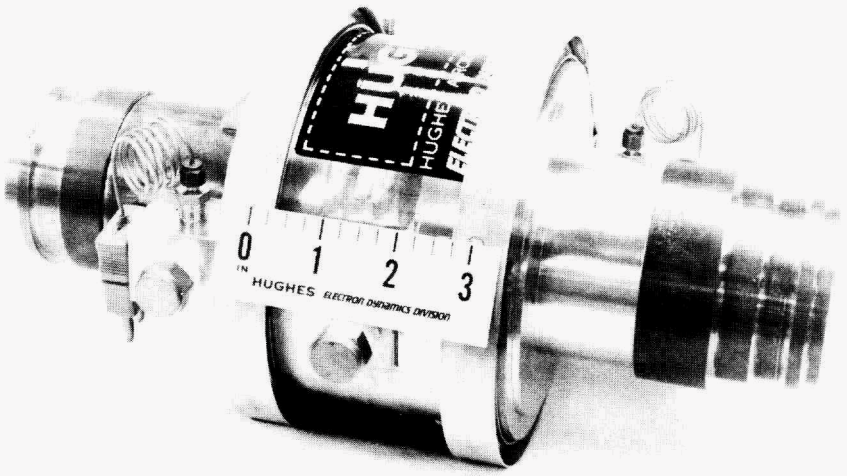

Figure 4-13 28 GHz barrier window for experimental determination of the power handling capability of the multi-disc configuration.

4.3 OVERALL TUBE LAYOUT

Figure 4-14 shows the first gyrotron, distinguished by its thin-walled, convectively-cooled collector allowing ready diagnostic investigation of collected beam distribution. The final tube design (Figures 4-15, 16, 17) is shown without drift tube and collector coolant housings, before going on test.

ORNL PHOTO NO. 5066-81
E3424

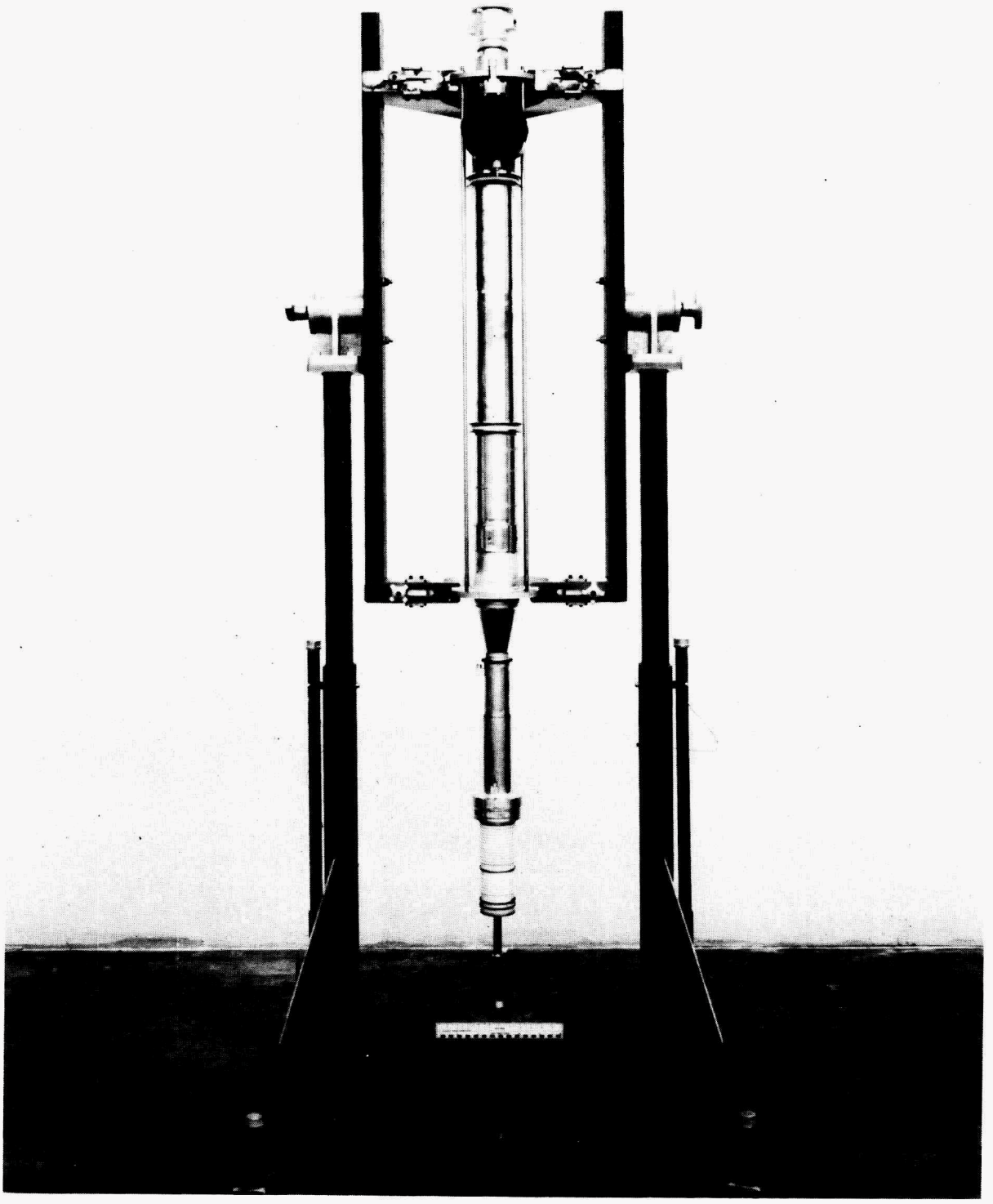

Figure 4-14 917H S/N 1 Hughes 60 GHz, 200 kW pulsed gyrotron.

E4686

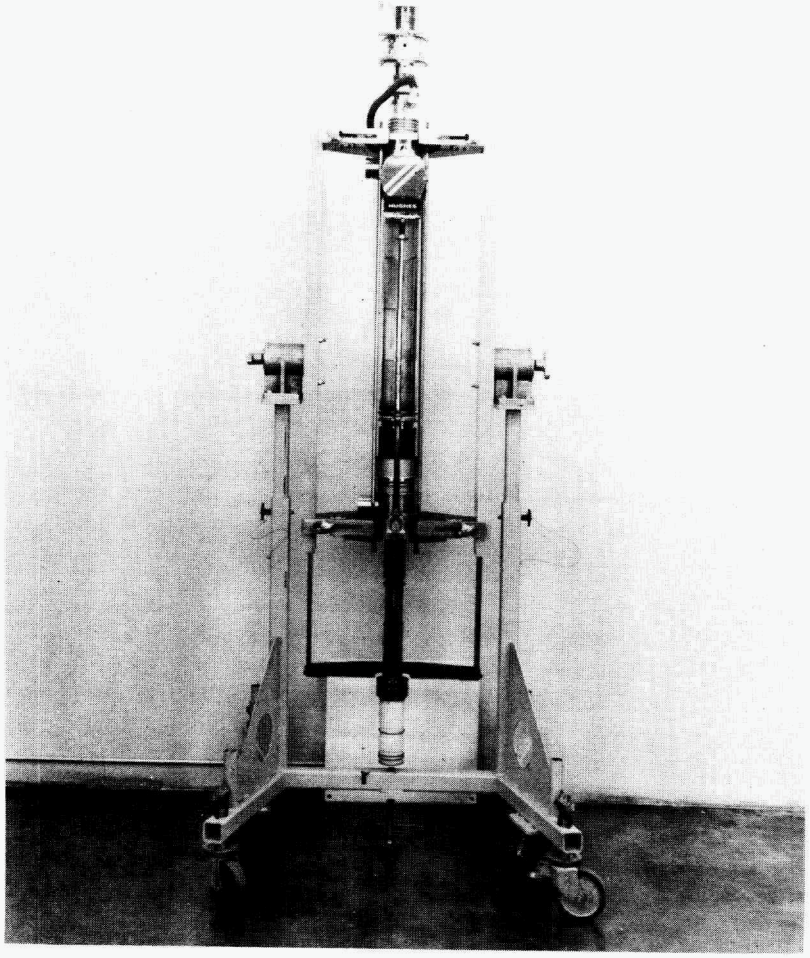

Figure 4-15 917H S/N 3 Hughes 60 GHz, 200 kW CW gyrotron.

ORNL PHOTO-0132-83
E4687

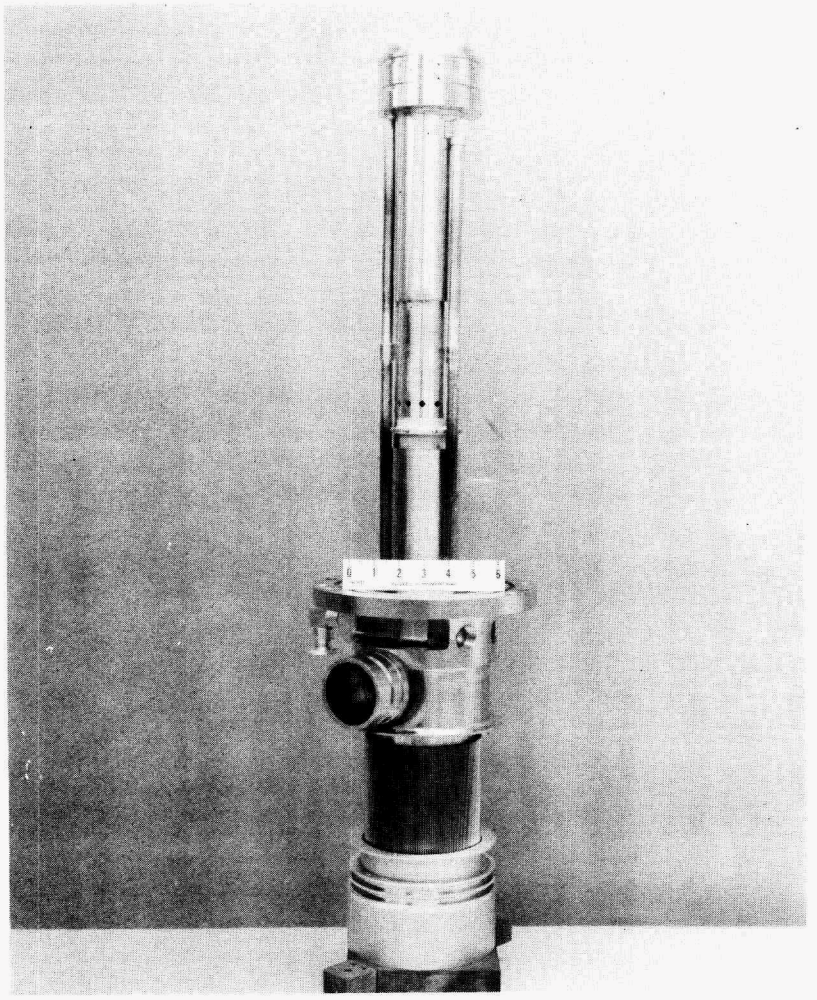

Figure 4-16 Drift tube, cavity, and uptaper assembly.

ORNL PHOTO-0131-83
E4688

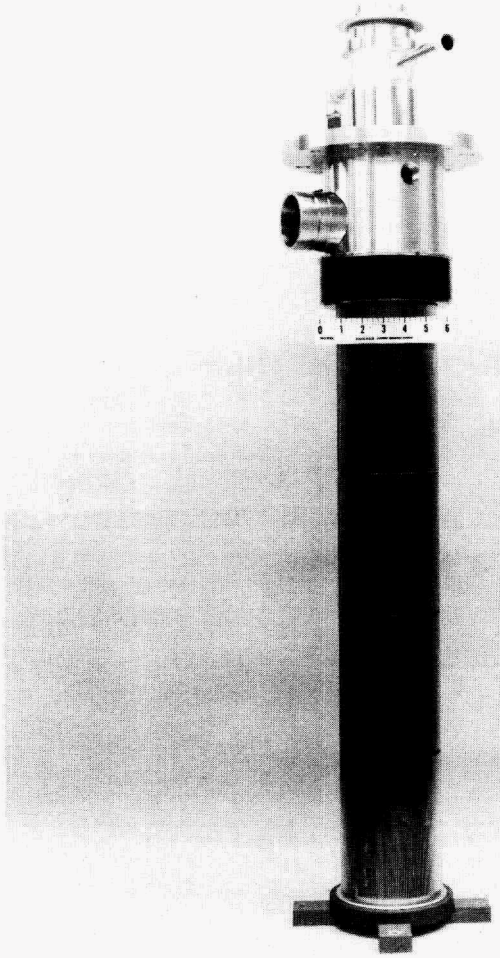

Figure 4-17 Collector and down taper assembly.

5.0 TEST RESULTS AND DEVICE DEVELOPMENT

5.1 BEAM TESTER

To investigate beam quality and evaluate the gun design, a magnetron injection gun with a plugged anode (Figure 5-1) was constructed, sealed-off, and tested at short pulsewidths in a flat 1300 gauss field. Full emission was obtained with negligible levels of mod anode interception current at mod voltages out to the design value of 22 kV. Satisfied with the beam performance, this "triode" was removed from test to allow full testing of S/N 1.

5.2 917H S/N 1

S/N 1 went on test (Figure 5-2) in July 1981, after a delay caused by an open in superconducting coil #6 that required shipment cross country to Magnetic Corporation of America and back for repair. This tube was conservatively designed for low oscillation thresholds (high Q cavity) and guaranteed high transmission (large beam tunnel). Even so, it verified theoretical predictions by delivering 160 kW at 34% efficiency.

The intentional high Q design of the cavity along with the large beam tunnel (which allowed for off-axis entrance of the beam to the cavity) made this device capable of oscillation in several different cavity modes (Figure 5-3) with only minor adjustment of the operating parameters, mainly cavity magnetic field.

In short, this first device verified the basic design philosophy and validated the construction and testing techniques for further device development.

5.3 TRANSVERSE MAGNETIC FIELD MEASUREMENT AND TUBE POSITIONING

Focussing S/N 1 for maximum transmission of beam current to collector required significant tilting and translation of the tube in the superconducting solenoid. This indicated a significant misalignment of the true magnetic axis with the actual geometric axis of the bore. To investigate this further, a study of the transverse magnetic field content of the solenoid was made. A proper experimental technique which allows for possible misalignment of the Hall Effect chip in the probe holder was followed for determining $B_\perp$ in the presence of

ORNL-PHOTO 0341-82
E3618

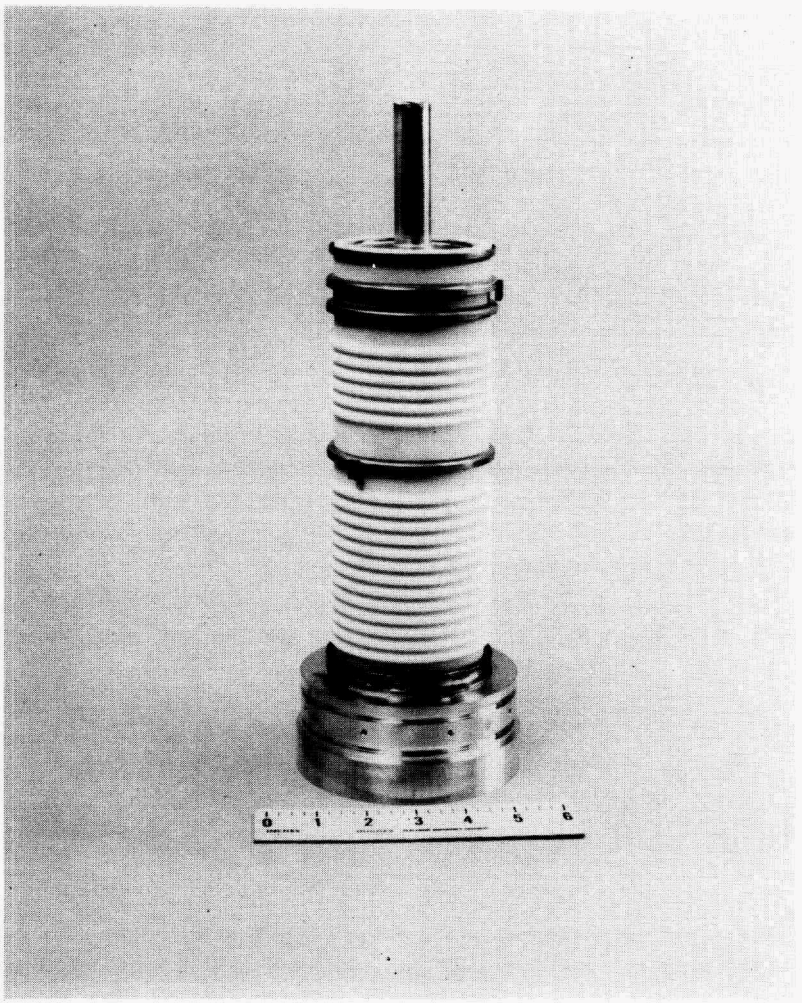

Figure 5-1 Gyrotron gun tester.

ORNL PHOTO NO. 0346-82
E3626

Figure 5-2 917H Gyrotron in test stand.

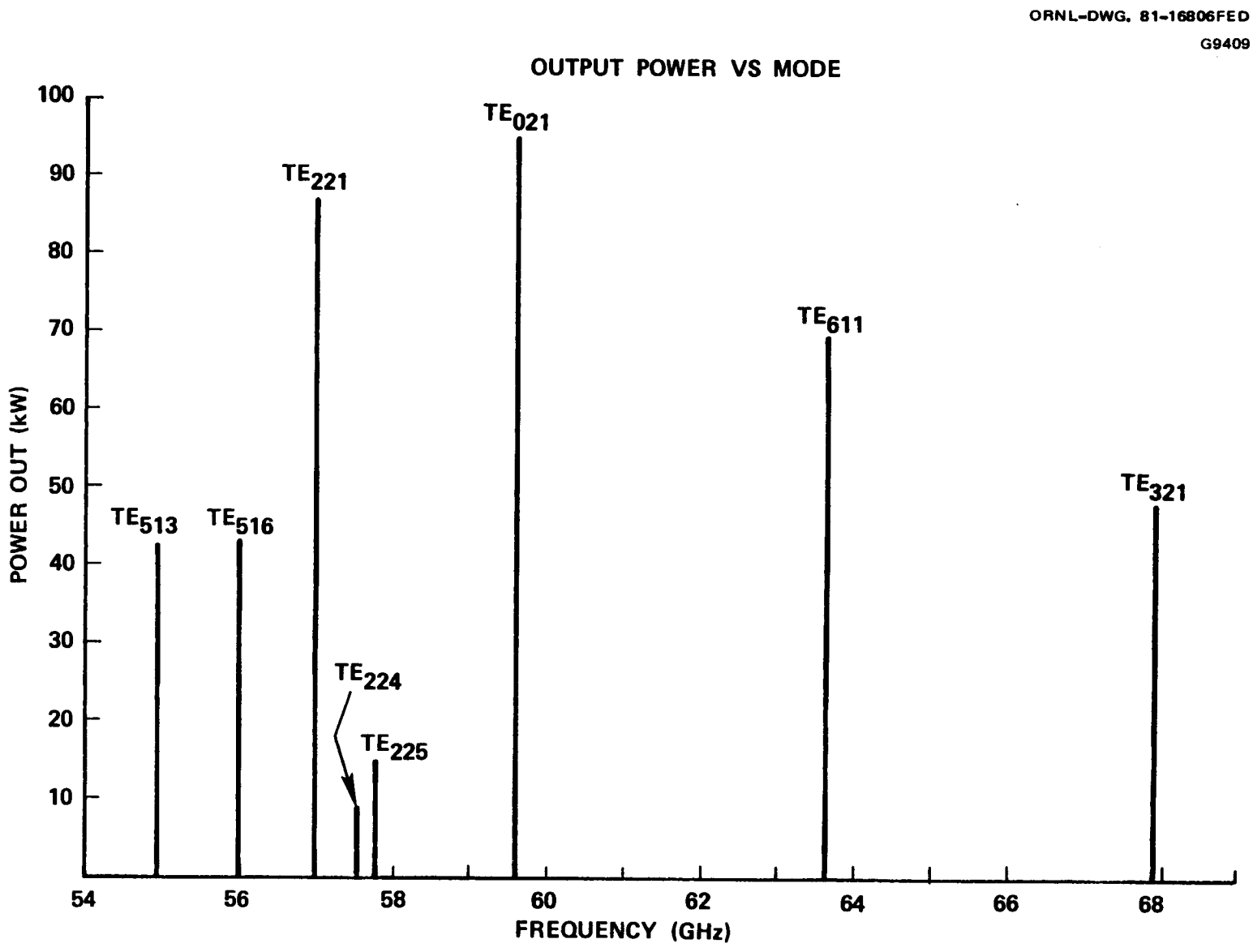

Figure 5-3 Power and frequency of observed cavity modes on S/N 1.

large B_z. The transverse probe (Figure 5-4) is rotated through 360° to determine both the maximum ($B_\perp \cos\theta + B_z \sin\theta$) and the minimum ($B_\perp \cos\theta - B_z \sin\theta$) readings (180° apart). $B_\perp$ is then found as half the sum of the maximum and minimum at a direction given by the orientation at the maximum reading. As expected, transverse fields, measured along the geometric axis of the bore, were severe. (Figure 5-5)

If the coils were concentrically and symmetrically wrapped on a perfect mandrel that was merely off-axis, a true magnetic axis of zero B_r should be obtainable. Considerable effort was then made in locating a (linear) axis that gave minimal transverse fields. However, the best performance obtainable (Figure 5-6) was still characterized by $B_\perp/B_z$ values of .4%. The deleterious nature of transverse fields was seen in section 2.2. Transverse fields should be kept to .2% of the axial field. This is routinely generated in room temperature solenoids and is claimed as achievable by superconducting coil manufacturers.

5.4 BEAM INSTABILITY INVESTIGATION

In testing S/N 1 with the "design" (flat over the cathode) magnetic field, a beam instability condition was first observed that manifested itself by:

- Excessive mod anode interception current at beam parameters that, from electron optics considerations, could not have been caused by mirroring of downstream particles or from grazing interception within the first cycloidal orbit after emission.

- Anomolous S-band RF emanations from the gun ceramics

- Gross localized heating of the lossy drift tube (observed later on S/N 1B and S/N 3)

- A reduction in output power and efficiency as beam alpha is experimentally increased (by increasing anode voltage) from low ($\alpha \simeq 1.1$) to moderate ($\alpha \simeq 1.5$) values, contrary to efficiency calculations. (In fact, the severity of the instability could be ultimately judged by the degree to which high alpha with high efficiency could be attained.)

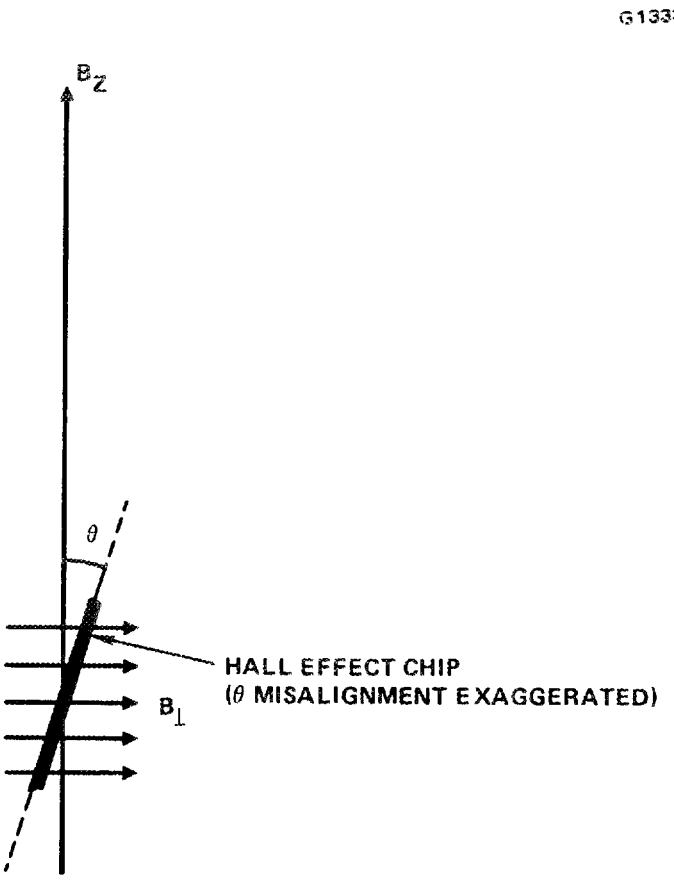

Figure 5-4 Experimental technique for determination of $B_\perp$ in the presence of large B_z.

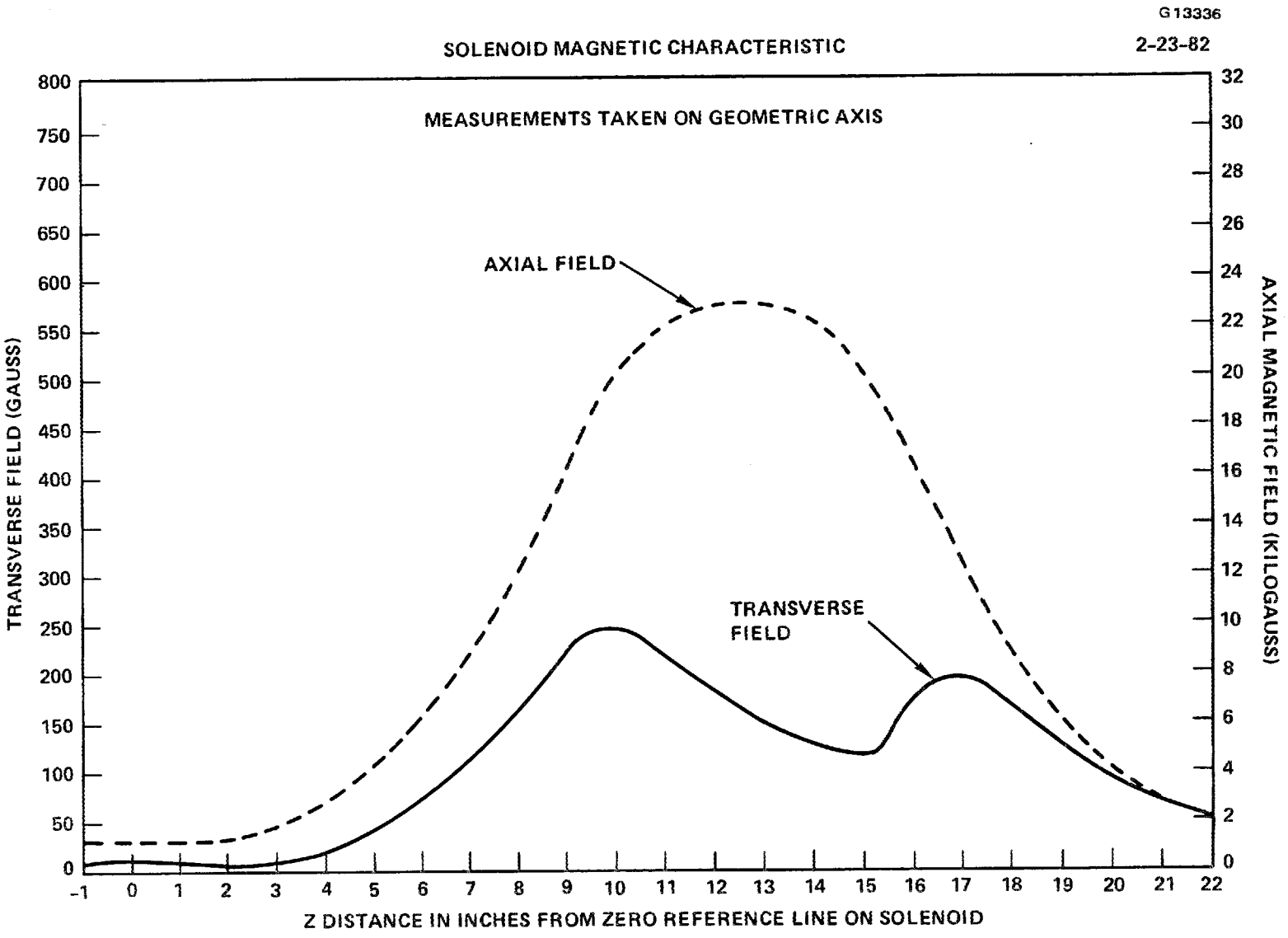

Figure 5-5 Transverse magnetic fields on geometric axis of bore.

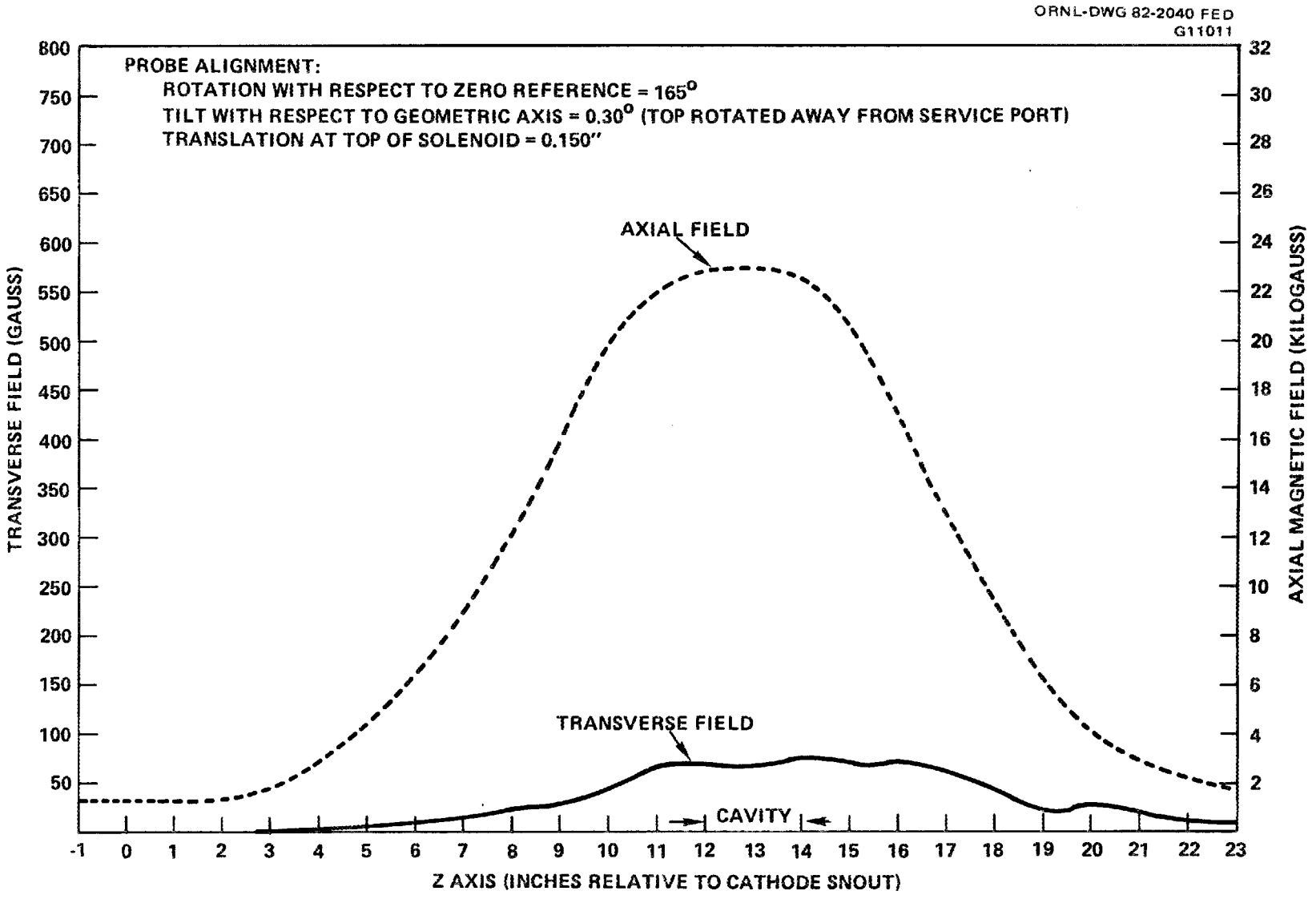

Figure 5-6 Best transverse magnetic field measured in superconducting solenoid.

However, an alternate magnetic field was empirically determined (Figure 5-7) that eliminated any instability and allowed high alpha, high efficiency operation. In fact, anode interception beyond the high efficiency point could realistically be attributed to normal beam mirroring, particularly considering that the cathode roughness and thermal spread in transverse velocities are not accounted for in gun simulations. Although most readily distinguished by the magnetic field taper in the gun region, later testing of S/N 18 verified that the magnitude and shape of the field within the drift tube was just as important.

In an effort to determine the cause of the beam instability, the gun tester was evaluated in the superconducting solenoid. The gun tester was painstakingly positioned within the solenoid as similar to S/N 1's gun as possible. Only a slight increase in mod-anode interception was observed which could be attributed to the higher transverse fields of this solenoid. The design of the gun itself appeared to be satisfactory and the instability problem appeared to be associated with the drift tube or cavity.

A lossy drift section was next added to the gun tester, with the vacuum being closed by a copper plug where the cavity would normally be. This test assembly was also evaluated in the superconducting solenoid. The results are compared in Figure 5-8 with S/N 1 and the gun tester alone, all immersed in the "flat" magnetic field as originally used. The same comparison is made for the tapered magnetic field in Figure 5-9. Considering that discrepancies of several milliamps could be attributable to measurement error in the pulsed instrumentation, it was concluded that the instability problem was associated with the cavity, whether the gun magnetic field was tapered or flat. However, a tapered gun field is preferred since any instability from the drift tube appears to be eliminated with a tapered field.

As further verification, the versatile solenoid design was utilized with the modified gun tester to cause the beam to be intercepted on the walls of the lossy drift section at successively greater distances from the cathode. A flat magnetic field was maintained in the cathode region throughout this test. No instability problem was observed (as evidenced by a significant increase in mod anode interception), until the beam was allowed to pass through the last

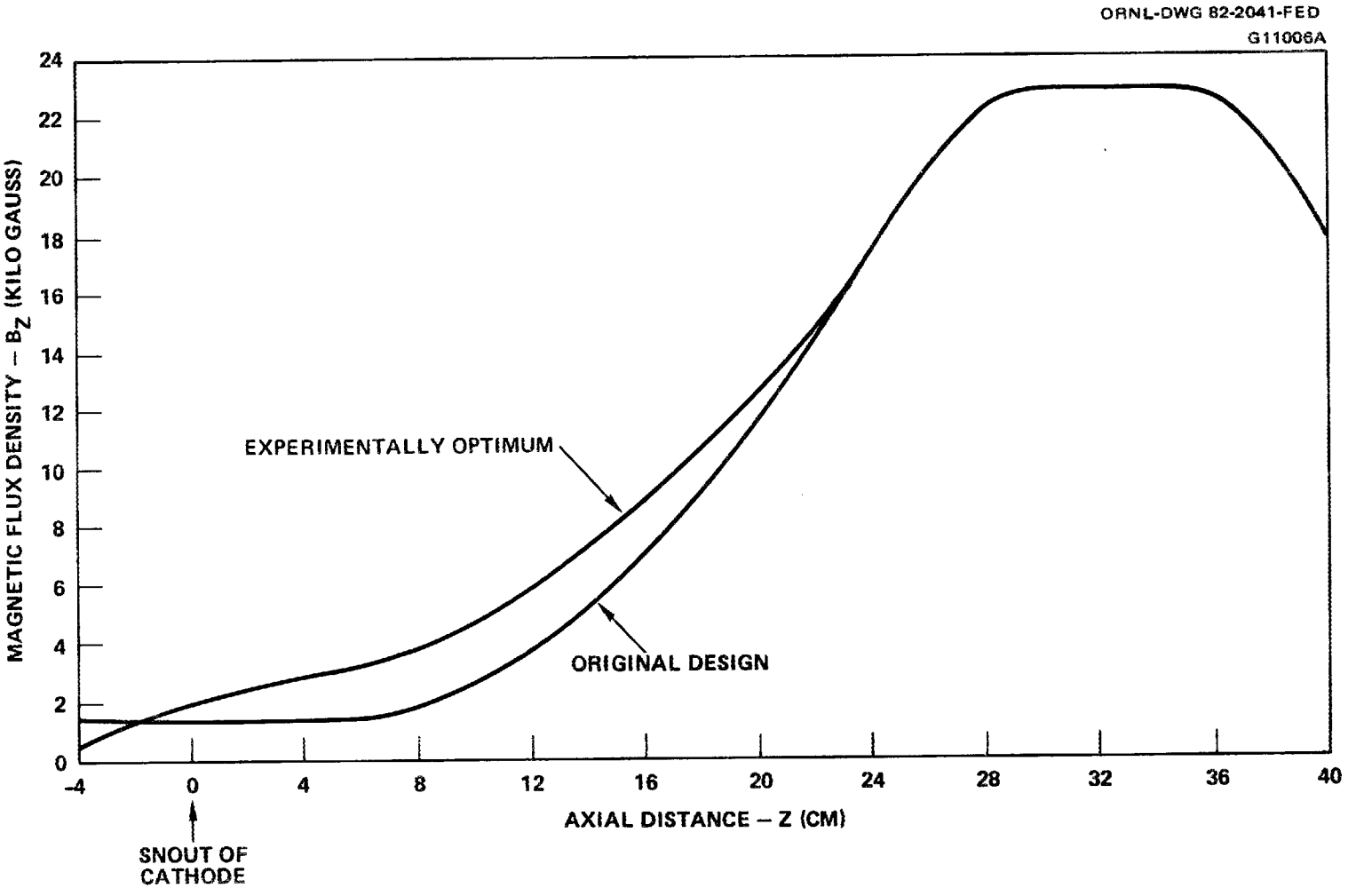

Figure 5-7 Axial magnetic field.

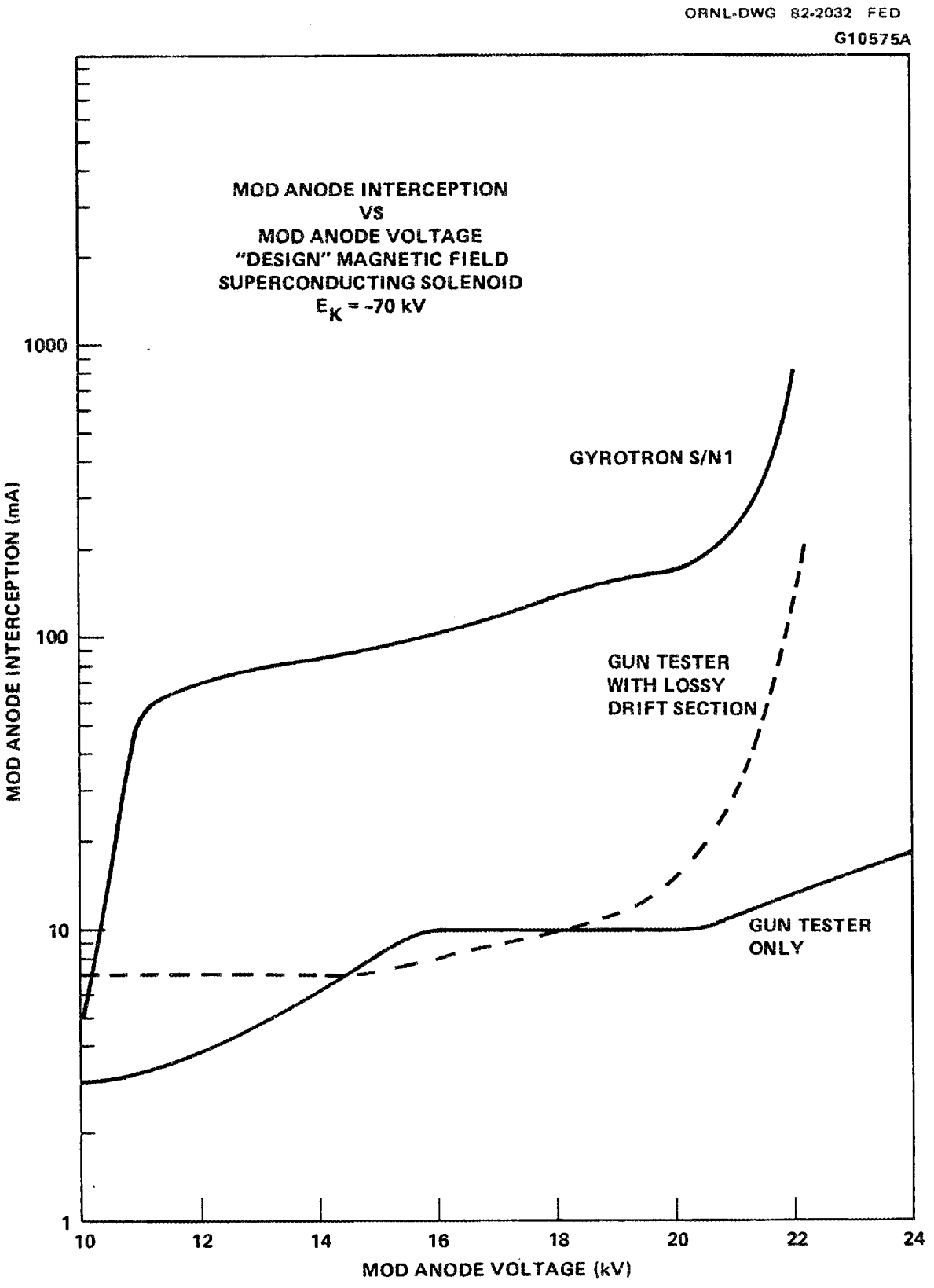

Figure 5-8 Comparison of mod anode current for three different configurations showing the effect of the cavity coupled to the drift tube.

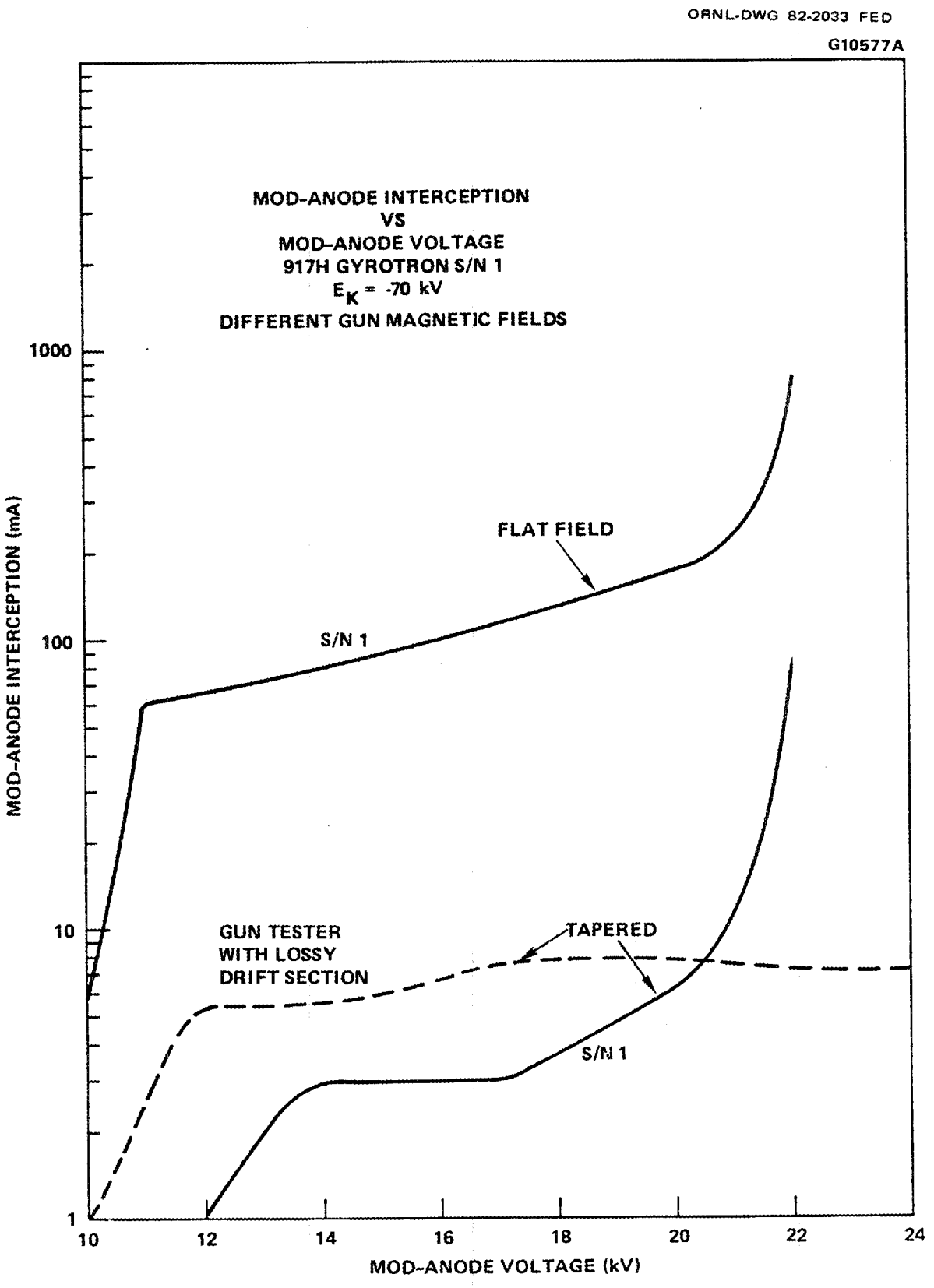

Figure 5-9 Comparison of mod anode current for two different configurations in the tapered magnetic field and contrasted with behavior in the flat field.

part of the lossy drift section (the cavity cut-off section) at high α. Therefore, the instability problem appeared to be definitely associated with either RF generated in the cut-off section or RF reflected toward the cathode from the cavity. The RF emanations observed from the gun were approximately the same as the cyclotron frequency calculated from the flat magnetic field. This S-band emission is probably due to the long duration of constant cyclotron frequency possibly being disturbed or pumped by mirrored electrons or reflected RF from the cavity end. No RF is emanated with the tapered magnetic field.

Further cold testing of the cavity and lossy drift section of S/N 1 found that the cut-off section could be significantly improved with regard to RF leakage from the cavity. The beam aperture was reduced by more than 30%. This change would also force improved beam alignment in the cavity for more efficient TE_{02} operation.

5.5 S/N 1A TEST

S/N 1A was a rework of S/N 1 and incorporated the high efficiency cavity design mentioned in section 3.4. Another significant change was the reduction in diameter of the last few copper discs of lossy drift tube assembly to below cut-off for TE_{01} at 60 GHz. Although focussing would be more critical, particularly in view of the high transverse field content of this solenoid, this would allow better "aiming" of the beam down the cavity axis, (essential for optimal efficiency) and greatly attenuate any rf leaking from cavity into the drift tube (which could perturb the drifting beam and prevent achieving maximum alpha or deleteriously prebunch the beam before the cavity)

Using an empirically determined magnetic field profile, the curves of Figures 5-10 and 5-11 were generated illustrating the high efficiency experimentally obtainable with the HEDD cavity design. (Data points marked with *'s were generated at a significantly different tube position found at a later date. Beam transmission was approximately the same in both cases; however, the bending effect of the magnetic transverse field apparently was such as to cause the beam to traverse the cavity truer to its own axis in the later position). A mode map of S/N 1A (Figure 5-12) reveals the operating range to be quite broad and usable.

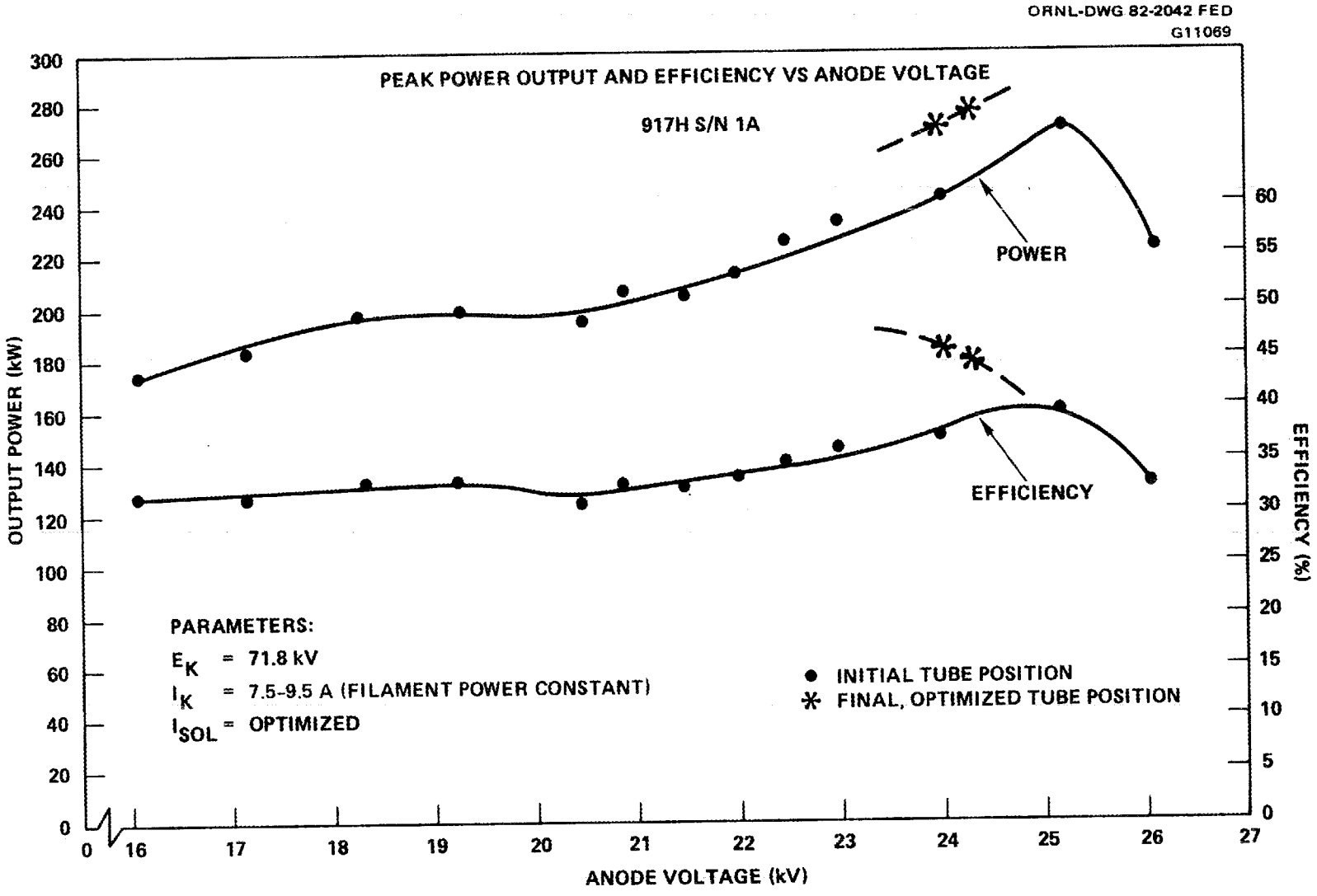

Figure 5-10 Power output and efficiency for S/N 1A versus mod-anode voltage.

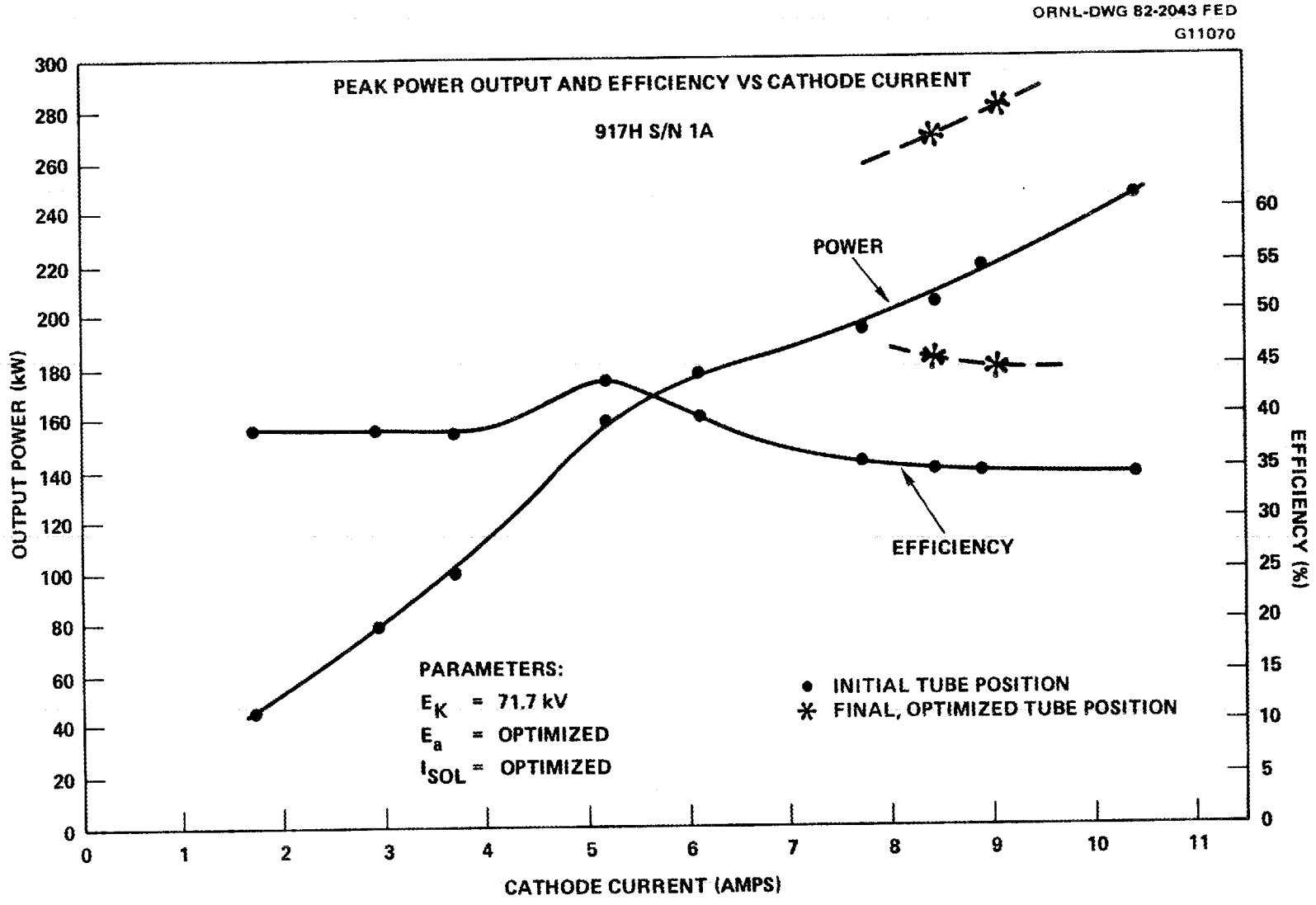

Figure 5-11 Variation of power output and efficiency with beam current for S/N 1A.

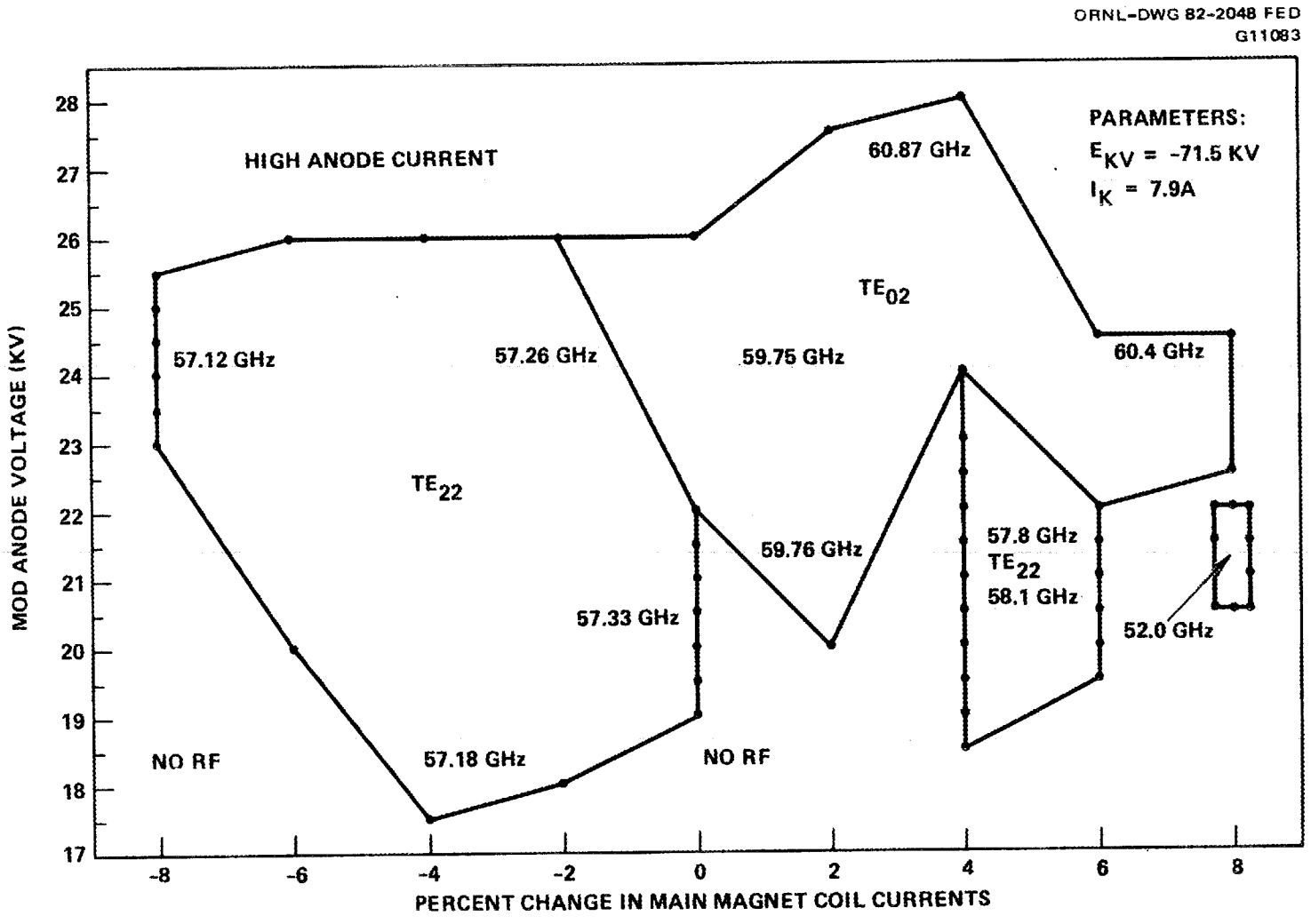

Figure 5-12 Identification of RF modes as a function of anode voltage and cavity magnetic field in the optimal tube position.

5.6 S/N 2A

Having seen dramatic performance improvement on test by tapering the cathode magnetic field, the second tube was built with a shorter drift tube which allowed even greater gun field sloping.

The fragile cathode support of the original S/N 2 apparently buckled during final assembly. The assembler, however, distorted the cathode assembly to meet the alignment required for fixturing. During bakeout and activation, the assembly was stress-relieved and returned to its original buckled position, resulting in a significant skewing of the cathode with respect to the axis. This problem was quickly identified and the tube reworked with the newly available gun redesign which optimized beam quality in sloped magnetic fields over the gun. Present guns use a thermally isolated emitter design so that the bulk of the cathode electrode runs relatively cool and can therefore be sturdily supported.

RF performance of S/N 2A is indicated by Figure 5-13. Probably most obvious is the degradation in electronic efficiency for beam curents over 6A. This was due to mode competition from the TE_{221} resonance. Figure 5-14 shows how the computed cavity magnetic field required for optimal efficiency compares with experimentally used values for S/N 1A and 2A. Mode competition from the TE_{221} resonance at higher beam currents prevented adequately lowering the cavity field to high efficiency regimes on S/N 2A. This additional tendency to oscillate in the wrong mode on the second tube was due to the use of a single disc alumina ($\epsilon_r \cong 10$) instead of beryllia ($\epsilon_r \cong 6.6$) window. The narrower window bandwidth increased reflections at TE_{22} frequencies causing an increase in the effective resonance Q for the TE_{221} mode. Therefore, although the TE_{22} power output was low (Figure 5-15) it was more easily started (Figure 5-16) particularly at the lower magnetic fields required for efficient, high current operation.

However, even for regimes of operation in which mode competition was not a limiting factor (i.e. for low beam currents) the efficiency of S/N 2A (with short drift tube) was below that of S/N 1A. Hence the drift tube and magnetic field of S/N 1A seem about optimal.

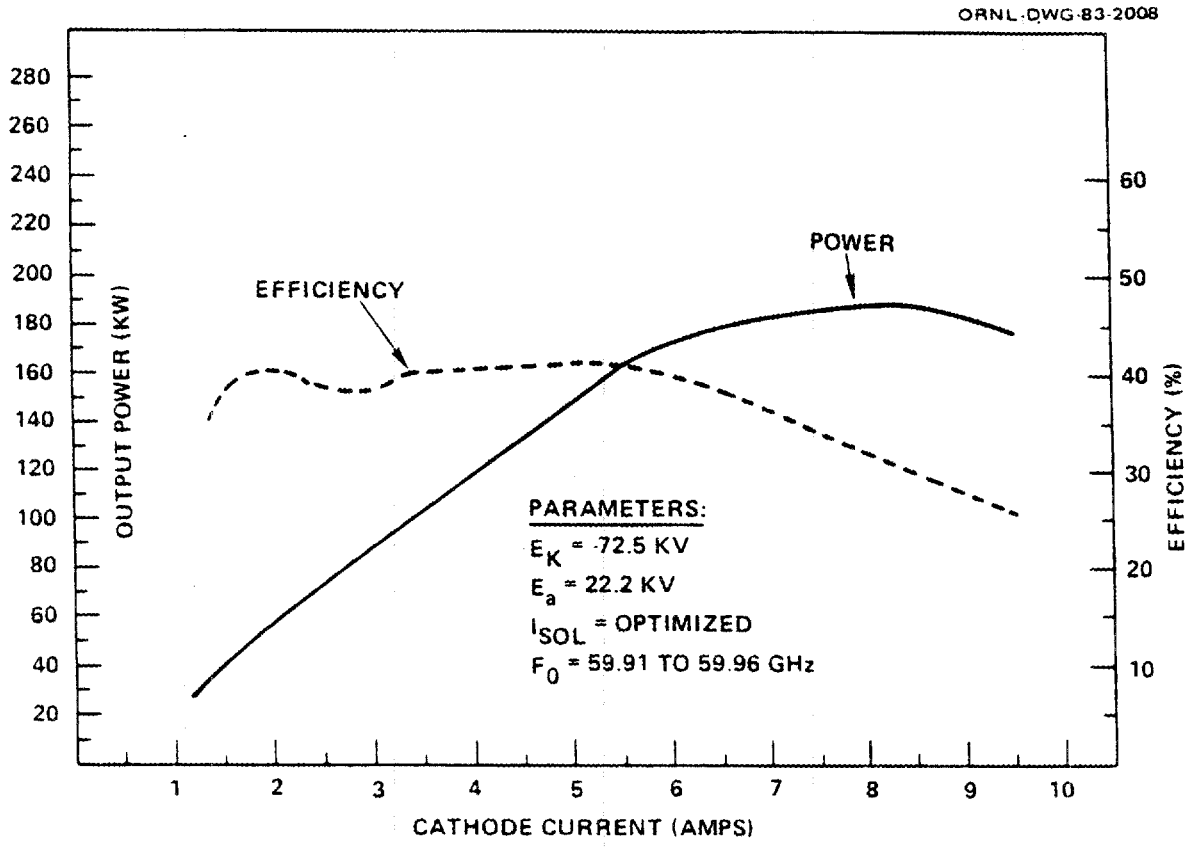

Figure 5-13 Power output and efficiency versus beam current for S/N 2A (short pulse).

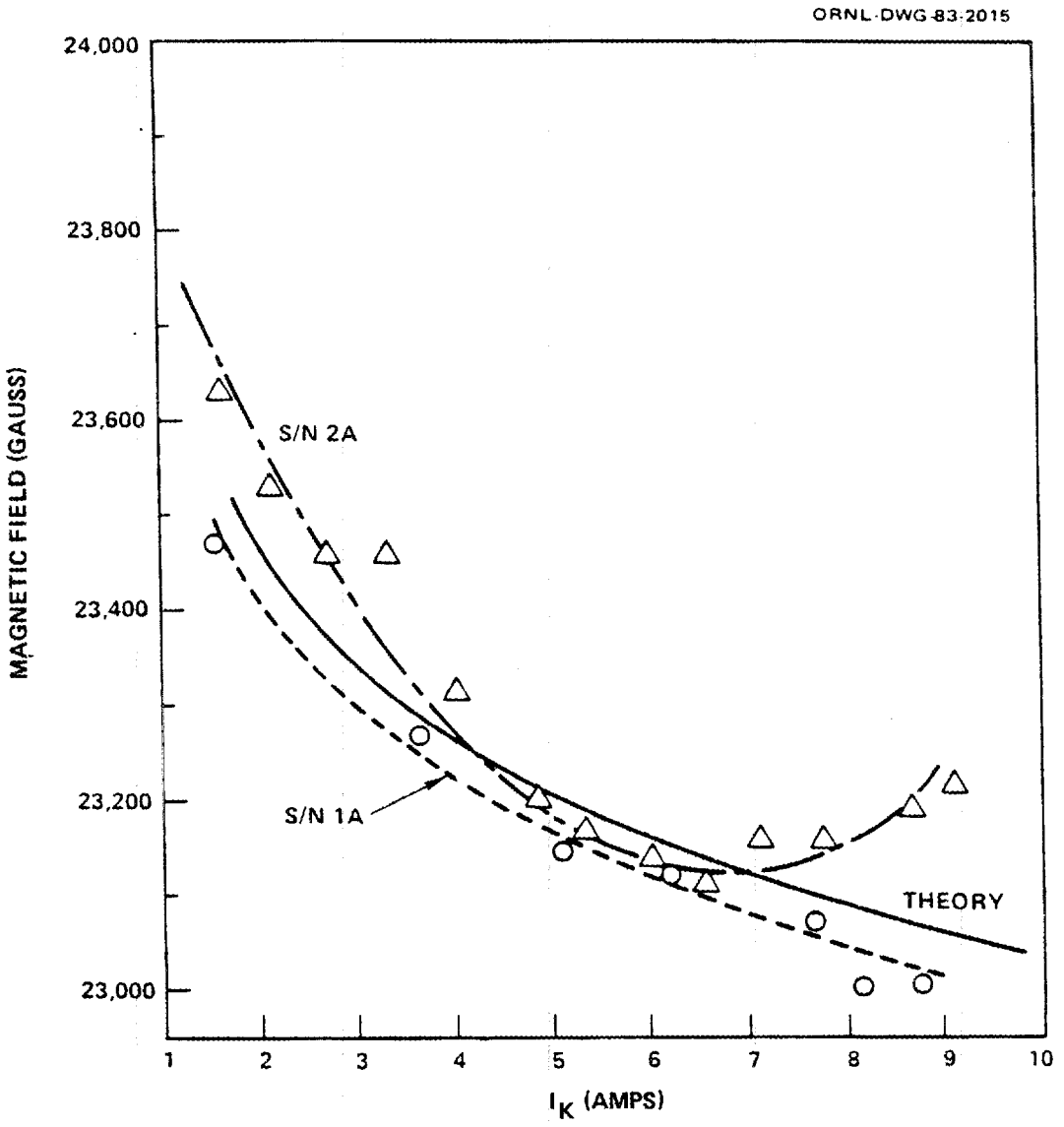

Figure 5-14 Cavity magnetic field for maximum efficiency vs beam current, for the theoretical case, and for S/Ns 1A and 2A. Theoretical calculations are from large signal analyses at constant α, although the same dependence of current and magnetic field can be seen in small signal oscillation threshold analyses (Figure 3-6) since optimal power occurs close to threshold (Figure 3-8).

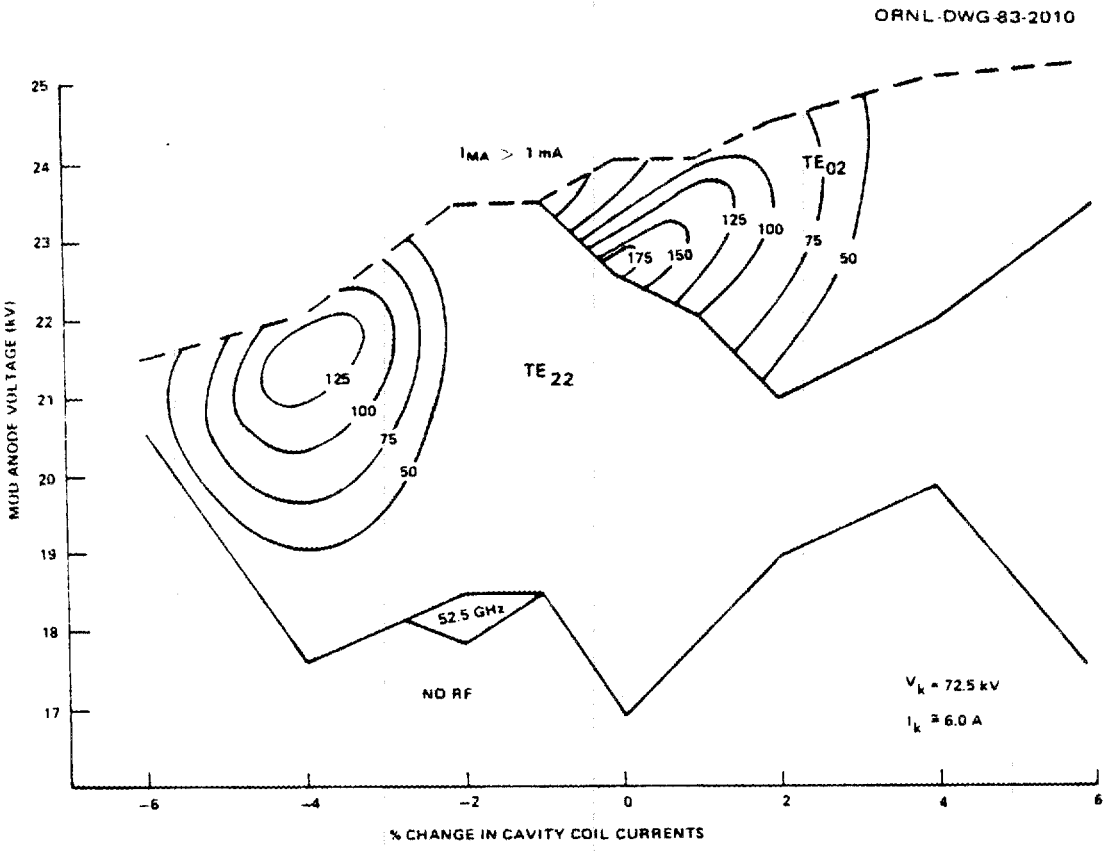

Figure 5-15 S/N 2A mode map. Curved contours represent lines of constant power.

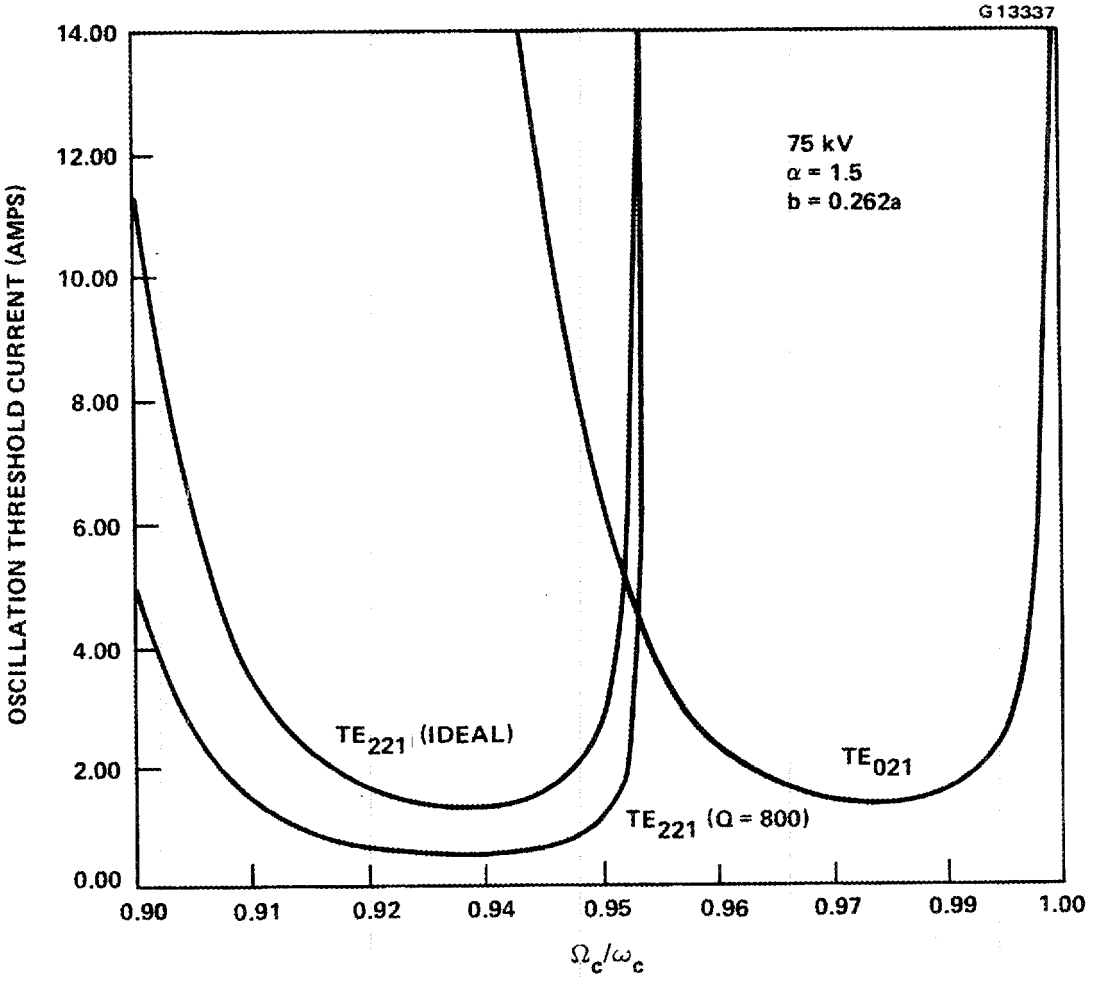

Figure 5-16 Oscillation threshold conditions for the TE_{021} and competing TE_{221} mode under ideal output conditions, and for an output mismatch.

5.7 S/N 1A LONG PULSE TESTING

Satisfied with the design and short pulse performance of the tube, long pulse testing of S/N 1A in the 1 to 100 ms regime was begun. It was soon discovered that the water load, though apparently adequate for 28 GHz use at these power levels, would need modification to prevent serious surface boiling at 60 GHz where the skin depth of penetration is considerably less. Processing of the tube to full beam power at 100 ms pulsewidth continued, however, with the power detuned to 110 kW (Figure 5-17). As load modifications became available, the power was gradually increased. Unfortunately, while testing at 150 kW, 60 ms, a catastrophic waveguide arc occurred which went undetected by the arc detector and caused a window fracture with subsequent loss of vacuum.

The waveguide arc detector being used at this time had been successfully checked out on a daily basis, with its own test light, as well as immediately after the tube failure. It had also been used successfully many times to detect arcs in high power TE_{10} radar set-ups, being sensitive to light near the center of the waveguide only. This insufficiently sensitive arc detector was replaced with a far more sensitive, high gain photomultiplier tube-based unit.

S/N 1A used a single, face-brazed beryllia window.

5.8 S/N 2A LONG PULSE TESTNG

With the newly developed high-confidence baffling scheme for the water load, and having replaced the insensitive arc detector, processing to 100 ms, 200 kW levels was begun on S/N 2A. Although mode competition considerations prevented attaining high efficiency at high power levels, this was still the first Hughes tube to successfully reach 200 kW TE_{02} output at 100 ms pulsewidths (Figure 5-18). However, this much less mechanically capable window (edge-brazed single Al_2O_3 disc) eventually failed under repeated thermal stressing at long pulsewidths.

ORNL-DWG-83-2003

LONG PULSE TEST WAVEFORMS
917H S/N 1A

RF PULSE

E4083

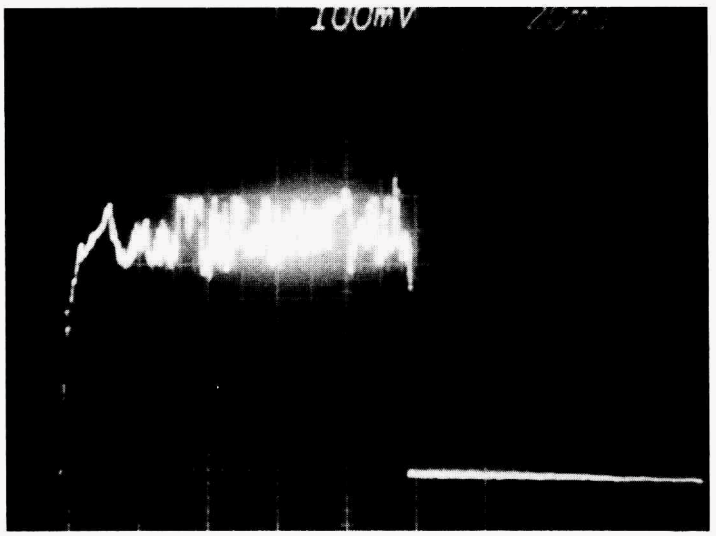

t_p = 100 ms

V = 0.1 Amp/Div

H = 20 ms/Div

Figure 5-17 RF pulsed waveform, detected from sampling hole in output waveguide. Hash on pulse top is indicative of water load boiling.

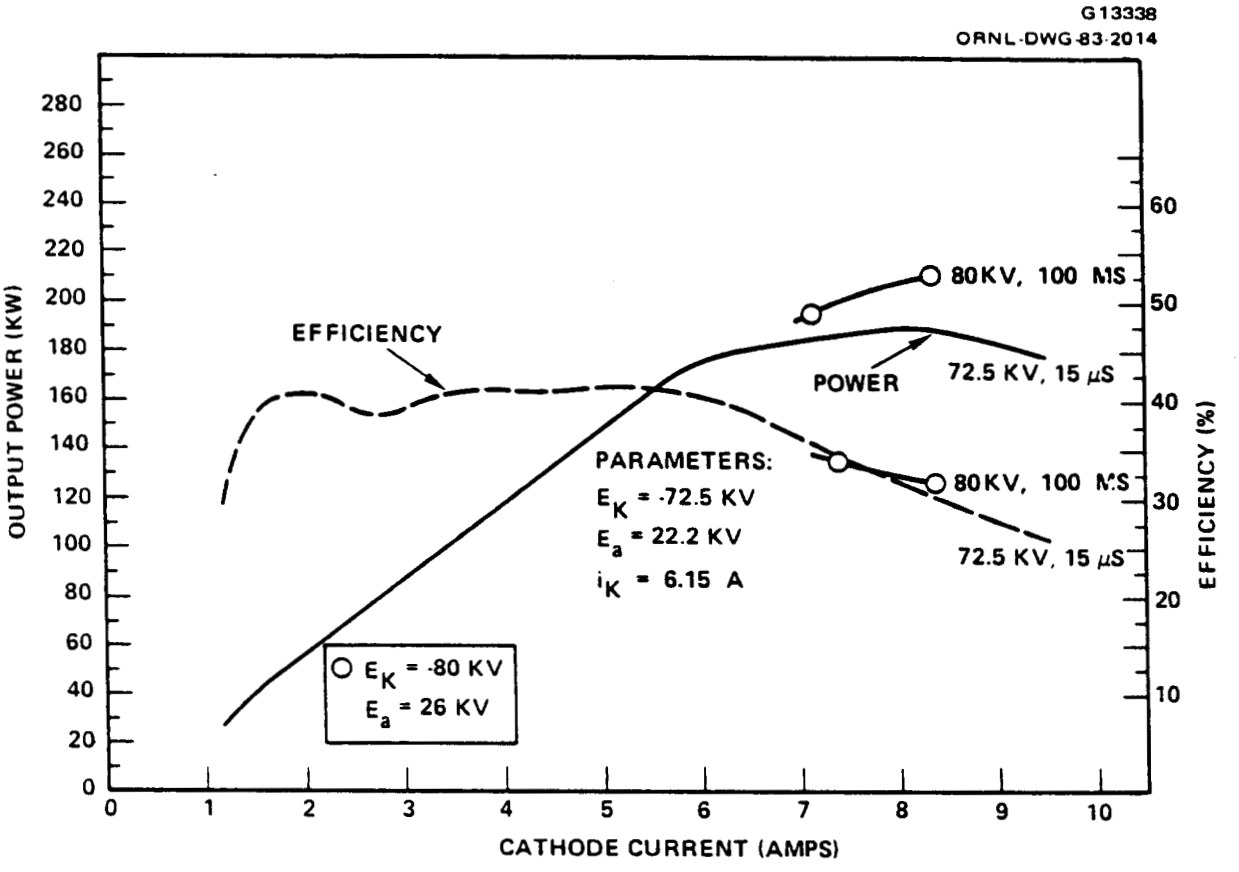

Figure 5-18 Power output and efficiency versus beam current for long and short pulse operation.

5.9 S/N 1B

S/N 1A was reworked with another single disc beryllia window and with the new gun design optimized for tapered cathode magnetic fields. Since it also contained the finalized "long" drift tube, S/N 1B would serve as a pulsed test vehicle for the final gun design destined for the CW tube, S/N 3. Unfortunately, a degradation in the current handling capability of the internal lead of the fourth superconducting coil prevented using the high efficiency, optimal magnetic field profile on S/N 1B. Being constrained to keep coil 4 current less than 34 A, alternate coil settings were found that reproduced the required field in the cavity and the gun with only slight variation magnetically in the drift region (Figure 5-19). When this field had been tried on S/N 1A, a reduction in obtainable alpha and overall efficiency was witnessed, but since a new solenoid system was on order and testing of S/N 1A by that time centered on long pulse testing at detuned power anyway, this was not considered a hindrance. However, HEDD was subsequently directed to cancel the new magnet order and efficiency on S/N 1B was thereby limited to 35% (Figure 5-20). Operating the tube in this field profile but at parameters that yielded 40+ percent efficiency on S/N 1A yielded the non-uniform drift tube heating profile of Figure 5-21 as well as excessive anode current and greatly reduced efficiency, indicating insufficient field was available in the drift tube to avoid the efficiency-robbing effects of the beam instability.

5.10 S/N 3 AND ITS PROPOSED REWORK

The salient features of S/N 3 were:

- High power, FC-75 cooled double disc window -- though not as attractive in bandwidth response as the multi-disc design, the high power test results of the 28 GHz multi-disc window model were not available to justify or disparage the thermal transfer characteristics of the multi-disc design. Hence the choice of the double disc design for this CW device was made.

- Down taper -- whereas S/N 1 and 2 had used a simple linear downtaper from the 3.5 inch collector to 2.5 inch window, S/N 3 used a non-linear design for reduced mode conversion.

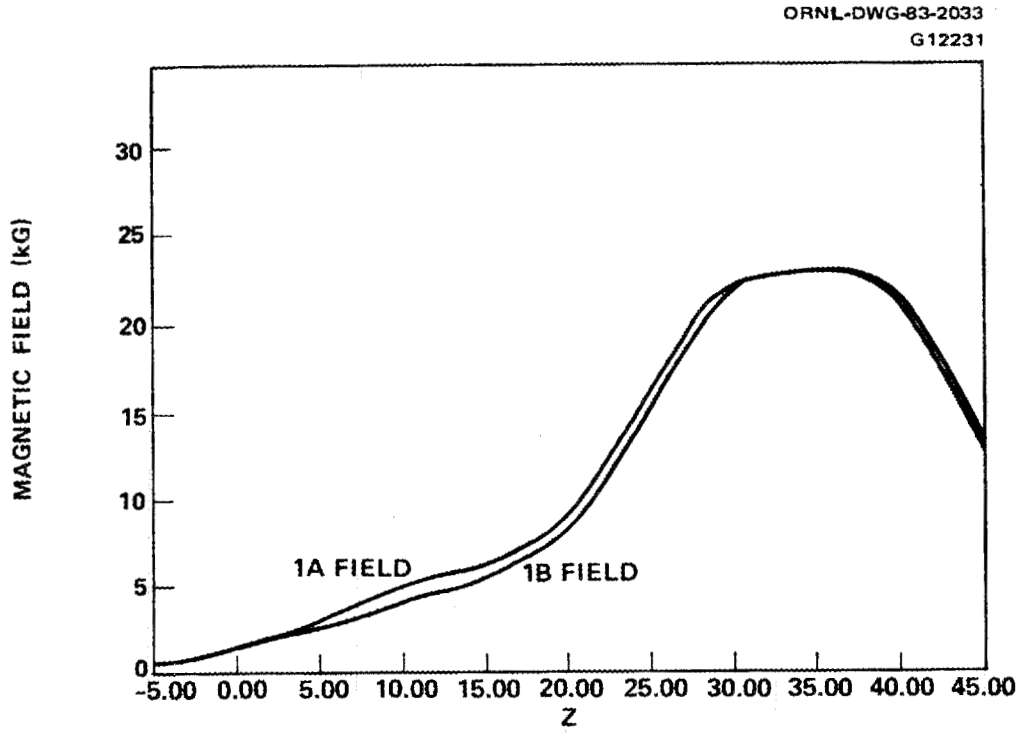

Figure 5-19 Comparison of 2 applied magnetic fields.

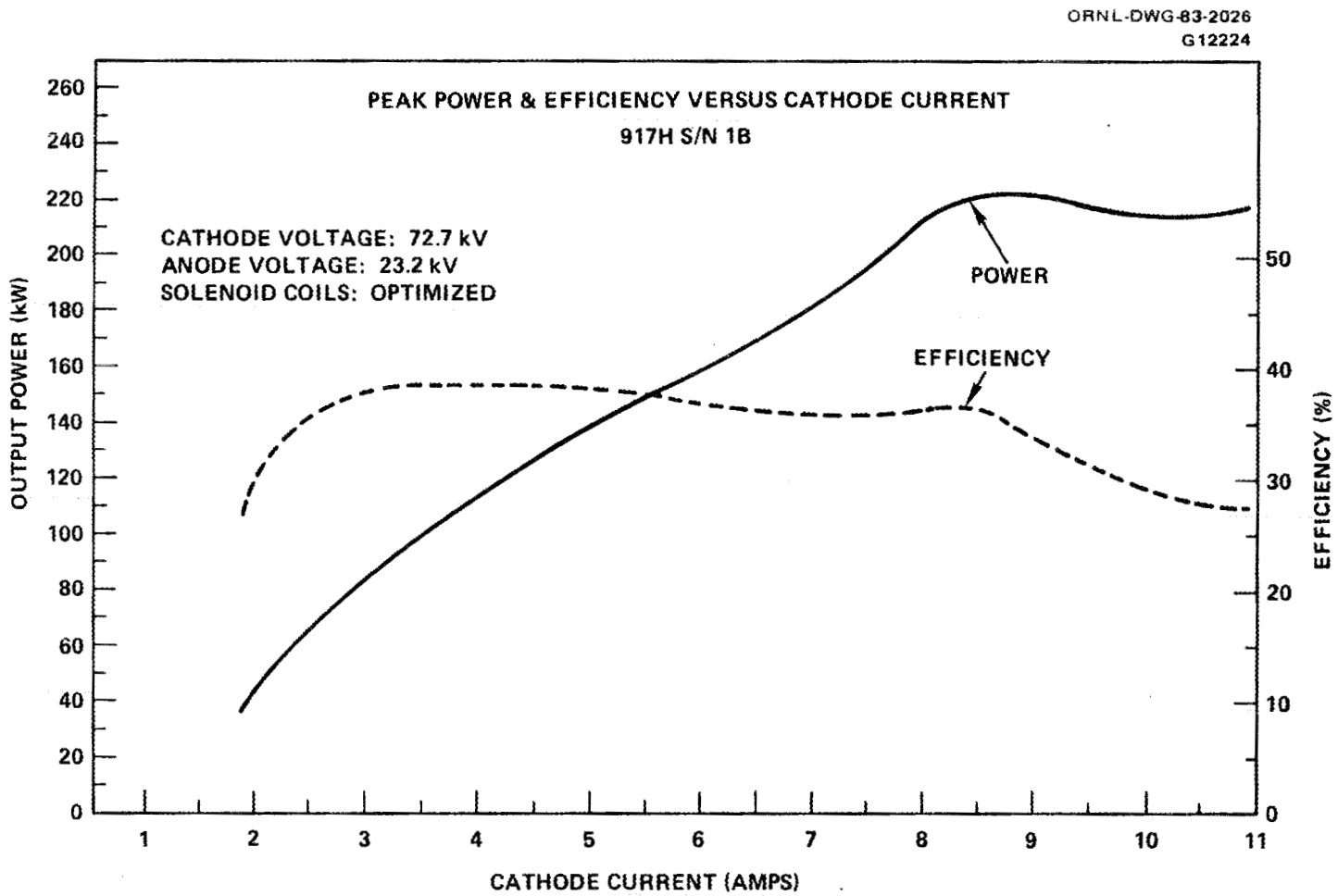

Figure 5-20 Peak power and efficiency vs cathode current.

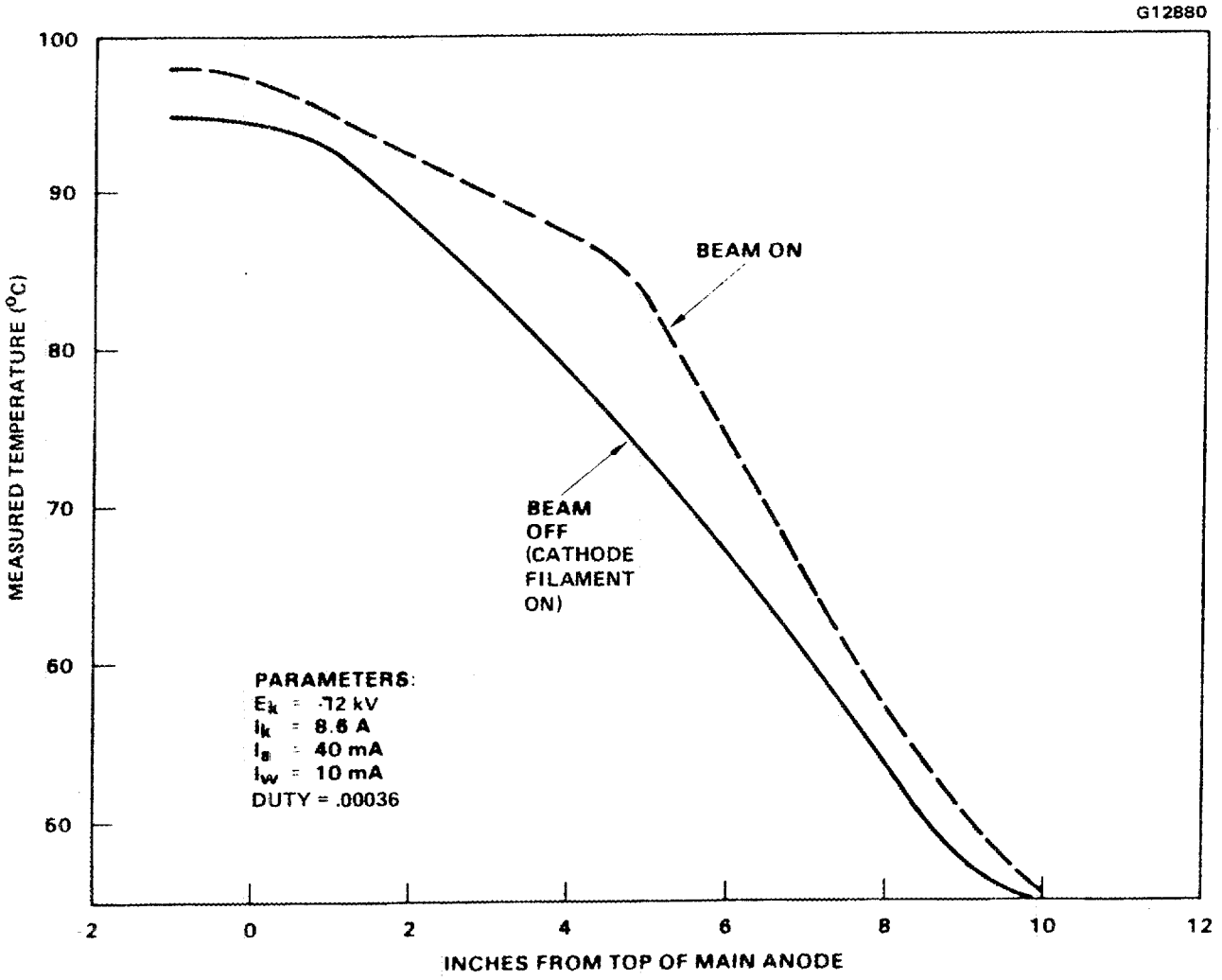

Figure 5-21 S/N 1B drift tube thermal measurements without coolant, showing localized microwave heating in the drift tube. (The approximate 5°C/inch gradient shows the significance of the cathode thermal source on the left; the 3°C offset between the two conditions reflects the half hour difference in measurement required to resolve the hot spot. Beam scrape-off heating, though negligible of this duty, would be concentrated at the cavity end where the beam is closest to the wall.)

- Collector -- CW, finned collector similar to tested mock-up model that easily handled 345 gpm of coolant. (S/N 1 and 2 had used a smooth, thin-walled copper collector for simplified electron distribution measurement.

- Gun -- The optimized, long drift tube, tapered gun magnetic field design as incorporated in 1B.

- Drift tube -- Identical to that in S/N 1A and 1B except the last 3 cm of loss rings were replaced by a solid copper beam scraper by direction of program management.[2] This beam scraper (plasma sprayed with lossy material) was included for CW thermal ruggedness and additional attenuation of any TE_{01} leaking back from the cavity.

Test results were discouraging with oscillation being dominated by a low Q resonance centered at 53.7 GHz and 64 kW peak output power (Figure 5-22). Oscillation in the TE_{021} mode would only occur at cavity magnetic fields in excess of 23800 gauss; levels at which efficiency is greatly reduced, resulting in a maximum TE_{02} power of 40 kW. Thermal measurements of the drift tube (Figure 5-23) at parameters consistent with high efficiency oscillation showed severe drift tube heating attributable only to the drift tube modification. It was concluded that a TE_{211} resonance in the long beamscraper is partially coupled out toward the gun, being lossed out in the drift tube (giving body heating) and partially transmitted out the window. The modulation this undesired oscillation imparts to the beam prevents TE_{02} interaction until the magnetic field is raised sufficiently high to avoid TE_{21} interaction completely. However at these values, predicted (and measured) efficiency is quite low.

It is therefore proposed to repair S/N 3 by replacing the beamscraper section with the original discs, electrically identical to S/N 1B but mechanically reconfigured to be thermally compatible with CW operation.

5.11 919H-53

Built for Kyoto University, Japan, the 919H-53 (Figure 5-24) is a 100 ms pulse version of the 917H at 53.2 GHz. It featured a broadband multi disc window

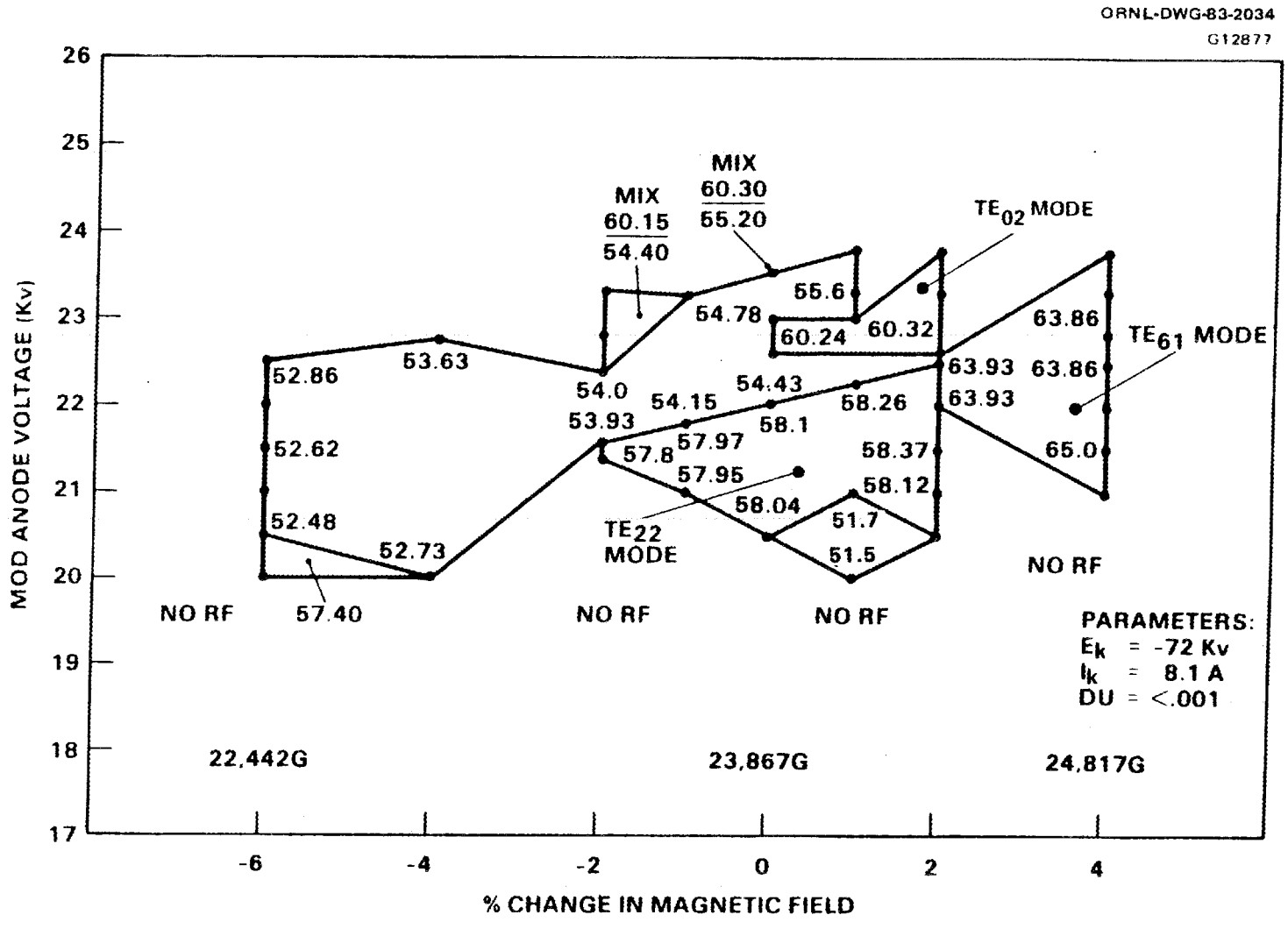

Figure 5-22 Short pulse mode map, S/N 3.

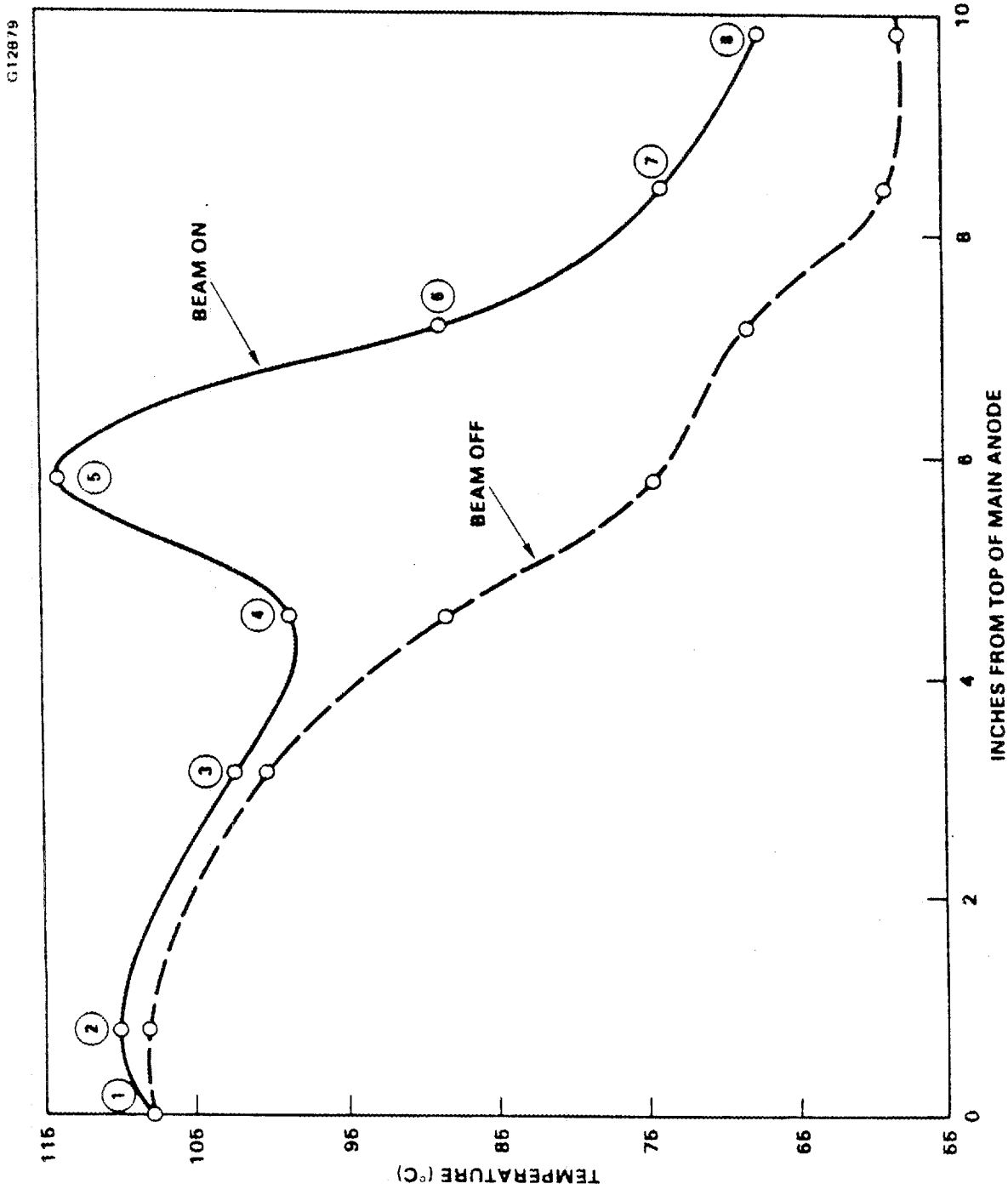

Figure 5-23 Drift tube thermal measurements, S/N 3.

E4689

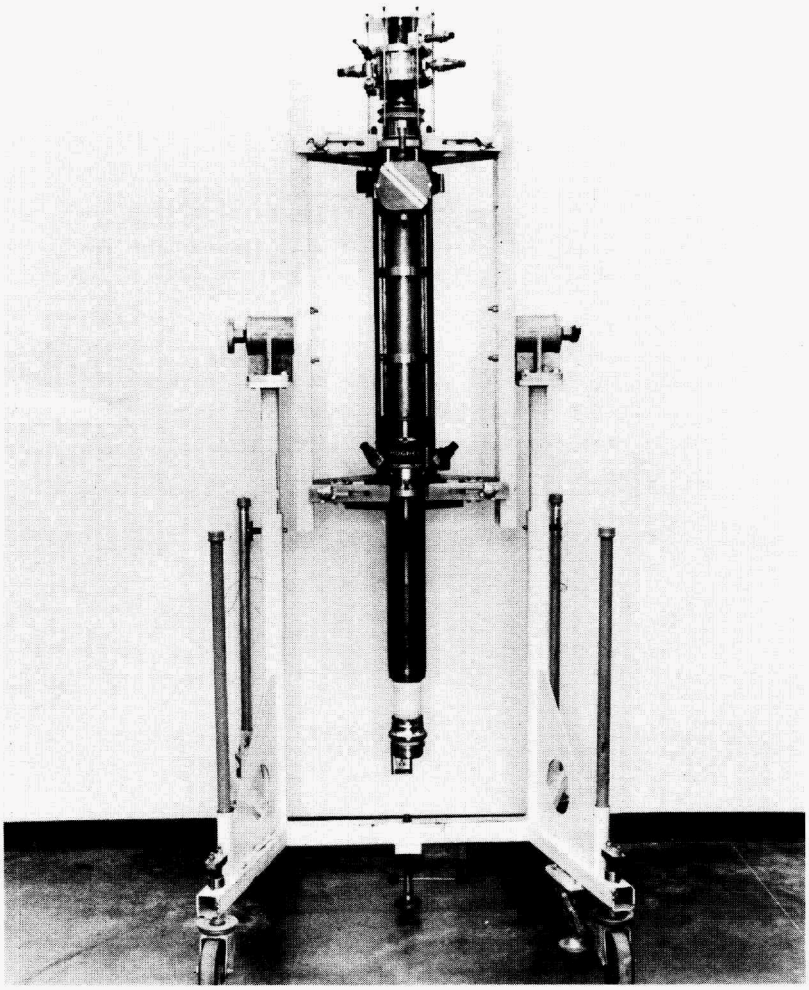

Figure 5-24 The 919H-53 pulsed gyrotron.

(measured VSWR less than 1.25 from 48-56 GHz) a 2.5 inch diameter collector, a low mode conversion nonlinear uptaper, and a thermally isolated cathode (refer to Figure 2-5).

Several other features were able to be incorporated into the 919H. These included a new insulator choke design which enabled high TE_{0n} transmission through the taper, collector and window sections, without RF emanating from the insulators. Therefore separate cooling of the collector insulators was not required. In addition, the method of pumping-out the collector was made to be completely symmetrical to minimize waveguide discontinuities and to preserve low mode conversion.

Due to the frequency requirement, the cavity magnetic field was scaled by frequency and the cavity, cavity end of the drift tube, and cathode field (to maintain b/a = .262) were scaled by wavelength. This allowed the use of the 917H electron gun, although the reduced gun to cavity magnetic compression ratio would require additional anode voltage to achieve the same high cavity alpha. (Though not used, parts for a backup gun design with reduced anode voltage and voltage gradients were ordered in case excessive gun arcing was observed on test.)

A new solenoid design requiring only four adjustments was specified by HEDD and constructed by Hitachi.

The tube demonstrated "full spec" performance of 200 kW in 100 ms pulsewidths at 1% duty. The thermally efficient collector was run at 20 gpm with a measured 20 psi drop. The broadband window allowed efficient operation in the TE_{22} mode with an exceptionally broad operating range for TE_{02} (primary mode) operation (Figure 5-25). Excellent dynamic range by anode voltage alone is shown in Figure 5-26. Waveguide mode patterns, burned on thermal paper, showed low levels of radial and axial mode beating (Figure 5-27) which is only possible with very high (>95%) mode purity.[3]

The successful operation of the 919H-53 proved the soundness, scalability, and commercial producibility of the basic 917H design.

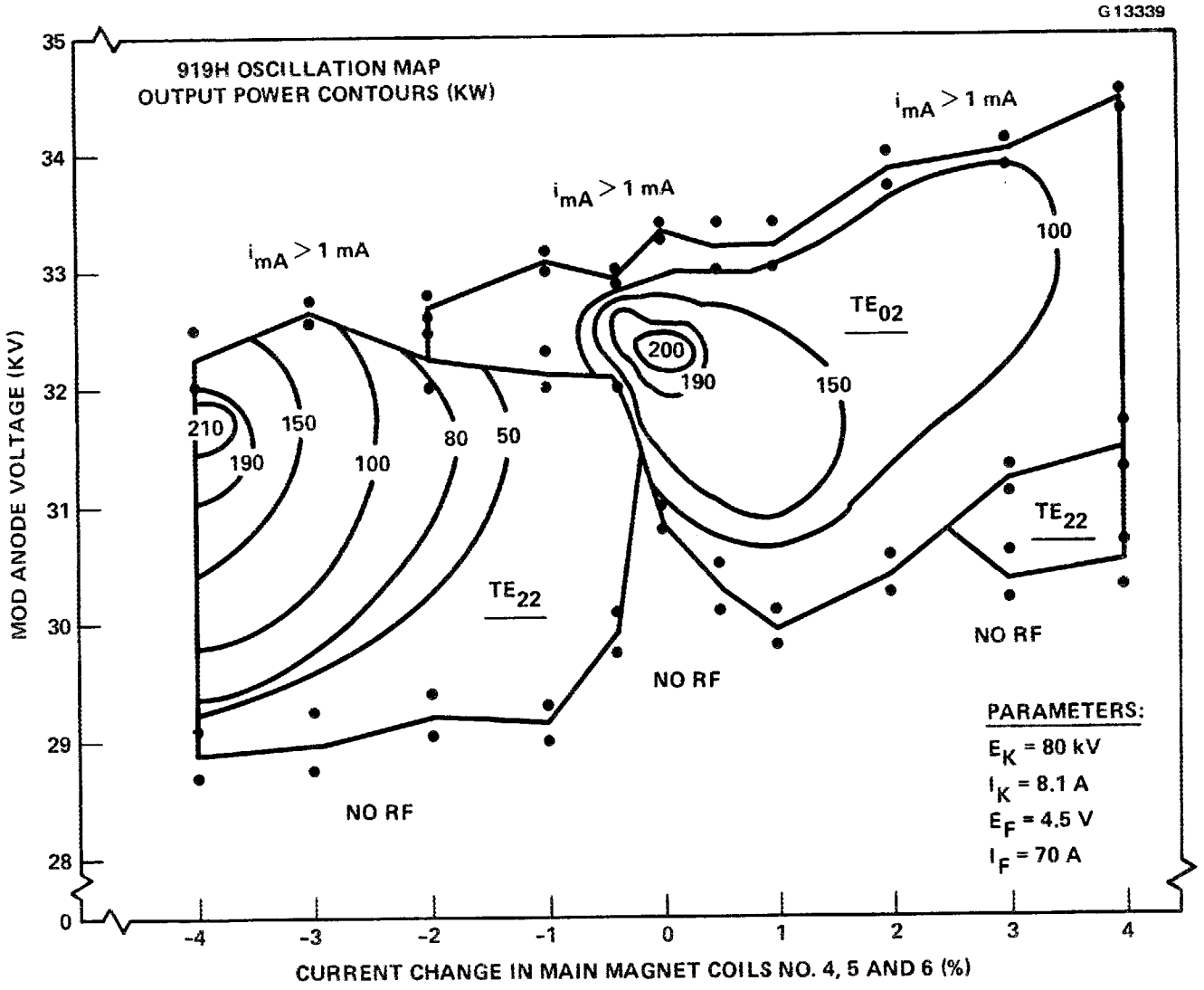

Figure 5-25 Oscillation mapping of the 919H-53.

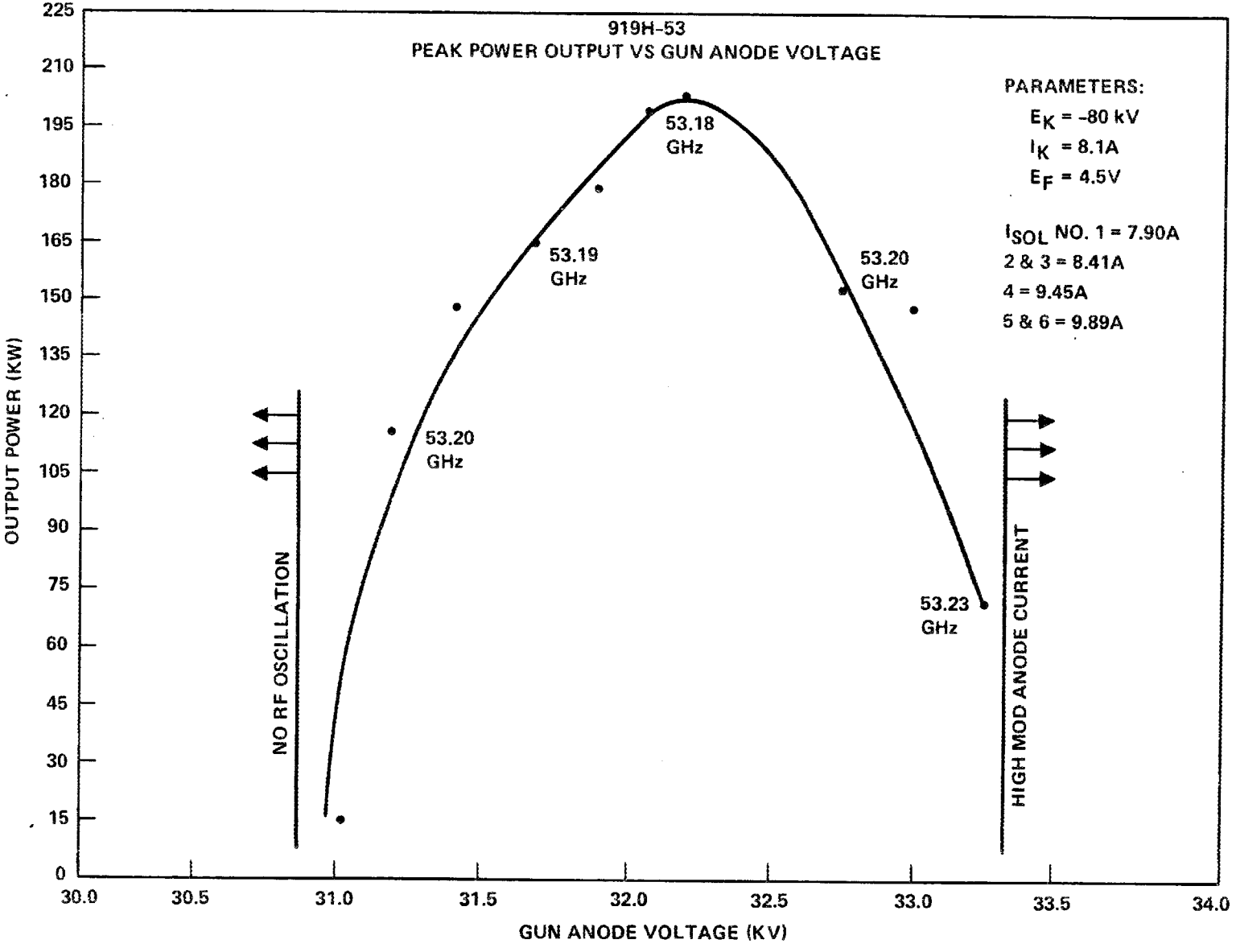

Figure 5-26 Dynamic range of the 919H-53.

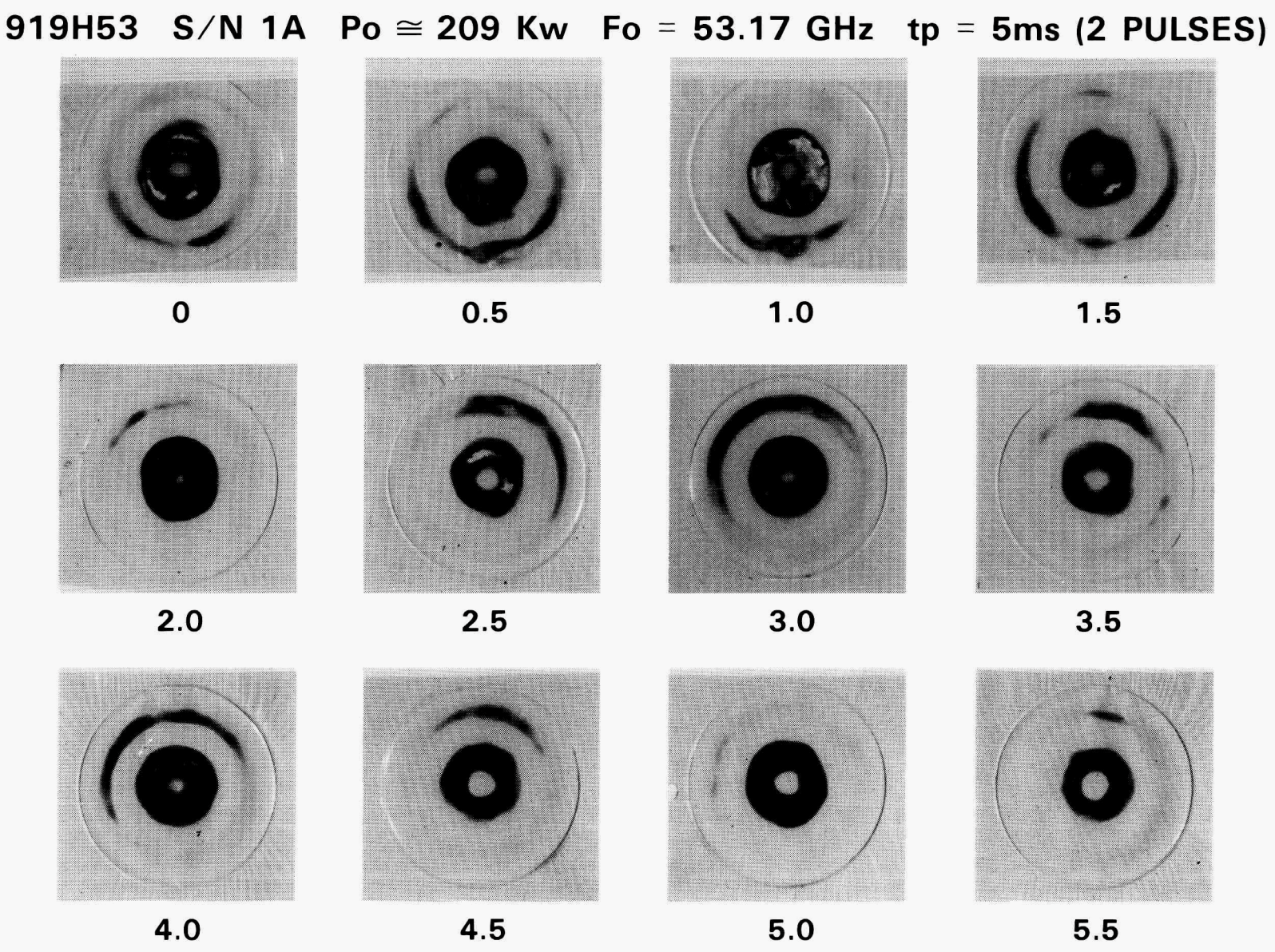

Figure 5-27 Thermal paper "burn" patterns taken at 0.5 inch axial intervals along 2.5 inch diameter waveguide.

E4691-2

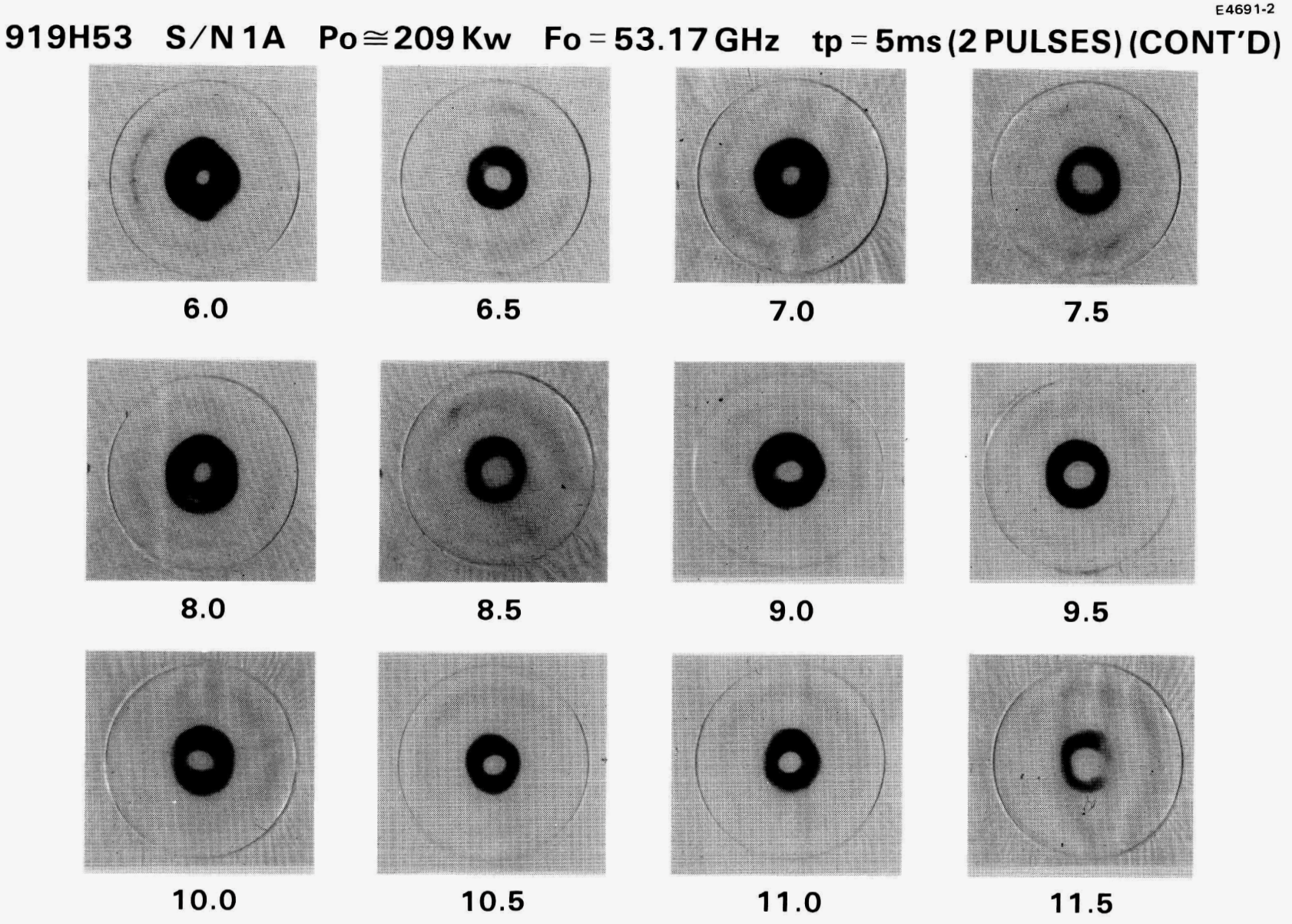

Figure 5-27 (Continued)

919H53 S/N 1A Po ≅ 209 Kw Fo = 53.17 GHz tp = 5ms (2 PULSES) (CONT'D)

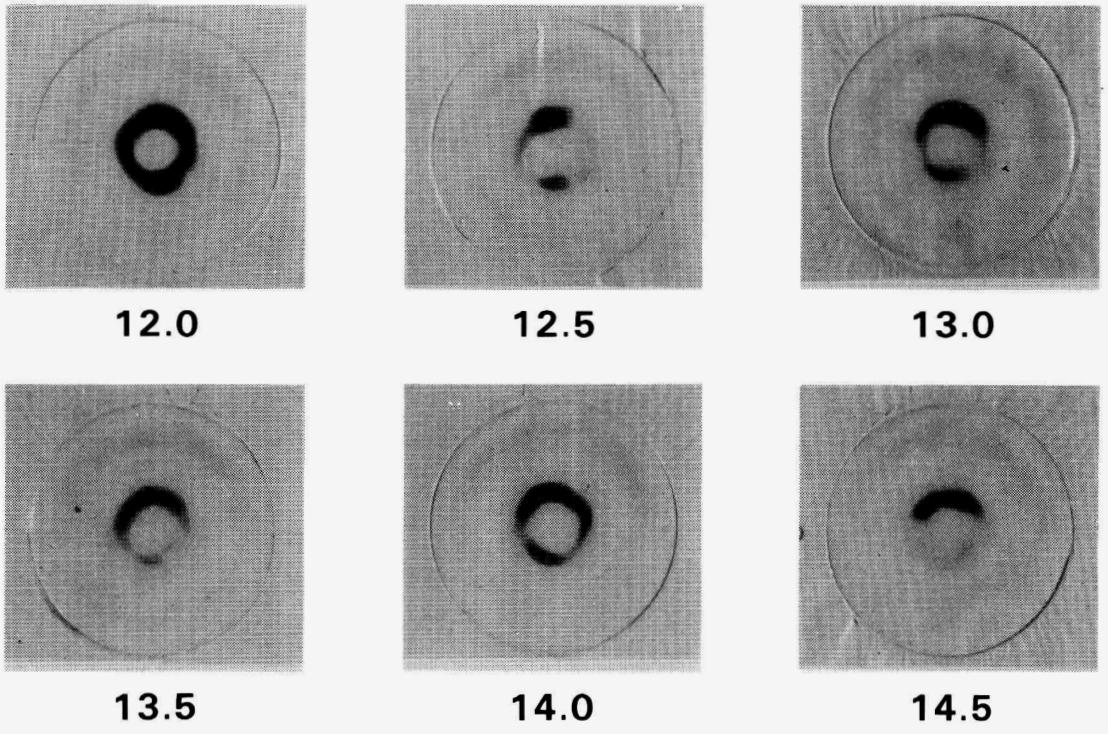

Figure 5-27 (Continued)

6.0 WATER LOADS AND ATTENUATORS

Initially, device termination and calorimetery of the HEDD gyrotrons was satisfactorily accomplished with a commercially available, 2.5 inch diameter water load (rated at 200 kW CW at 28 GHz by its manufacturer, Varian Associates, Palo Alto, CA.) However, as long pulse testing was commenced on S/N 1A, it became apparent that the combination of increased frequency and imaginary dielectric constant (for temperatures above 50°C) caused a significant decrease in skin depth at 60 GHz. The resultant surface boiling (Figure 6-1) caused large fluctuations in VSWR (and effective cavity Q) preventing maximum power transfer to the water as well as causing eventual cavitational erosion damage (Figure 6-2) to the conical ceramic. Initial attempts with increased backpressure or partial ethylene glycol mixes showed insignificant improvement.

Some degree of success, however, was achieved with a simple baffle arrangement to increase the flow velocity on the cone surface. Next, a baffle arrangement utilizing various details of baffle rings and spacers (Figure 6-3) was constructed for concentrated flow velocity and turbulence at any desired part of the load. An acrylic housing was fabricated to serve as visual diagnostic aid in locating critical boiling areas as power and pulsewidth was progressively increased.

Along with a widened inlet boss (for reduced flow restriction) and a cone fixturing method guaranteeing concentric alignment of cone apex and waveguide axis (to ensure symmetric power dissipation) this flexible baffling technique was incorporated into the Hughes water load (Figure 6-4). This allowed problem-free testing to full power and pulse width at flow rates (35 gpm) readily available from the UVC modulator and consistent with precise calorimetric power determination.

In parallel with the final load effort, a lossy-wall attenuator (Figure 6-5) was developed. Approximately 1.2 dB of attenuation was obtained with no change in rf match. Further development of attenuators is foreseen as gyrotron powers increase.

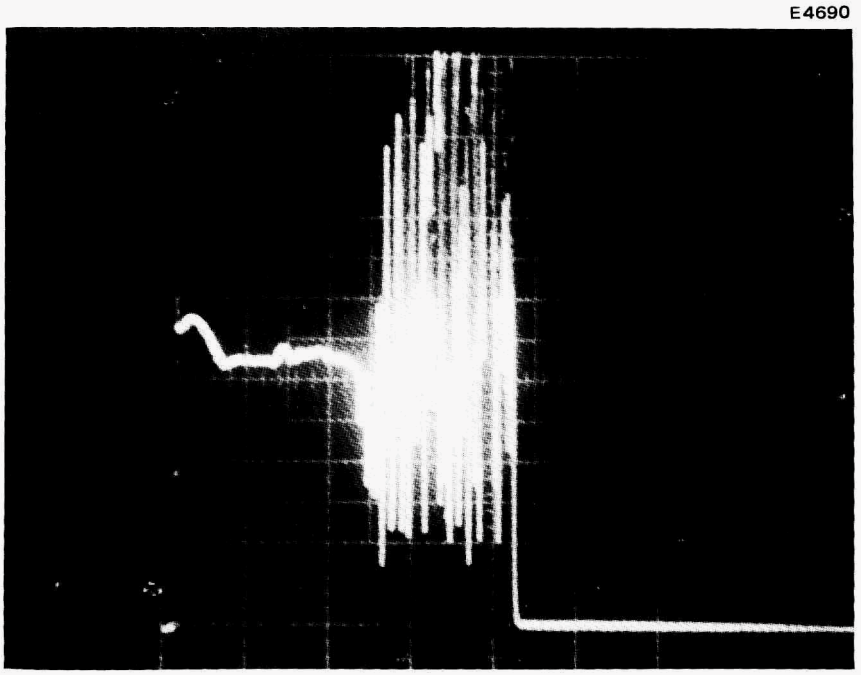

Figure 6-1 RF output pulse showing onset of water boiling.

E4439
ORNL-PHOTO-0129-83

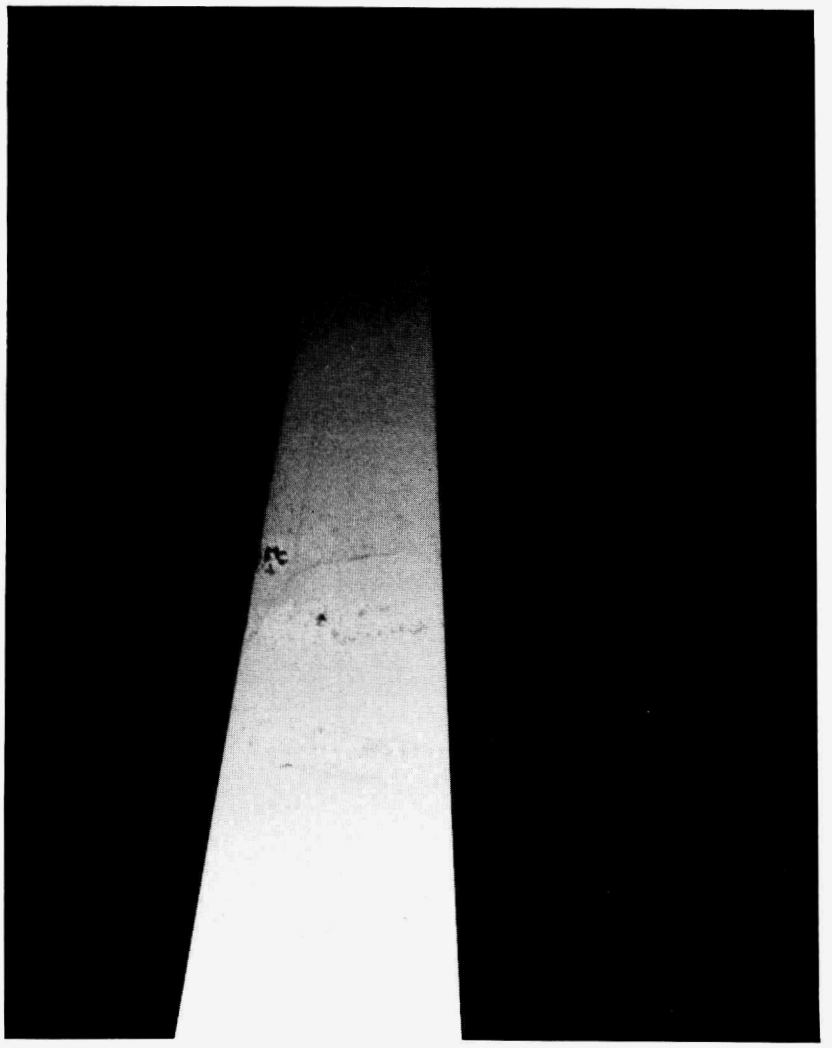

Figure 6-2 Alumina cone from RF water load showing crack and erosion after 100 ms testing.

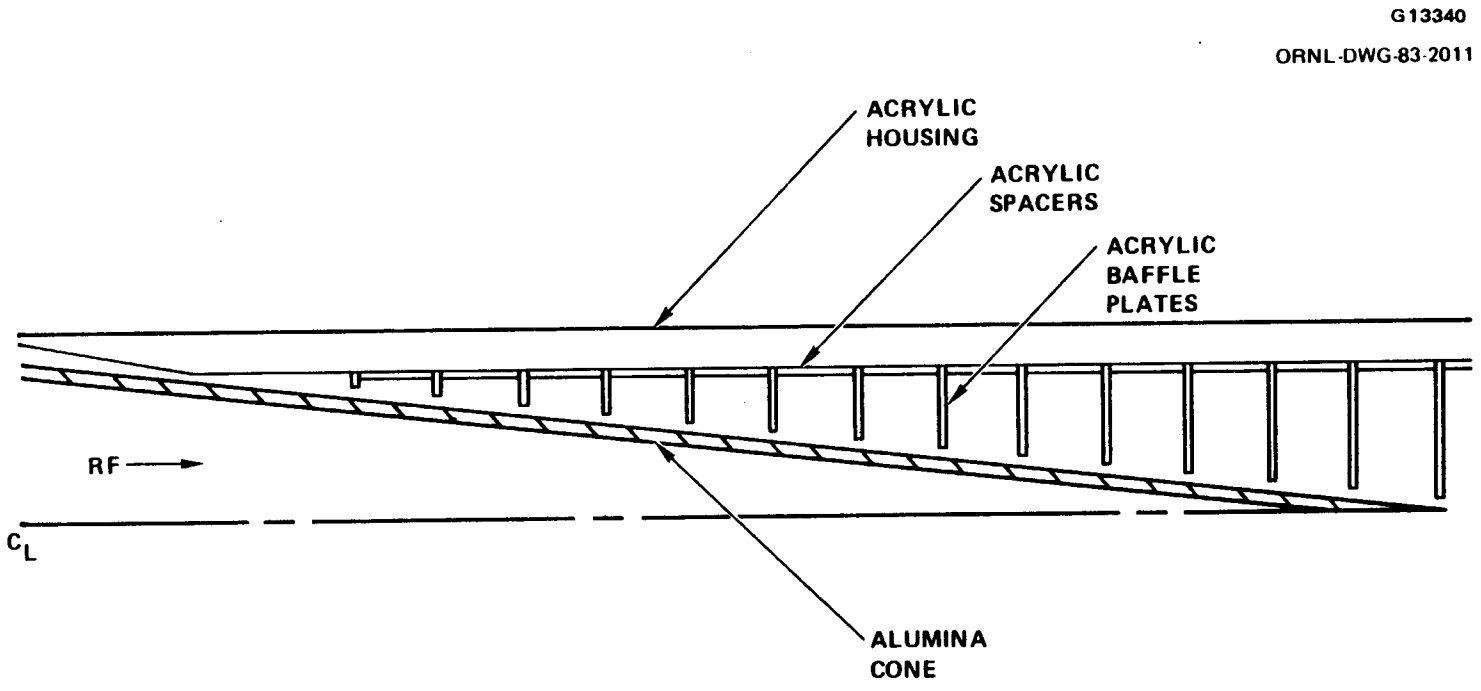

Figure 6-3 RF water load baffle arrangement.

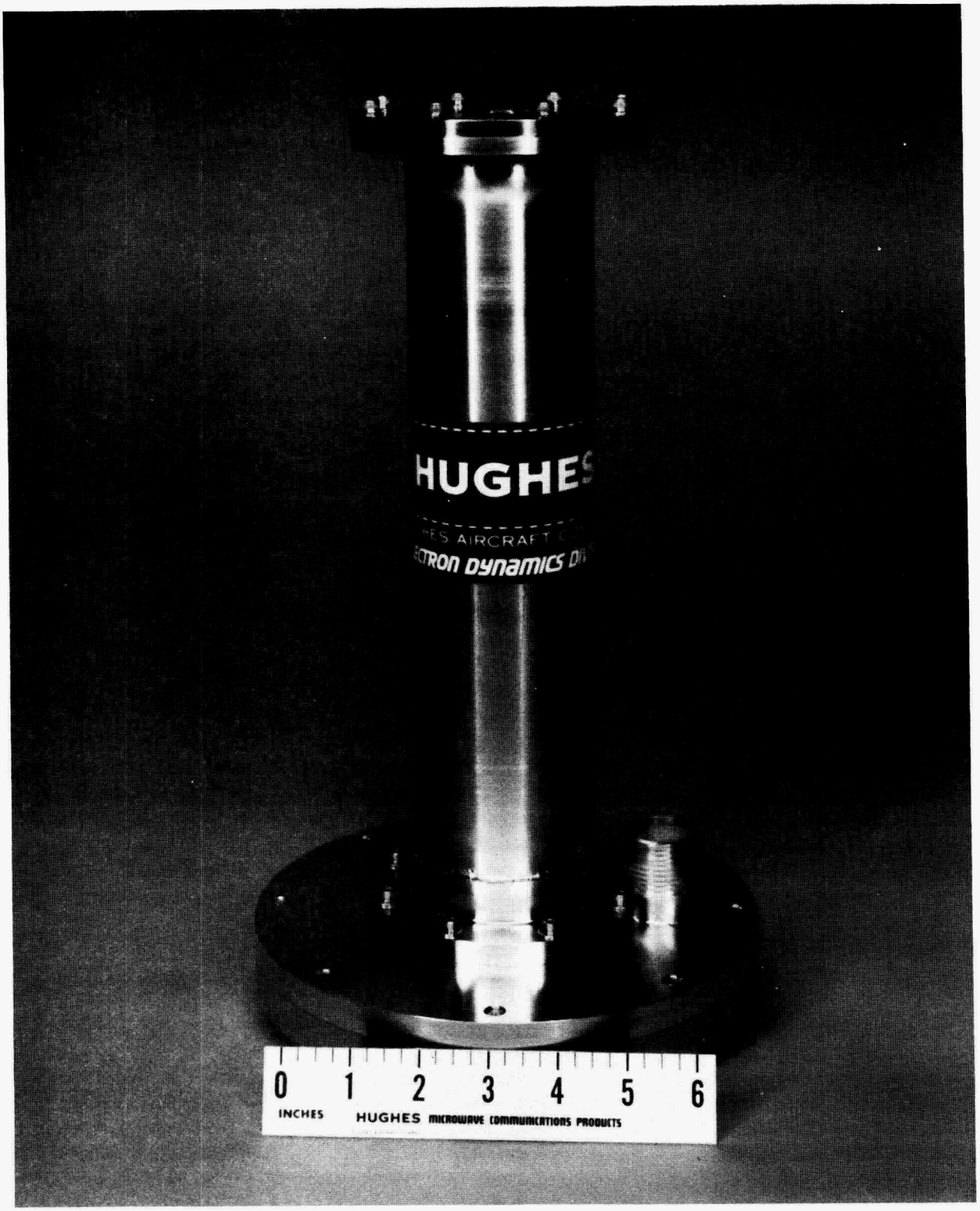

Figure 6-4 Hughes 60 GHz, 200 kW water load.

ORNL-DWG 84-2777 FED
E4536

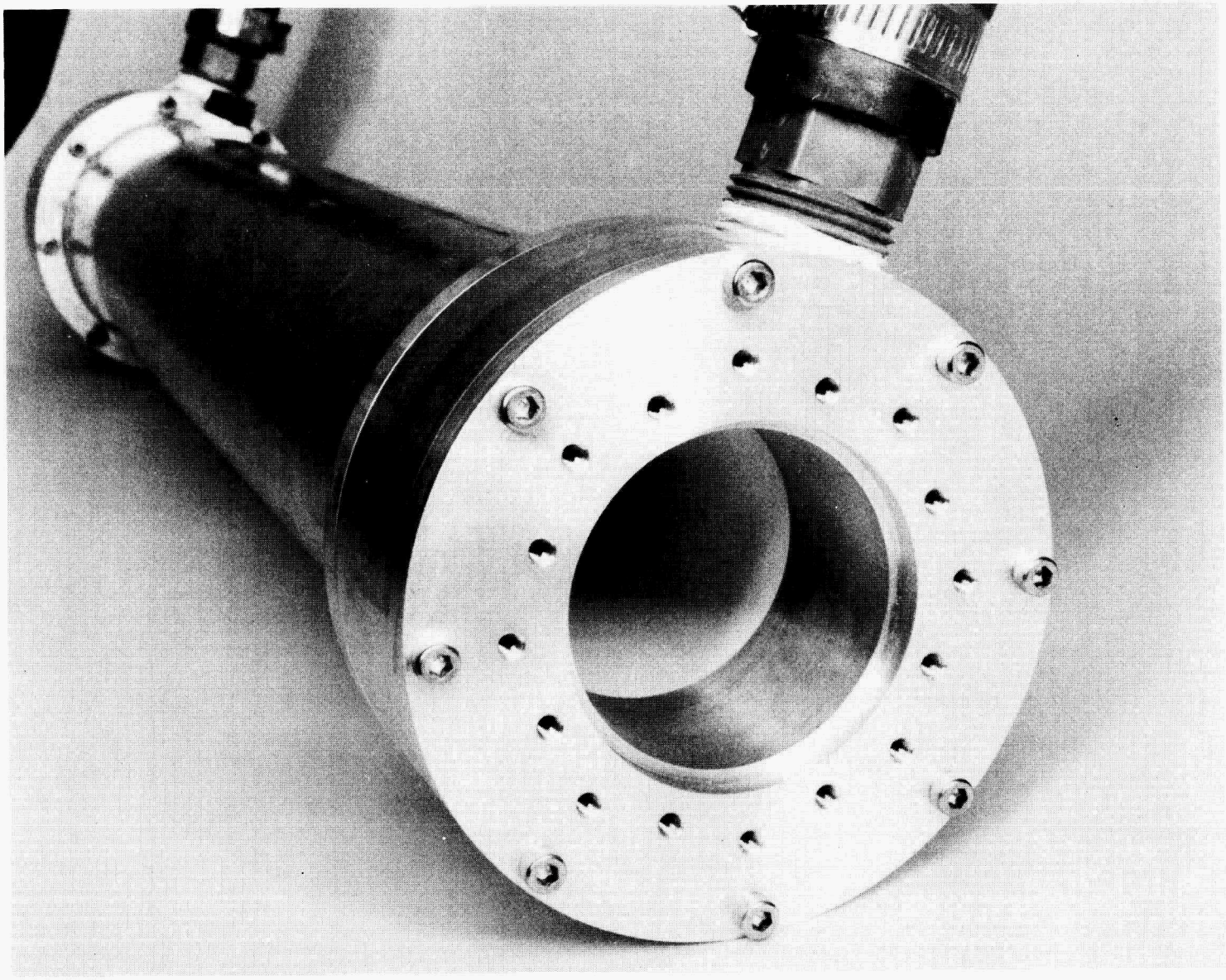

Figure 6-5 Hughes 2.5 inch I.D. lossy wall attenuator.

7.0 HIGH VOLTAGE FACILITIES

High voltage, high power test facilities were recognized to be a crucial part of the gyrotron development program. A one megawatt CW (100 kV, 10A) test facility was included in the original program plan. A power supply and heat exchanger were to be purchased from program funds, which would provide a test capability from short pulse to CW.

Toward the end of 1979, the availability of the Army's Missile Site Radar (MSR) transmitter, as surplus equipment, became known. The transmitter power supply located on Kwajalein atoll in the Marshall Islands, had a capability up to 3 MW (150 kV, 20A) CW. This power supply would provide Hughes with the ability to operate MW gyrotrons which were anticipated as the next generation of gyrotrons, or alternatively, multiple 200 kW tubes in parallel. Since no program funds were yet committed to the proposed test facility, it was decided to obtain the MSR power supply.

Utilizing gyrotron development funds, the MSR power supply was dismantled and shipped to Hughes in August 1980. Also shipped were the ancillary high purity cooling system, including water-to-water heat exchangers and pumps, 200 kV high-potter, and monitoring equipment. During dismantling, slight mechanical damage to the high voltage transformer occurred, and during shipment one portion of the capacitor bank was severely damaged. Everything except the high-pot power supply was put into storage until facility funds could be obtained, which was not until late 1981.

During the interim, HEDD had modified an existing power supply for operation to 20 μs at 70 kV and up to 15 amps, at duty cycles of less than 2%. This supply became the Short Pulse Modulator. Facility space up to 9000 square feet was alloted for gyrotron assembly and test, as shown in Figure 7-1.

In April 1981, the components of a 100 ms pulse modulator were furnished to Hughes by DOE. This power supply was originally constructed by Universal Voltromics Corp. (UVC) for General Atomic, who provided it to the Japanese Atomic Energy Research Institute (JAERI) for use on JFT-2. The power supply

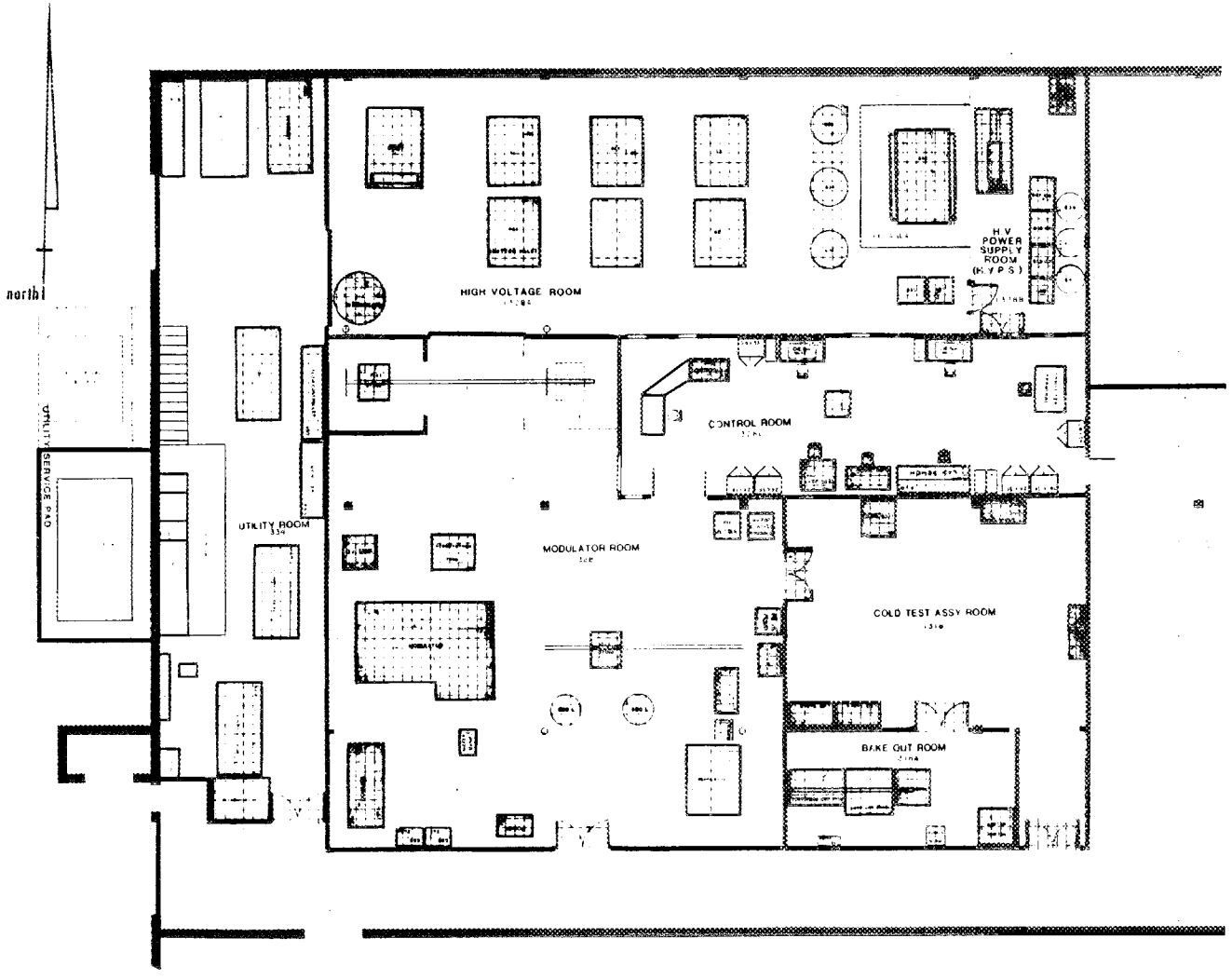

Figure 7-1 Facility layout.

was used to operate a 28 GHz gyrotron to 40 ms pulsewidth. The UVC modulator has a capability of 90 kV, 10A, a pulse width of 100 ms at a duty cycle limited by the charging rate of the power supply to 0.4%. Full 100 ms operational capability was achieved in January 1982.

Funding for a CW test facility was received in FY-82. A plan was generated which would utilize components of the MSR power supply with the modulator of the UVC power supply. A schematic of the electrical plan is shown in Figure 7-2. Because components of two different power supplies were being married, a new system of controlling the supplies had to be devised, as well as monitoring for the CW gyrotron. These plans were formallized and presented at a Preliminary Design Review in March 1983. Useful comments from this review were incorporated into the design plan. Specifications were drawn up for new components and construction, and quotes were solicited. Site construction was started with a pit for the MSR high voltage transformer.

In November 1983, funding for the CW Test Facility was halted. All plans and drawings were cataloged and stored for future reference. The UVC modulator for Medium Pulse operation has undergone some upgrading, but is essentially intact for use at 100 ms pulse widths.

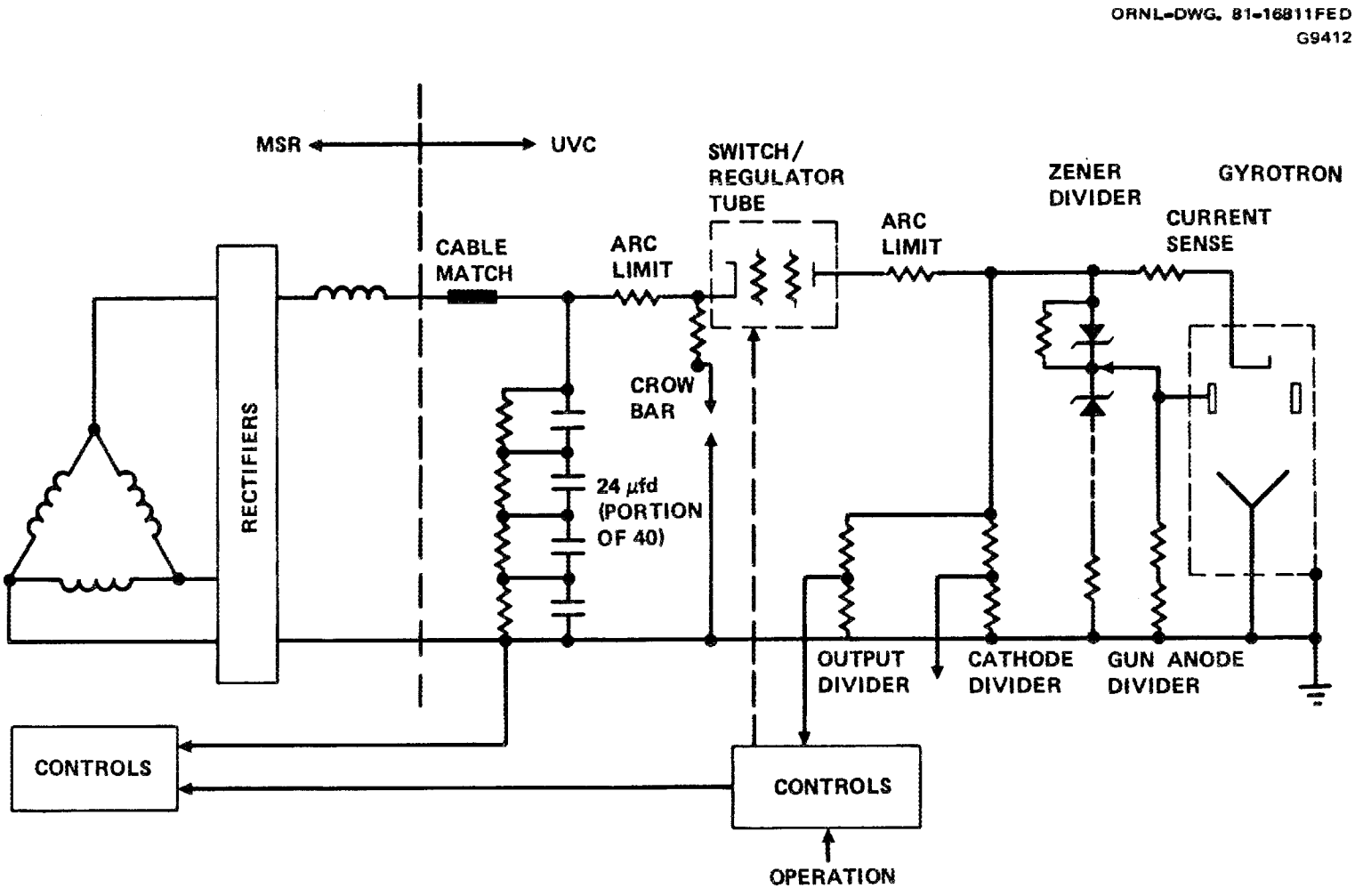

Figure 7-2 Schematic representation of proposed CW supply and modulator.

8.0 CONCLUSIONS AND RECOMMENDATIONS

8.1 CONCLUSIONS

8.1.1 Gyrotron Results

The Hughes EDD gyrotron development program for DOE was paced by funding limitations, several program redirections, and management direction to maintain consistency between experiments. Nevertheless, the second tube constructed basically met the final program objectives of 200 kW output with 100 ms pulses. With additional program time, it could have been shown that the first tube (S/N 1B) actually met the program requirements.

Table 8-1 highlights the results of the gyrotron tube development. All tubes were constructed to be electrically CW relevant; that is, the tubes were electrically identical to the intended CW tube, as far as the electron beam and RF are concerned, except for the vacuum window. Thus, all tubes employed a 3.5" ID collector which was evaluated to be adequate to dissipate 640 kW of DC beam power with the Hughes solenoid.

S/N 3 was the first tube to utilize full CW cooling and a CW-relevant double-disc BeO window. One other recommended change was the incorporation of a water-cooled beam scraper before the cavity. Recognizing the potential of producing undesired gyrotron oscillations within a beam scraper, the walls were tapered and coated with lossy material. These measures, however, when combined with high VSWR from the narrow bandwidth, double-disc window, were insufficient to prevent a 53 GHz oscillation from starting within the beam scraper. With the beam inadvertently pre-bunched, output at 60 GHz was severly degraded.

A thermally-ruggedized drift tube was designed, electrically identical to S/N 1A. However, program funds were not available to implement this improved design.

8.1.2 Gyrotron-Related Accomplishments

The course of state-of-the-art development programs in areas of new technology often require innovation in design, construction and test techniques related

TABLE 8-1

HUGHES-DOE GYROTRON ACCOMPLISHMENTS

S /N	Features	Accomplishment
1	CW relevant, except single disc BeO windows; High Q cavity	160 kW peak output short pulse
1A	Revised cavity	285 kW peak output short pulse, 44% efficiency; 150 kW 60 ms pulse (power limited by RF load)
1B	Rebuilt gun and window	223 kW peak output, short pulse, 35% efficiency with impaired magnetic field; 203 kW, 70 ms pulse (by end of contract)
2	Same as S/N 1A except revised cathode, assembly and short drift tube	None (cathode cocked)
2A	Same as S/N 2 except single disc, edge-brazed alumina window	190 kW peak, short pulse 38% efficiency (72 kV) 207 kW, 100 ms pulse 31% efficiency (80 kV)
3	Same as 1A, except beam scraper and double disc, BeO window; Full CW cooling	None (beam scraper oscillation)

to the development program. Some of the salient accomplishments which are related to this gyrotron program are given in Table 8-2.

The acquisition of the 3 MW power supply from the MSR transmitter was accomplished with gyrotron development funds, as a means to have a MW gyrotron test capability, as well as for 200 kW CW gyrotrons. It was unfortunate that the gyrotron program was later short of both development and facility funding.

All of the commercially-available gyrotrons and most of the US experimental gyrotrons produced before the start of this program employed oil-cooled cathodes. The Hughes development program demonstrated conclusively that cooling was unnecessary, at least to 100 ms pulse widths.

Hughes EDD was the first (to our knowledge) to introduce a computer analysis of both linear and non-linear, circular waveguide microwave tapers for evaluating mode conversion. This analysis proved accurate for the mode purity obtained with the 919H. Hughes has provided computer-numerically-controlled up tapers for all its gyrotrons, starting with S/N 1.

At the outset of the program, US CW gyrotron collectors required excessively high coolant flow-rates and high pressure drops. This imposed an expensive burden on the gyrotron user. The Hughes gyrotron collector was evaluated with conventional computer trajectory plots and thermal-mechanical analyses as well as X-ray techniques and thermocouple measurements of actual CW-relevant operating tubes. In addition, Hughes introduced infra-red imaging and photo-diode-backed scintillating crystals as a further means for improving collector diagnostics. These techniques provided high confidence that an efficient cooling technique could be realized. In order to offset uncertainty over the integrity of the final design, a mock-up collector was constructed which withstood 345 gpm water flow at a pressure drop of only 60 psi. Thus high confidence was achieved in this extremely efficient cooling technique.

During gyrotron testing in the pulsewidth regime of 10s of milliseconds, it became apparent that a high VSWR was suddenly being presented to the tube. RF pulses would manifest a suddent change from flat top to hash. This RF hash

TABLE 8-2

OTHER GYROTRON-RELATED ACCOMPLISHMENTS
DURING HUGHES-DOE PROGRAM

- Acquired 3 MW Power Supply.
- Proved oil-cooled cathodes are not required, at least up to 100 ms.
- Provided first computer analysis of linear and curved tapers for mode conversion.
- First use of curved up-tapers and down-tapers in gyrotrons.
- Introduction of novel methods of evaluating collector power dissipation (infra-red imaging and photo-diode-backed scintillating crystals).
- Demonstrated the feasibility of high flow, low pressure cooling up to 345 gpm at 60 psi.
- Improved RF load performance at 60 GHz.
- Improved the bandwidth of CW relevant vacuum windows with multi-disc design; 28 GHz barrier window provided to ORNL.

was later found to be caused by boiling in the RF water load, near the cone-to-water interface, due to the high dielectric constant and loss tangent of water at 60 GHz. Experiments with other absorbing media were unsuccessful, therefore, Hughes EDD embarked on its own RF water load design. Basic improvements were implemented by simple baffling techniques which increased the turbulence of the water flow close to the cone. A Hughes RF water load is currently in use at Kyoto's Heliotron E, where it is successfully being employed to evaluate five gyrotron waveguide systems.

The full merit of the wideband, multi-disc window is unknown at this time. The RF properties of this window offer low VSWR over bandwidths as wide as 10%, with reasonably low loss. This bandwidth is necessary for suppression of spurious modes. High temperature, high strength materials are utilized in its construction and thermal-mechanical analysis indicates it is capable of high CW power levels. A barrier window was designed and constructed using this wideband technique at 28 GHz, where CW testing could be undertaken at ORNL. No results are yet available from ORNL, however, the superior qualities of this window have been demonstrated on the 919H, 100 ms pulsed gyrotron.

8.1.3 Hughes 919H Gyrotron

This tube represents the first commercial gyrotron manufactured by Hughes, and its design is based on the experience gained through the DOE gyrotron program. The salient features of this 53 GHz gyrotron are listed in Table 8-3, and are representative of how Hughes would build a CW gyrotron today.

Of particular significance, it should be noted that the efficient collector cooling of the 919H is approximately an order of magnitude improvement over other commercially available 100 ms pulse gyrotrons.

The achievement of greater than 95% mode purity and greater than 10 dB of dynamic range can be directly attributed to the use of the wideband window.

The features of Table 8-3 therefore represents the successful conclusion of the DOE-funded experimental program and the beginning of a new generation of gyrotron devices.

TABLE 8-3

OTHER FUSION-RELATED GYROTRON ACCOMPLISHMENTS
HUGHES 919H

- 200 kW power output, 100 ms pulse, 1% duty
- Low flow collector cooling (20 gpm, 20 psi)
- Wide band gyrotron window
- Symmetric collector pump-out assembly
- Low power, thermally-isolated cathode assembly
- Non-radiating (RF) collector insulators
- Greater than 95% mode purity
- Dynamic range from less than 15 kW to over 200 kW.

8.2 RECOMMENDATIONS

The Hughes-DOE gyrotron program has taken a slightly different path from other gyrotron developers toward attainment of a 200 kW CW goal. Some of these paths are believed to be worthy of further exploration because they may benefit the entire fusion community.

The benefit from the use of efficient collector cooling techniques is two-fold:

- the high cost of gyrotron heat exhangers, pumps, etc. can be significantly reduced, and
- efficient collector cooling can lead to longer collector life, with less cyclic fatigue.

Another departure taken by Hughes EDD is the wideband window. The virtues of this window technique in suppressing undesired modes have been fully demonstrated in the 919H. However, the RF power handling capability of this window is undemonstrated at this time. Yet, at the time of this writing, the worthiness of double-disc windows at 60 GHz for long CW periods or cyclic periods is also uncertain.

It is therefore recommended that both efficient collector cooling techniques and wideband window techniques be further exploited.

9.0 LIST OF SYMBOLS

$\vec{r}$	position vector
(r, θ, z)	circular cylindrical coordinates
ω	rf circular frequency
λ, λ_g	free space wavelength, guide wavelength
k	rf wave number
m, n, ℓ	azimuthal, radial, axial mode numbers
a	cavity radius
L	cavity length
p_{mn} or p	the n^{th} zero of $J_m'(x) = 0$
Q	resonance quality factor
E	electric field intensity
J_m	Bessel function of the first kind of order m
γ	Lorentzian relativistic factor
v	electron velocity
c	vacuum speed of light
β	normalized electron velocity
B	magnetic flux density
Ω_c	cyclotron frequency (radians/s)
s	cyclotron harmonic number
r_L	Larmor radius
b	beam guiding center radius
η	e/m (electron charge to mass ratio)
ϵ	dielectric constant

10.0 REFERENCES

1. Technical Proposal, 110 GHz, 200 kW Gyrotron, prepared by Hughes Aircraft Company for Oak Ridge National Laboratory, March 1979.

2. "Review of the DOE Gyrotron Development Program by the Gyrotron Technical Review Committee, June 7 and 8, 1982," enclosure of letter dated November 3, 1982, from C. M. Loring.

3. Private Communication, dated September 7, 1984, from Dr. Manfred Thumm, University of Stuttgart.

Internal Distribution

1. P. F. Becher
2. L. A. Berry
3. T. S. Bigelow
4. J. M. Galyon
5. H. H. Haselton
6-8. G. R. Haste
9. H. D. Kimrey, Jr.
10. R. P. Jernigan
11. H. C. McCurdy
12. D. H. Metzler
13. O. B. Morgan
14. J. Sheffield
15. T. L. White
16-17. Laboratory Records Department
18. Laboratory Records, ORNL-RC
19. Y-12 Document Reference Section
20-21. Central Research Library
22. Fusion Energy Division Library
23. Fusion Energy Division Publications Office
24. ORNL Patent Office, ATTN: J. M. Spicer

External Distribution

25. M. N. Asfar, Francis Bitter National Magnet Laboratory, Massachusetts Institute of Technology, Cambridge, MA 02139

26. D. S. Beard, Office of Fusion Energy, Office of Energy Research, ER-531 GTN, U. S. Department of Energy, Washington, DC 20545

27. N. Bowen, Princeton University, Plasma Physics Laboratory, P. O. Box 451, Princeton, NJ 08540

28. R. A. Dandl, AMPC, Inc., 2210 Encinitas Blvd. Suite P, Encinitas, CA 92024

29. J. F. Decker, Office Fusion Energy, Office of Energy Research, ER-1, GTN, U. S. Department of Energy, Washington, DC 20545

30. N. J. Dionne, Raytheon Co., Microwave and Power Tube Division, Waltham, MA 02254

31. W. Friz, AFAL/DHM, Wright Patterson AFB, OH 45433

32. T. V. George, Office of Fusion Energy, Office of Energy Research, ER-531, GTN, U. S. Department of Energy, Washington, DC 20545

33. T. Godlove, Office of Energy Research, ER-20, GTN, U. S. Department of Energy, Washington, DC 20545

34. M. J. Gouge, U. S. Department of Energy, Oak Ridge Operations, P. O. Box E, Oak Ridge, TN 37831

35. V. J. Granatstein, Naval Research Laboratory, Code 6740, Washington, DC 20545

36. G. M. Haas, Office of Fusion Energy, Office of Energy Research, ER-533, GTN, U. S. Department of Energy, Washington, DC 20545

37. J. L. Hirshfield, Yale University, Department of Engineering and Applied Science, P. O. Box 2159, Yale Station, New Haven, CT 06520

38. W. W. Ho, Rockwell International Science Center, 1049 Camino dos Rios, Thousand Oaks, CA 91360

39. H. Hsuan, Plasma Physics Laboratory, Princeton University, P. O. Box 451, Princeton, NJ 08544

40. H. R. Jory, Varian Associates, Inc., 611 Hansen Way, Palo Alto, CA 94550

41. K. Krause, MFE Electronics Engineering Department, Lawrence Livermore National Laboratory, P. O. Box 5511 (L-634), Livermore, CA 94550

42. J. V. Lebacqz, Stanford Linear Accelerator Center, Stanford University, P. O. Box 4349, Stanford, CA 94305

43. C. M. Loring, Varian Associates, Inc., EIMAC Division, 301 Industrial Way, Can Carlos, CA 94070

44. C. P. Moeller, GA Technologies, Inc., Fusion and Advanced Technology, P. O. Box 85608, San Diego, CA 92138

45. R. Prater, GA Technologies, Inc., Fusion and Advanced Technology, P. O. Box 85608, San Diego, CA 92138

46. R. Profant, Office of Nuclear Materials Production, DP 13.2, GTN, U. S. Department of Energy, Washington, DC 20545

47. M. E. Read, Naval Research Laboratory, Code 6740, Washington, DC 20375

48. D. B. Remsen, GA Technologies, Inc., Fusion and Advanced Technnmology, P. O. Box 85608, San Diego, CA 92138

49. T. E. Romesser, TRW, 1 Space Park, Bldg. R-1, Room 2044, Redondo Beach, CA 90278

50. G. Simonis, Harry Diamond Laboratory, 2800 Powder Mill Road, Adelphi, MD 20783

51. M. S. Sparks, Science Research Center, 9507 High Ridge Place, Beverly Hills, CA 90210

52. B. L. Stallard, Lawrence Livermore Laboratory, P. O. Box 5511 (L-637), Livermore, CA 94550

53. H. S. Staten, Office of Fusion Energy, Office of Energy Research, ER-531, GTN, U. S. Department of Energy, Washington, DC 20545

54. M. A. Stroscio, AFOSR, Bolling Air Force Base, Washington, DC 20332

55. R. S. Symons, Litton Industries Inc., Electron Tube Division, 960 Industrial Road, San Carlos, CA 94070

56. P. J. Tallerico, AT-5, Accelerator Technology Division, Los Alamos Scientific Laboratory, MS 821, P. O. Box 1663, Los Alamos, NM 87545

57. R. J. Temkin, Plasma Fusion Center, Massachusetts Institute of Technology, 167 Albany Street AW16-254, Cambridge, MA 02139

58. Director, U. S. Army Ballistic Missile Defense Advance Technology Center ATTEN: D. Schenk, ATC-R, P. O. Box 1500, Huntsville, AL 35807

59. Office of Assistant Manager for Energy Research and Development, Oak Ridge Operations Office, Department of Energy, Oak Ridge, TN 37831

60-61. Technical Information Center, Oak Ridge, TN 37831